Investigation of the precipitation hardening behaviour and the corrosion properties of novel aluminium-manganese alloys containing scandium and zirconium

Doctoral Thesis
(Dissertation)

to be awarded the degree

Doctor of Engineering (Dr.-Ing.)

submitted by

Dipl.-Ing. Dhritti Tanprayoon

from Bangkok, Thailand

approved by the Faculty of Natural and Materials Science,

Clausthal University of Technology

date of oral examination

24 September 2015

Dean

Prof. Dr. rer. nat. Winfried Daum

Chairperson of the Board of Examiners

Prof. Dr. rer. nat. Albrecht Wolter

Chief Reviewer

Prof. Dr.-Ing. Babette Tonn

Reviewer

Hon.-Prof. Dr.-Ing. Volkmar Neubert

Acknowledgements

I would like to express my deepest gratitude to Prof. Neubert for his support and guidance throughout my research. I am sure that the knowledge I acquired from him will be applicable for the rest of my life.

I would like to thank Mrs. Tonn for giving her valuable time to review my work. Her comments and suggestions have been a great help towards the conclusion of my thesis.

I am grateful to the Institute for Materials Testing and Material Engineering Dr. Neubert GmbH for their academic and financial supports over the past six years. I would like to take this opportunity to thank Dipl.-Ing. Reuter for sharing his practical experiences as a mechanical engineer. I also appreciated such valuable advice from Mr. Jeschke about the metallographic preparation.

I am honoured to have been given an opportunity to work with the Faculty of Mathematics and Physics at the Charles University in Prague. With this, I thanked Prof. Stulíková, Prof. Smola and Dr. Vlach for their suggestions in the field of resistrometry measurement.

I would like to express my gratitude to Prof. Dölling and Mr. Pereira, who advised me about the corrosion test, especially the evaluation of the potentiostatic electrochemical measurement.

I would also like to thank Mrs. Lenk, Mr. Herrmann and Mr. Fischer, who operate the electron microscopes, for helping me to discover my own mistakes.

As a foreign student, whose native language is not English, this thesis would not be completed without the revisions from Mrs. Lenger.

This thesis is dedicated to my family, who have supported me from the beginning until the end of my graduation. I am most grateful to my parents for their encouragement. I also appreciate the constructive criticisms from my brothers, who kept me grounded as I wrote my thesis.

Abstract

An addition of manganese offer many improvements for aluminium alloys such as the recrystallisation temperature, extrudability and corrosion resistance. However, the aluminium alloys containing manganese have relatively low strength due to the lack of the precipitation hardening effect. Because of this, until today, the applications of the aluminium-manganese alloys are limited.

The properties of novel aluminium-manganese alloys with the addition of scandium and zirconium were investigated. The samples from three different production routes - cast, cast-hot extruded and atomised-hot extruded - were subjected to the annealing in the temperature range from 200 to 600°C up to 48 hours. After this time period, one sample was recrystallised.

The light microscope, the scanning electron microscope (SEM) and the transmission electron microscope (TEM) were used to characterise the microstructures. The microstructural developments of the samples after quenching were deduced from the changes in specific resistivity at -196°C. The hardness increase due to the $Al_3(Sc,Zr)$ precipitates was studied by the Vickers hardness measurement (HV5).

As the aluminium-manganese alloys are generally wrought alloys, the corrosion characteristics of the extruded samples quenched from the temperatures above were determined by the potentiostatic polarisation in 0,1 M NaCl solution.

The peak hardness was observed after the heat treatment for the cast samples unlike the extruded samples, whose maximum hardnesses were obtained right after the extrusion. The specific resistivity changes showed the influence of the extrusion process on the precipitation of the Al_6Mn phase. However, the hardness increase from this phase was negligible.

The corrosion characteristics of the cast-hot extruded sample remained unchanged during the heat treatment. On the contrary, the corrosion behaviour of the atomised-hot extruded sample was greatly affected by a contaminant, which prevented the passivation of the surface after the annealing at 600°C.

The results suggested the benefit of scandium and zirconium as the alloying elements in the aluminium-manganese alloys without modifying their corrosion behaviour. In comparison to the previous result, the resistance to the pitting corrosion was improved by the manganese addition, especially when manganese was in the solid solution.

To my family

Publications from this Dissertation

1. M. Vlach, I. Stulíková, B. Smola, H. Císařová, J. Piešová, S. Daniš, R. Gemma, D. Tanprayoon and V. Neubert

   Microstructure, Thermal and Mechanical Properties of Non-Isothermally Annealed Al-Sc-Zr and Al-Mn-Sc-Zr Alloys Prepared by Powder Metallurgy

   Acta Physica Polonica A **122** (2012): 439-443

2. Martin Vlach, Ivana Stulíková, Bohumil Smola, Hana Císařová, Tomas Kekule, Jaroslav Malek, Dhritti Tanprayoon, Volkmar Neubert

   Response of Hot-Extruded Al-Mn-Sc-Zr Alloy to Annealing with Constant Heating Rate

   Defect and Diffusion Forum **334-335** (2013): 161-166

3. M. Vlach, I. Stulikova, B. Smola, T. Kekule, H. Kudrnova, S. Danis, R. Gemma, V. Ocenasek, J. Malek, D. Tanprayoon, V. Neubert

   Precipitation in cold-rolled Al-Sc-Zr and Al-Mn-Sc-Zr alloys prepared by powder metallurgy

   Materials Characterization **86** (2013): 59-68

Contents

1. Introduction

The element aluminium (Al) was first named *aluminum* by Sir Humphry Davy in 1805, even though he was not able to extract it at that time. While the name aluminum was adopted to aluminium to be consistent with other element names, the original spelling is still accepted, and widely used in North America. The early aluminium production by metallothermic reduction process was not economical, making aluminium so valuable that it was once exhibited alongside the Crown jewels of England at the Paris Exposition of 1855 [1]. The abundance of aluminium and other metals in the Earth's crust can be taken from **Table 1**. Despite being the most abundant metallic element in the Earth's crust, the importance of aluminium as a metallic material for engineering applications was first recognised in the late 19th century after the implementation of the electrolytic process [2].

Element	**Chemical symbol**	**Abundance on Earth's crust in mg/kg**
Aluminium	Al	82300
Iron	Fe	56300
Magnesium	Mg	23300
Titanium	Ti	5650
Manganese	Mn	950
Zirconium	Zr	165
Zinc	Zn	70
Copper	Cu	60
Scandium	Sc	22
Lead	Pb	14
Silver	Ag	0,075
Platinum	Pt	0,005
Gold	Au	0,004

Table 1 Abundance of some metallic elements in the Earth's crust [1]

Today, aluminium is considered as an attractive material in many aspects because of its low density and high corrosion resistance in general due to the oxide protective layer. Together with its availability, developments of aluminium alloys have proved to stay in long-term interest of many industries such as automobile, aircraft and spacecraft.

Like other metals, properties of aluminium alloys are defined by its microstructure. Alloying is one way to adjust this microstructure to achieve a preferable property. For example, the refined aluminium 99,99% has the *ultimate tensile strength* (R_m) of about 50 MPa [3], and the application of aluminium would have been very limited. If the traces of silicon and iron are present, the ultimate tensile strength will increase to 80 MPa.

Aluminium alloys are classified in cast and wrought alloys. Because the addition of manganese is especially dedicated to the wrought alloys, the investigation of phases in a cast sample will only serve as the intermediate data in this work. Therefore, only wrought alloy will be investigated further. An overview of commercial aluminium wrought alloys is listed in **Table 2**. Before we progress, it should be pointed out that the 4000 series alloys are assigned as materials for metal-joining applications rather than structure materials. The main consideration for development of this alloy type would be the wettability instead of strength. Thus, the information on mechanical properties is still limited.

	Non-heat-treatable				Heat-treatable		
Series	1000	3000	4000	5000	2000	6000	7000
Main alloying system	None	Al-Mn	Al-Si	Al-Mg	Al-Cu	Al-Mg-Si	Al-Zn-Mg
Concentration range in wt%	None	Mn 0,5-1,5	Si 0,8-1,7	Mg 0,5-5	Cu 2-6	Mg 0,5-1,5 Si 0,5-1,5	Zn 5-7 Mg 1-2
Another additive	Cu	Mg, Cu	N/A	Mn, Cr	Si, Mg	Cu, Cr	Cu
R_m in MPa	50-150	100-260	150-400	100-340	300-450	150-310	320-600
Corrosion resistance	Good	Good	N/A	Good	Poor	Good	Poor
Extrudability	Good	Good	N/A	Poor	Poor	Good	Poor
Application	wire, tube, foil, sheet, heat exchanger, kitchen utensils	tube, foil, sheet, heat exchanger, kitchen utensils, roofing, vehicle parts	brazing (hard soldering) and welding electrode	tube, foil, sheet, kitchen utensils, pressure vessel, shipbuilding	aircraft, spacecraft, screw machine parts, fitting	heat exchanger, vehicle parts, automobile body sheet	aircraft, spacecraft, medium-strength welded structure

Table 2 Aluminium alloys classification and their properties [4,5]

Unlike ferrous alloys, whose strengthening mechanism involves the phase transformation of iron itself, aluminium alloys, on the other hand, gain strength from microscopic second phase particles within the main materials (matrix). The particles can be brought into the materials either by direct addition in the melting process or by thermodynamic formation of particles in the matrix during and after the solidification - the *precipitation*. The precipitates are usually intermetallic phases formed between two metallic elements or more.

However, not all precipitates are able to increase strength. Some precipitates are brittle, while others are needle-shaped, promoting the crack initiation. Eventually, aluminium wrought alloys are then divided again into heat-treatable and non-heat-treatable alloys. The heat-treatable alloys are able to be strengthened by heating, resulting in strength and hardness increase, whereas the non-heat-treatable alloys lack such possibility. The latter alloy type has to rely only on *plastic deformation* subsequent to the solidification process to increase strength, hence the name *wrought alloy*.

Interaction between alloying elements themselves is a complex issue in the development of aluminium alloys. For example, the 2000 series alloys are strengthened by Al_2Cu precipitates. With the presence of magnesium, the intermetallic phase Al_2CuMg is formed during the heat treatment instead. The formation between a small amount of zinc and magnesium into $MgZn_2$ is more favourable than vastly available aluminium atoms in the matrix, but $Mg(ZnCuAl_2)$ will form if copper is added into the 7000 series alloys. The addition of magnesium gives strength to the 5000 series alloys at the cost of inferior extrudability, see **Table 2**. While alloying with silicon (Si) will transform the non-heat-treatable 5000 series into heat-treatable 6000 series alloys, which gain additional strength from Mg_2Si. Nevertheless, the magnesium content of the alloys has to be reduced, in order to remain corrosion resistant.

Even though the intermetallic phase Al_6Mn of manganese doesn't increase hardness in aluminium alloys, the manganese in solid solution improves strength, enhances corrosion resistance and raises the *recrystallisation temperature*. Yet, good extrudability is maintained in the 3000 series alloys. The benefits of manganese in aluminium alloys are so versatile that according to the chemical composition of aluminium wrought alloys, the presence of manganese, if not intentionally added, is allowed in every alloy series [6]. When it comes to material choosing, these well-rounded properties are disadvantageous for the 3000 series alloys. If we take the good corrosion resistance into consideration, the strength increase of the 3000 series alloys is still lower than the 5000 series alloys in general, while the 6000 series alloys also offer good extrudability. In order to improve the properties of aluminium-manganese alloys, a novel alloy with some other alloying elements will be suggested.

An increase in the recrystallisation temperature is profitable for engineering applications. It means, the wrought alloys are able to withstand higher temperature without the microscopic structure (microstructure) reverting back to the state before the plastic deformation, losing strength in progress. High temperature applications will affect the heat-treatable aluminium alloys more than non-heat-treatable aluminium alloys, because the heat treatment temperatures of heat-treatable aluminium alloys lies between 100-200°C [5]. The above mentioned precipitates in heat-treatable alloys are not able to sustain their optimal properties at such high temperatures.

Scandium is considered an expensive element, even though it is more abundant than lead. It is because of disperse distribution of the scandium ore, while the lead ore comes in most case with copper and zinc ores. In recent decades, scandium has gained more interest as an alloying element for aluminium. Scandium improves the strength of the aluminium alloys through the Al_3Sc intermetallic phase. The Al_3Sc precipitates formed during heat treatment are very fine and uniformly distributed, which help retarding the recrystallisation. The recrystallisation temperature of aluminium alloys containing scandium will be higher as a result [7-10].

The properties of the Al_3Sc precipitates can be further improved by the zirconium addition. During the heat treatment, the ternary phase $Al_3(Sc,Zr)$ will be formed instead. Previous investigations show that the aluminium alloys containing $Al_3(Sc,Zr)$ precipitates display better temperature stability than the aluminium alloys containing Al_3Sc precipitates, which will enhance the recrystallisation resistance [7,11-14].

Moreover, the nanoscale sizes of Al_3Sc and $Al_3(Sc,Zr)$ precipitates are comparable to the thickness of the oxide layer of aluminium alloys. In such cases, the precipitates will be embedded in the oxide layer, and the corrosion resistance should not be disturbed by the microscopic flaws near the precipitates.

However, outside the laboratory condition, there are other factors, which are able to influence the microstructure, e.g., production routes, alloy compositions, time and temperature of heat treatment, and so on. These factors may change the properties of aluminium alloys. So, it is beneficial to have a wider range of information about properties of material in various scenarios.

In this work, the precipitation hardening effect of scandium (Sc) and zirconium (Zr) in aluminium will be added in a non-heat-treatable aluminium-manganese (Al-Mn) alloy in attempt to introduce the heat treatment possibilities to these types of alloys without affecting the corrosion resistance.

In order to compare the microstructural development during heat treatments, the hardness and electrical resistivity test will be performed on an alloy from three different production routes with different conditions of heat treatments. The phases are determined by using a scanning electron microscope (SEM) as well as a transmission electron microscope (TEM). As Al-Mn alloys are predominantly utilised as wrought alloys, the examination of corrosion resistance by means of potentiostatic polarisation will be focused on extruded materials, which are used as intermediate material in further processes.

2. Groundwork

The experimental results are by no means from an isolated factor, and many phenomena are able to lead the measurement in the same direction. Because of this, it is critical to understand and define, what is being observed and measured. This chapter will cover the experimentation backgrounds and the properties of aluminium alloys regarding the microstructural changes, which are the foundations of our investigations.

2.1 Experimental techniques

In this work, three tests will be carried out on the samples, namely the hardness, resistrometry and the potentiostatic electrochemical measurement. The hardness will be used to perform a non-destructive observation on the strength of the samples. The resistrometry will help identify the possible occurrences within the microstructure. The potentiostatic polarisation will be performed to monitor the corrosion resistance, which might be distinguishable during the heat treatment.

2.1.1 Hardness measurement

In this experiment, hardness was measured by using the Vickers hardness test (DIN EN ISO 6507-1) with pressing force (HV5) applied for 15 seconds. The hardness value is determined by the ratio of the applied force and the surface area of the pyramidal diamond indentation, see **Figure 1**. According to the standard, the Vickers hardness is defined as [15]:

$$HV = 0{,}102 \cdot \frac{2F \sin\left(\frac{\alpha}{2}\right)}{d^2}, \tag{1}$$

where

HV	Vickers hardness
F	Force in N
d	Arithmetic mean between diagonal d_1 and d_2 in mm, see **Figure 1**
α	Angle between opposing pyramidal faces equals to 136°

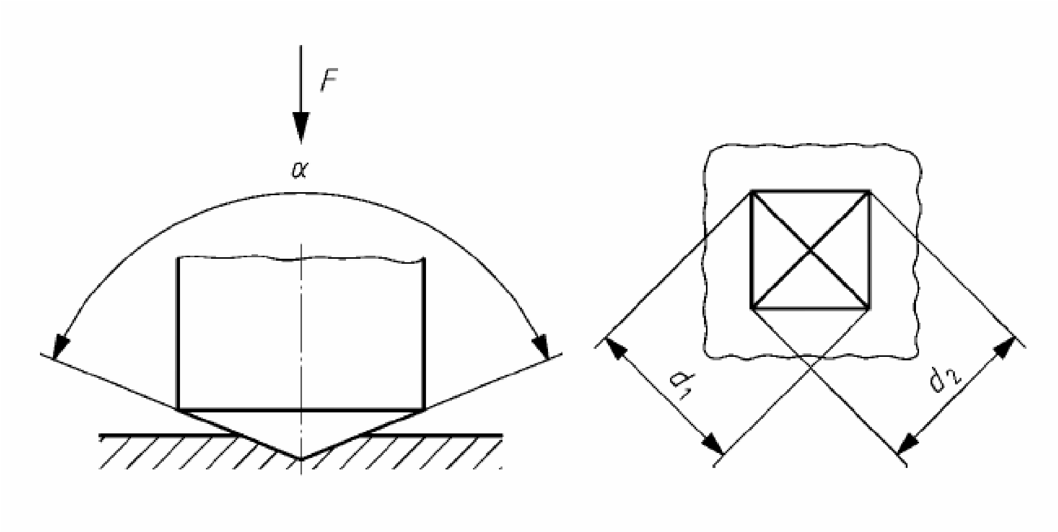

Figure 1 Pyramidal indenter and its indentation (schematic) [15]

In this case, the load for HV5 is 49,03 N according to standard, which simplifies the formula to:

$$HV = \frac{9{,}27}{d^2}. \tag{2}$$

2.1.2 Resistrometry measurement

Metallic materials are usually regarded as excellent electrical conductors due to the mobility of conduction electrons. The capability to permit electron flow is not only material characteristic, but also depends on the sample geometry. The electrical resistance R of a sample with a uniform cross section is proportional to its length l and inversely proportional to cross-sectional area A [16]:

$$R = \rho \frac{l}{A}. \tag{3}$$

The proportional constant ρ is labelled as specific electrical resistivity, and will be calculated from measured electrical resistivity. Hence, equation (3) is rearranged to:

$$\rho = R\frac{A}{l}, \tag{4}$$

where

ρ	Specific electrical resistivity in Ω·m
R	Measured electrical resistance in Ω
A	Sample cross sectional area in m^2
l	Sample length in m

According to Matthiessen's rule, the specific resistivity of metallic material is the sum of temperature-dependent resistivity ρ_t and residual resistivity ρ_D [17], see **Figure 2**:

$$\rho = \rho_t + \rho_D. \tag{5}$$

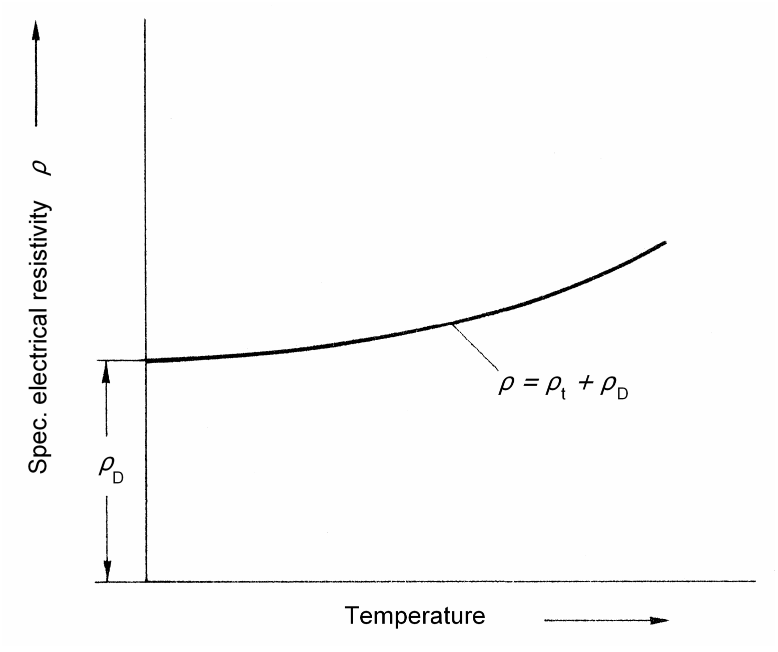

Figure 2 Temperature dependency of specific electrical resistivity in metallic materials [17]

The temperature-independent part is caused by crystallographic defects, e.g., impurities and dislocations, which hinder the flow of electrons. By annealing, microstructural changes will reflect in residual resistivity, which can be easily observed at a low temperature, where it is dominant.

Because of the mentioned properties, measurement of electrical resistivity is commonly used to monitor the precipitation and recrystallisation behaviour of materials during heat treatment. After precipitation, the impurities in the material matrix will become lower, hence less obstruction to the electron flow.

The structural change can result either in an increase or a decrease of electrical resistivity. Dislocations are eliminated by the lattice rearrangement from the recrystallisation of materials, while grain boundaries formed during the process are also known to increase electrical resistivity [18,19].

2.1.3 Potentiostatic electrochemical measurement

While the guideline for measuring potentiostatic polarisation is explained in DIN EN ISO 17475, the decision on test conditions requires further understanding on corrosion reactions. In this chapter, the structure of an electrochemical cell used in the measurement will be explained.

2.1.3.1 Electrode potential

The simplest model to suggest the interaction on an electrode surface is a metal-metal ion electrode model. When a metal is immersed in its salt solution, the surface will show electrical properties:

$$\mathrm{Me} \Leftrightarrow \mathrm{Me}^{z+} + \mathrm{z\,e}^{-}. \tag{6}$$

The reaction will continuously shift towards the thermodynamic equilibrium either by moving forward giving electrons (dissolution of metal), or receiving metallic deposit on the surface in a backward reaction. This natural phenomenon occurs due to the different chemical potential, a driving force of reaction [20]. The metal surface will obtain the electrical properties through the change in either direction. The electrically positive or negative surface can further attract oppositely charged ions in the solution. Because this attraction will form another electrically charged layer, the layers are called together *double layer*. It can be found not only on metal and its ion pair, but also on every metal-electrolyte interface.

In this work, the investigations were performed in 0,1 M NaCl solution, in which the average distance between ions - the ionic cloud radius - has the same order of magnitude of atom radius as shown in **Table 3**. This test condition would allow the simplification of the double layer as a "rigid" conductive layer, the Helmholtz model [21]. By analogy to the parallel-plate capacitor, if the double layer does show electrical properties, the potential of the metal surface $\varphi_{\mathrm{Surface}}$ has to distinguish itself from that of the electrolyte $\varphi_{\mathrm{Electrolyte}}$, see **Figure 3**.

However, this potential difference can not be measured in practice because the measuring instrument itself would act as the second electrode when it is immersed in the electrolyte. The measured potential is the potential difference $\Delta\varphi_{\mathrm{I,II}}$ between the targeted electrode (I) and the interface of the measuring instrument (II), see **Figure 4**.

The potential measurement plays a crucial role in the potentiostatic polarisation. The experimental setup and the relationship between the potential and the measured current will be elaborated in the following chapter.

Concentration in M	**Ionic cloud radius in nm**
10^{-1}	0,96
10^{-2}	3,04
10^{-3}	9,6
10^{-4}	30,4

Table 3 Ionic cloud radius in NaCl solution-type [22]

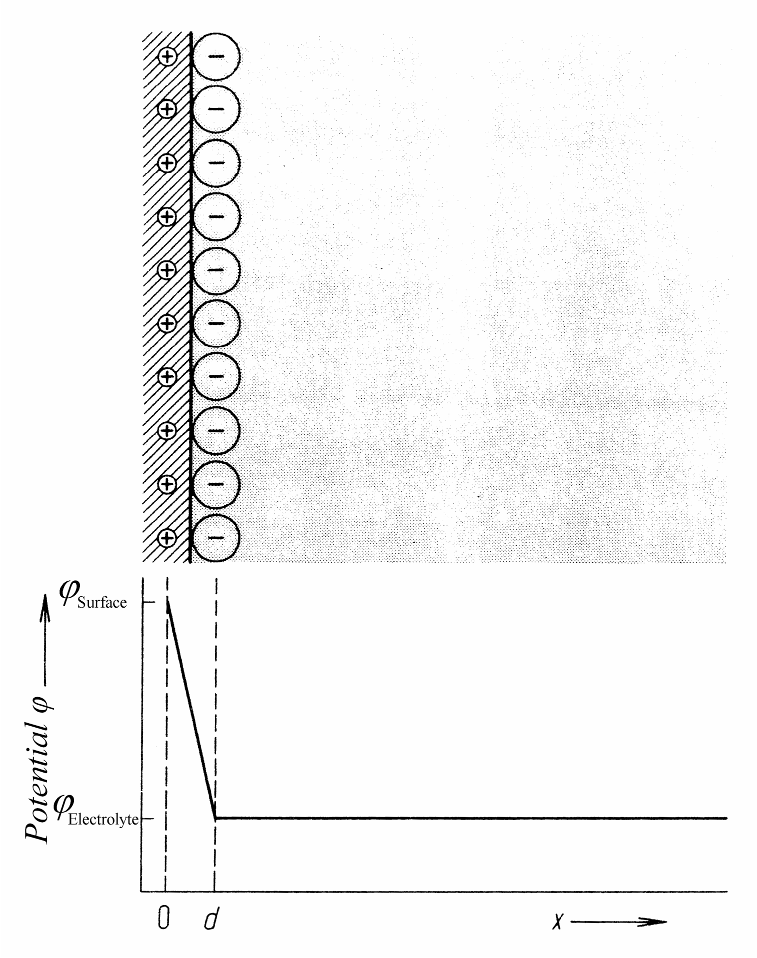

Figure 3 Helmholtz double layer model showing the different potential between the electrode surface and the electrolyte [21]

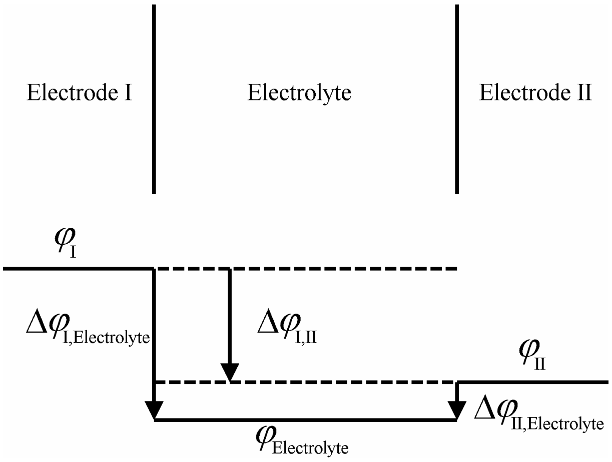

Figure 4 Potential difference between two electrodes $\Delta\varphi_{\text{I,II}}$ immersed in an electrolyte, redrawn from reference [20]

2.1.3.2 Experimental setup and corrosion reaction in the electrochemical cell

With the understanding of surface properties of electrodes, it is clear that the corrosion reaction occurs because of the interaction between the material surface (sample) and the given environment (electrolyte). Therefore, the observation has to be made directly on the surface of the materials. By applying an external power source, the reaction in equation (6) can be shifted to a new position in favour of the given potential.

As the potential is always measured relatively between 2 points, it is necessary to set up a *reference electrode* aside the electric circuit, so that the reference itself does not participate in any reactions. As a result, the experimental setup of the potentiostatic polarisation consists of 3 electrodes, i.e., working, counter and reference electrode. The *counter electrode* is an electrical conductor, which is electrochemically stable throughout the polarisation. It functions as an interface between power supply and electrolyte. The experimental setup is illustrated in **Figure 5**. The sample will be mounted as *working electrode*.

In potentiostatic polarisation, the power supply will polarise the working and counter electrodes until a given potential between working and reference electrodes is attained. The Luggin-Haber capillary is placed near the working electrode in order to measure the potential directly on the surface and minimize error at the same time [23].

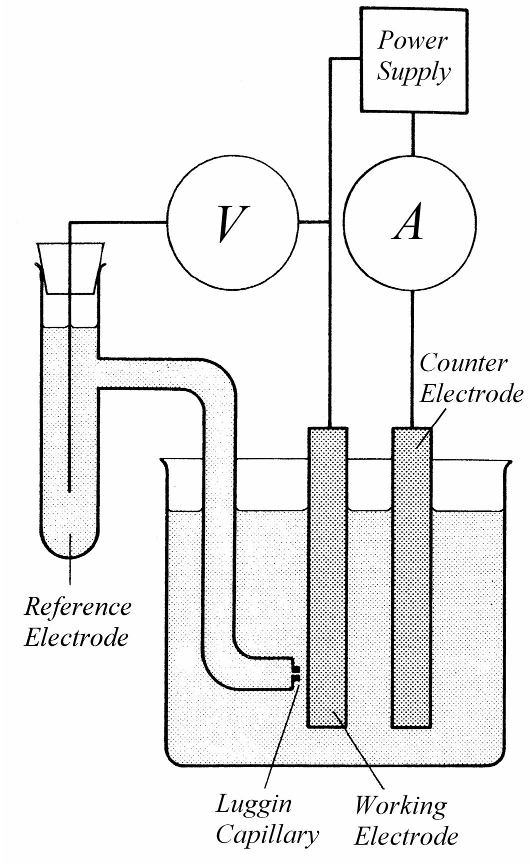

Figure 5 Experimental setup of the three-electrode system for potentiostatic polarisation measurement [23]

With the help of the external power source, the reaction on the working electrode surface can be realised in both directions, resulting in 2 reaction types depending on charge transport. The oxidation number of the investigated material is increased in an anodic half reaction, also known as oxidation reaction. In reverse, the reaction, in which the oxidation number is decreased, is defined as a cathodic half reaction or reduction reaction, e.g.,

anodic half reaction $Al \Leftrightarrow Al^{3+} + 3\,e^{-}$, (7)

cathodic half reaction $2\,H^{+} + 2\,e^{-} \Leftrightarrow H_2$. (8)

The measured electrical current is normalised by the surface area to the current density j, the electrical current per unit surface area of a working electrode. The amount of charge transport in equation (7) and (8) is expressed as anodic current density j_a and cathodic current density j_c respectively. For the sake of clarity, j_a is defined as *positive* and j_c as *negative* in this work.

Under the rest condition, both current densities are equal, and no net current can be measured. It should be noted that the corrosion rate is not zero in this case. The summation of both reactions in this case would understandably eliminate the presence of electrons in the half reactions. This would give a redox reaction (reduction-oxidation reaction):

$$2\,\mathrm{Al} + 6\,\mathrm{H}^{+} \Leftrightarrow 2\,\mathrm{Al}^{3+} + 3\,\mathrm{H}_2 . \tag{9}$$

Equation (9) is the corrosion reaction of aluminium in an aqueous solution. Since this chapter is about the theoretical aspect of experimentation, other mechanisms involving the corrosion of aluminium will be elaborated later in chapter 2.2.4. The exchange current density is a decisive factor to determine the corrosion rate, the purpose of the potentiostatic polarisation.

As we apply the external potential E during the polarisation, the electrode potential will change and differ from the value at the rest condition (E_{Corr}). If the polarisation is strong enough, one of the half reactions will dominate the other. The relationship between the net (measured) current density j and exchange current density j_0 can be simplified to [24]:

$$\log|j| = \log j_0 + B\left(E - E_{\mathrm{Corr}}\right) \tag{10}$$

This semi-logarithmic equation (10) is named *Tafel equation* after Julius Tafel. The *Tafel slope B* is dependent on the dominated half reaction. The cathodic and anodic extrapolations (*Tafel lines*) are shown as dashed lines in **Figure 6** on the left-hand and the right-hand side of the graph respectively.

In the investigation, the working electrode will be scanned from a cathodic reaction to an anodic reaction. However, the potential at the rest condition can not be determined before the polarisation itself. Naturally, the potential of the sample will develop towards the rest condition while the sample is immersed in the electrolyte. Therefore, an open-circuit potential (OCP), observed before the polarisation, is practically used as a guideline for the rest condition.

Inevitably, there are always other reactions within the system, e.g., electrolysis of water. For this reason, the Tafel diagram will not show a linear relationship on the whole polarisation. According to Robert G. Kelly's Electrochemical Techniques in Corrosion Science and Engineering, the extrapolation should start about 50 to 100 mV away from the observed rest condition on both sides, also known as *free corrosion potential* or just *corrosion potential* E_{Corr} [25]. As mentioned above, the word *free* should not be understood as free from corrosion, but rather the corrosion can occur quite naturally or spontaneously at this potential. According to equation (10), the intersection of the anodic and cathodic extrapolations has to be around this corrosion potential resulting in *corrosion current density* j_{Corr}.

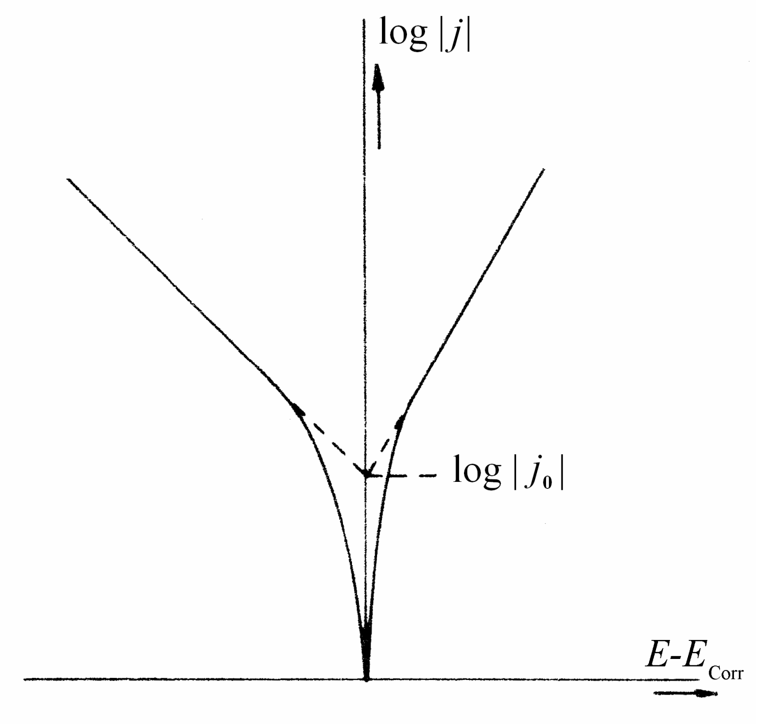

Figure 6 Polarisation diagram (Tafel diagram) of logarithmic current density versus the potential difference E - E_{Corr} [26]

2.1.3.3 Passivity and pitting corrosion

As described in the last chapter, the corrosion current density will give us an idea, how reactive the surface is at the corrosion potential. The surface of aluminium is able to form a protective oxide layer, *passive layer*, preventing it from further corrosion. Additional information about the stability of the passive layer can be studied by the anodic polarisation until the dissolution of the passive layer.

A typical passivation process of the surface is expressed in **Figure** 7. It should be noted that the diagram shows only the anodic current density on a linear scale. When the polarisation surpasses corrosion potential E_{Corr}, the dissolution of the surface will raise until the current density reaches passivation current density j_{p}. Beyond this passivation potential E_{p}, the current density remains relatively constant at a passive anodic current density j_{pass}. The surface is considered to be in a passive state.

At the breakthrough potential E_{b}, the passive layer will start to break down. The term breakthrough or breakdown potential are interchangeably used together with the transpassivation potential [25,27,28], but they are not the same as solution and dissolution potential, which describes the corrosion potential [5,29]. The transpassive state is indicated by an increased current density once more. The dissolution of the passive layer can be uniform, or local depending on the environment.

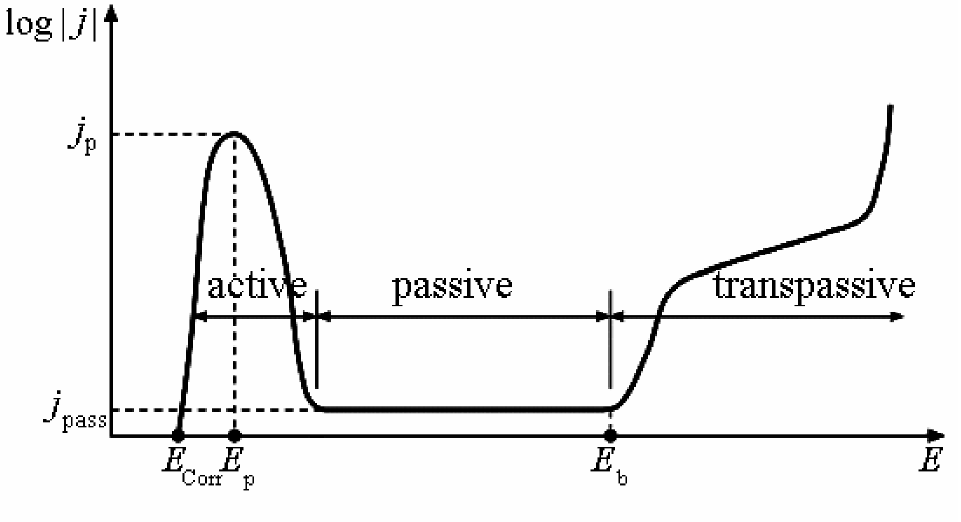

Figure 7 Passivation process of the surface during an anodic polarisation showing active, passive and transpassive state [30]

The chloride-containing electrolyte used in the investigation can promote the local dissolution of the surface, known as pitting corrosion. The detail of pitting mechanism on aluminium will be given in chapter 2.2.4. The pitting corrosion is difficult to verify due to its random occurrence, unlike uniform corrosion. The passive layer can not only be destroyed electrochemically, but also mechanically, making the prediction and detection even more complicated in practice. Fortunately, the repassivation of the passive layer is possible. For engineers, ensuring the repassivation condition is as important as pitting prevention itself.

In order to display the repassivation, the reverse scan is applied after the current density exceeds a pre-defined limit, also known as vertex current density [25], see **Figure 8**. In the international standard, the current density for propagating pitting is defined as 100 $\mu A/cm^2$ [31]. As our samples will be polarised beyond E_b, and the pitting corrosion is expected, this current density value is chosen as a fixed vertex for all polarisations.

At the same time, the potential at the vertex current density can be regarded as pitting potential E_{pit}. The hysteresis loop formed during the reverse scan is a hint at the stability of pits. If the pits are formed and stable, the current density will remain similar to the vertex current density for a while causing a positive hysteresis loop as shown in **Figure 8**. In practice, the potential at intersection of the hysteresis loop is used to set up the *protective potential* E_{prot} for the permanent protection of the structural material (cathodic protection).

Should the repassivation overtake the dissolution of the surface, the passive layer will be thickened over time. The current density on the reverse scan will decrease rapidly, resulting in a much smaller or even negative hysteresis loop [25]. The repassivation potential E_{rp} will enable the protection of the component by applying an external power source, an impressed current, to ensure the repassivation possibility.

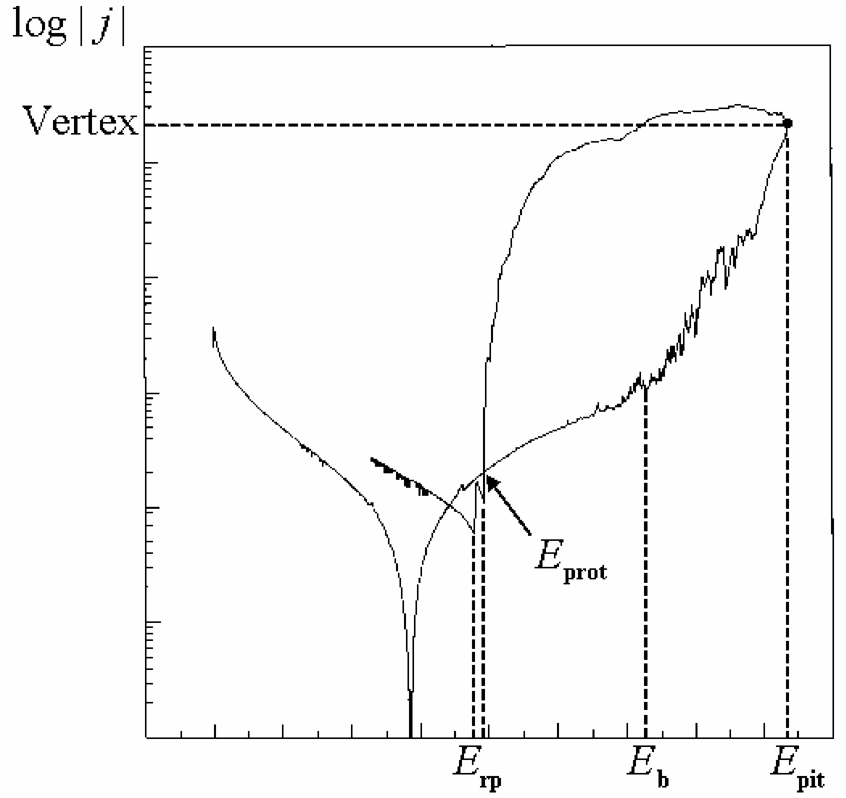

Figure 8 Polarisation curve with positive hysteresis loop on reverse scan indicating the stabilisation of pits during corrosion [25]

2.2 Properties of aluminium alloys

This chapter will introduce the origins of the properties of aluminium alloys. The first two sections will introduce the precipitation, recovery and recrystallisation, which are related to the annealing process. At the end of this chapter, the influence of the precipitates on the recrystallisation and corrosion resistance of aluminium alloys will be explained.

2.2.1 Strengthening mechanism by precipitation hardening

Generally, the shear stress is the critical factor to be taken into consideration for the deformation behaviour of material, because the shear modulus is smaller than the elastic modulus [32]. In other words, atoms will find a preferable plane to move rather than parting from each other. In reality, the yield strength $R_{p0,2}$ of materials are about three orders of magnitude lower than the theoretical shear stresses τ_{th}, see **Table 4**.

Material	τ_{th} **in GPa**	$R_{p0,2}$ **in MPa**
Ag	1,0	0,37
Al	0,9	0,78
Cu	1,4	0,49
Ni	2,6	3,2
α-Fe	2,6	27,5

Table 4 Theoretical shear strength τ_{th} and yield strength $R_{p0,2}$ of some metals [32]

This is mainly because of the one-dimensional crystallographic defect called dislocation $\perp$, see **Figure 9**. The presence of dislocations will allow the partial movement of atoms one after another, thereby lowering the yield strength. This moving array of atoms is referred to as dislocation movement, see **Figure 10**. The concept of the strengthening mechanism of aluminium alloys often involves the restriction of dislocation movement.

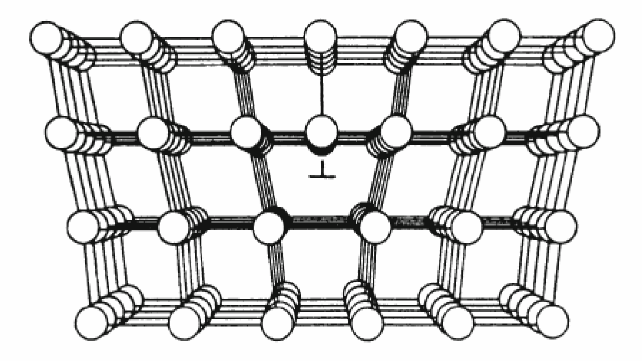

Figure 9 Arrangement of a dislocation [32]

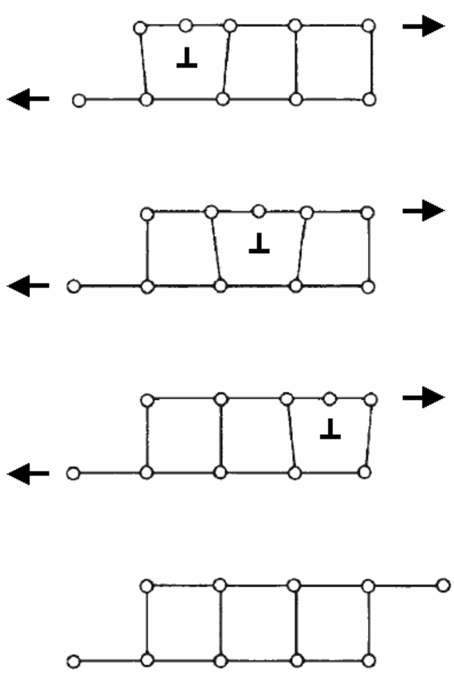

Figure 10 Dislocation movement caused by shear stress [32]

The movement path can be obstructed by particles such as oxide, or intermetallic phases. The dislocations have two mechanisms to move past these particles, depending on the radius r of the particles. For particles smaller than the critical radius, the dislocation will cut through the particles, see **Figure 11a**. The larger the radius becomes, the more stress τ_{cutting} will be required.

$$\tau_{\text{cutting}} \propto \sqrt{r} \tag{11}$$

If the particle radius exceeds r_0, the dislocation will surround the particles. When the dislocation bypasses the particles, the dislocation loops will be formed as shown in **Figure 11b**. The strength of the pinning effect, the Orowan stress τ_{OR}, is inversely proportional to the particle radius. Mathematically considered, the critical radius r_0 is provided by the intersection between τ_{cutting} and τ_{OR}, see **Figure 12**.

$$\tau_{\text{OR}} \propto \frac{1}{r} \tag{12}$$

a)

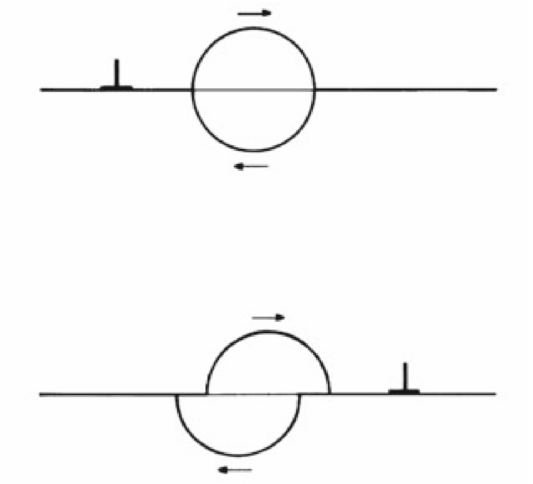

b)

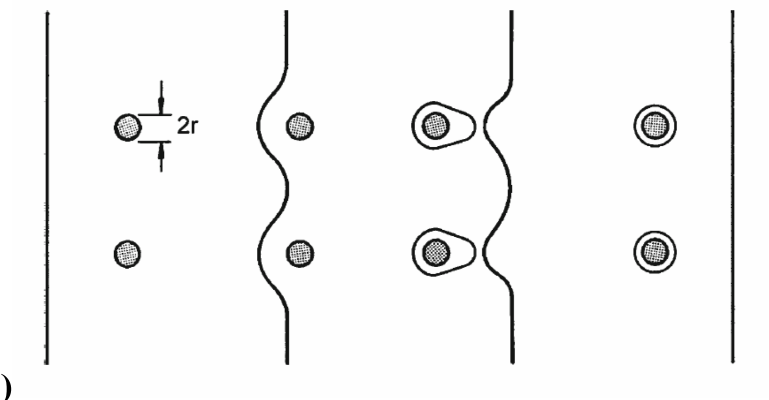

Figure 11 Interaction between dislocation and particles a) cutting through b) bypassing [32]

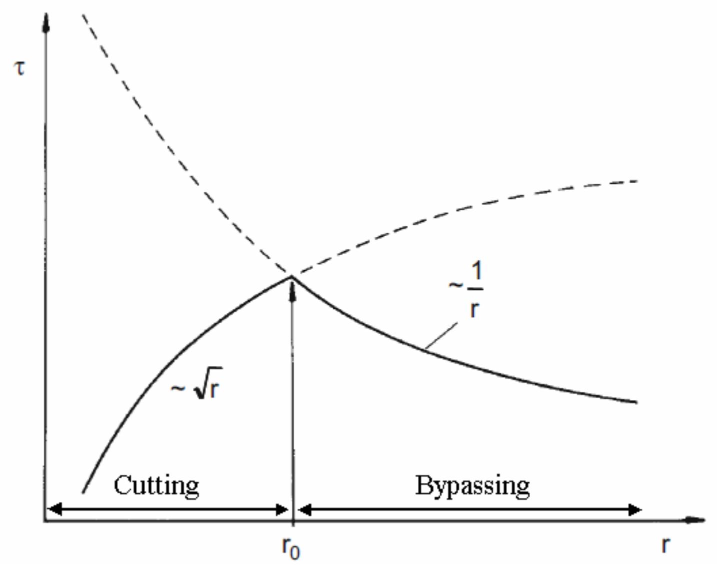

Figure 12 Relationship between particle radius and shear stress [32]

In aluminium alloys, these particles are not always present at the beginning. If the melt is cooled down quickly enough, the formation of other phases will be suppressed. The alloying elements are contained in the material matrix as a solid solution. The material is by no means in the thermodynamic equilibrium, but the formation of stable phases is not possible due to the low diffusion rate at room temperature. With heat treatment, the alloying elements are able to precipitate into other phases. The increased strength is accompanied by an increased hardness, which leads to the name precipitation hardening. Because the investigation centres around the heat treatment, the precipitates will be the main concern in this work.

Although the diffusivity of alloying elements allows the precipitation, it is also the limitation for high temperature applications. As **Figure 12** suggested, the precipitation hardening is dependent on the radius of precipitates. Even if the alloying elements are well adjusted, so that the equilibrium concentration in the matrix is attained right after the heat treatment, the precipitate radius is still influenced by the temperature.

As long as the diffusion permits, the precipitates will reduce their overall surface energy in the process called the *Ostwald ripening*, the coarsening of precipitates at the cost of smaller precipitates nearby. The Ostwald ripening is schematically illustrated in **Figure 13**. As the precipitate **2** coarsens, the concentration of an alloying element near the precipitate will be lower. In order to maintain the bulk concentration c_B, this depletion will be compensated by the shrinking precipitate **1**.

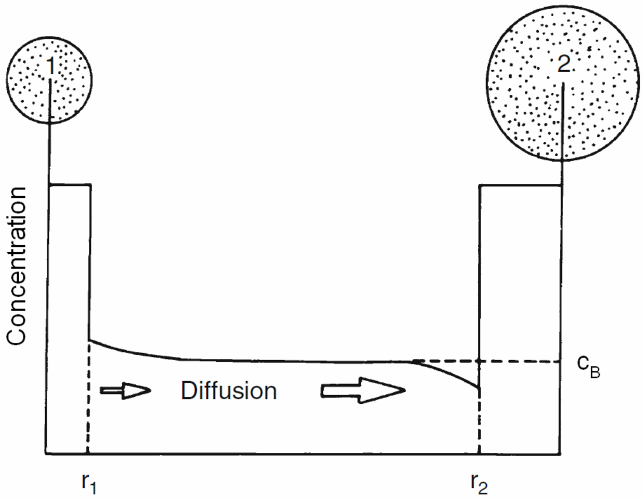

Figure 13 Diffusion scheme during Ostwald ripening due to different precipitate size [32]

Since the diffusion is a thermally activated process, in the end, the strength of heat-treatable aluminium alloys is ruled by the thermal stability of the precipitates.

Still, the material matrix is influenced along with precipitates during heat treatment, which can result in the rearrangement of the material matrix, namely the recovery and recrystallisation. The effect of precipitates on the recrystallisation will be introduced in chapter 2.2.3.

2.2.2 Recovery and recrystallisation

During plastic deformation, about 1% of deformation energy will be stored in form of crystallographic defects, mostly dislocations [33]. However, the materials are not able to use such stored energy to rearrange themselves into a more thermodynamically stable state without any heat treatments. This indicates that the rearrangement is also a thermally activated process.

The power difference, Vickers hardness and specific resistivity change of 75% deformed pure aluminium during isochronal annealing are shown in **Figure 14**. The plateau of the heat difference curve between 100-250°C indicates the recovery stage. During recovery, the crystallographic defects are annihilated, and rearranged. The interstitial atoms diffuse to vacancies, and the opposing dislocations will compensate themselves, see **Figure 15a** and **b**. The remaining dislocations will form an array shown in **Figure 15c**. This phenomenon is called polygonisation, the formation of subgrains (low angle grain boundary). The specific resistivity is expected to be lower resulting from a reduced number of crystallographic defects, while mechanical properties, in this case Vickers hardness, are barely affected until the transition to the recrystallisation stage [2].

The peak at 300°C is the recrystallisation peak followed by significant changes in Vickers hardness and specific resistivity. The recrystallisation is characterised by the rearrangement of a deformed structure with a high dislocation density by forming new grains. The dislocation density will be reverted back to the magnitude of non-deformed material. The dislocations will serve as nuclei for new grains, and these grains will grow in order to lower the Gibbs free energy per unit volume. Therefore, it is not surprising that the energy per unit volume will often be described as the *driving pressure* ($J \cdot m^{-3} = N \cdot m^{-2}$), or the physically incorrect but more conventional expression - the driving force [9,34-43].

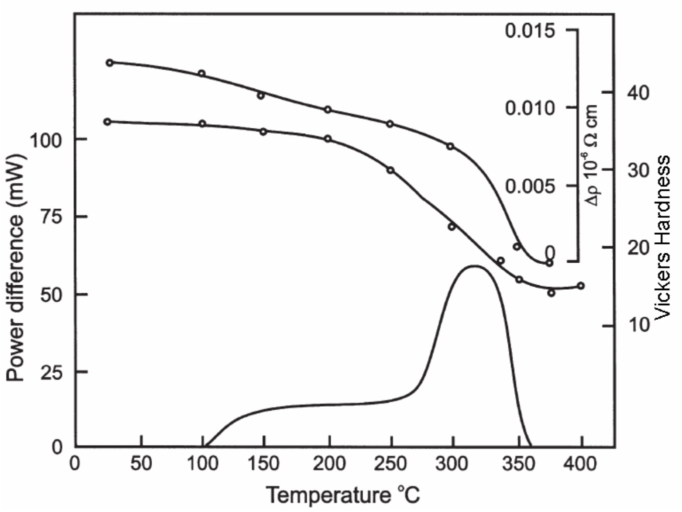

Figure 14 Recovery and recrystallisation of 99,998% pure aluminium compressed 75% measured by calorimetry with heating rate 6°C/min [33]

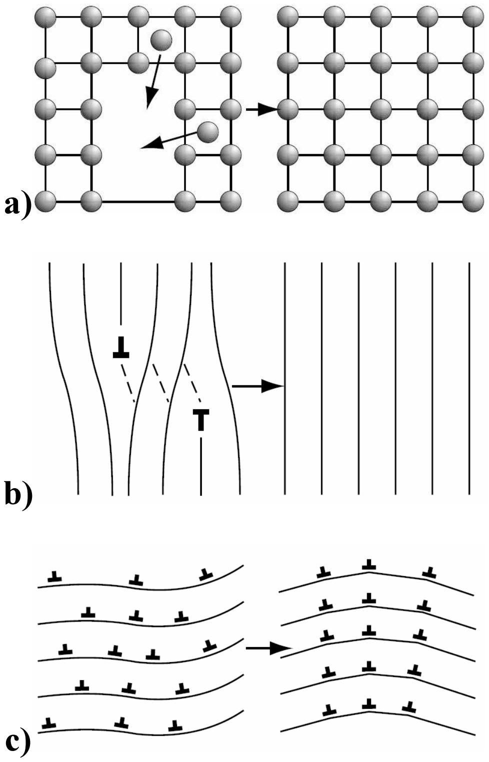

Figure 15
Crystallographic defect annihilations and rearrangement during recovery [2]

a) Interstitial atoms diffusion

b) Dislocation annihilation

c) Polygonisation

2.2.3 Zener drag and its benefit in recrystallisation resistance

Precipitates play a very complex role in the recrystallisation of materials. Similar to solidification, particles are able to promote heterogeneous nucleation of the recrystallisation, if their sizes are larger than a critical size about 1 μm [33]. This process is known as particle stimulated nucleation (PSN), see **Figure 16**. Contrarily, the growth of recrystallised grains is pinned down at precipitates, and is explained as follows:

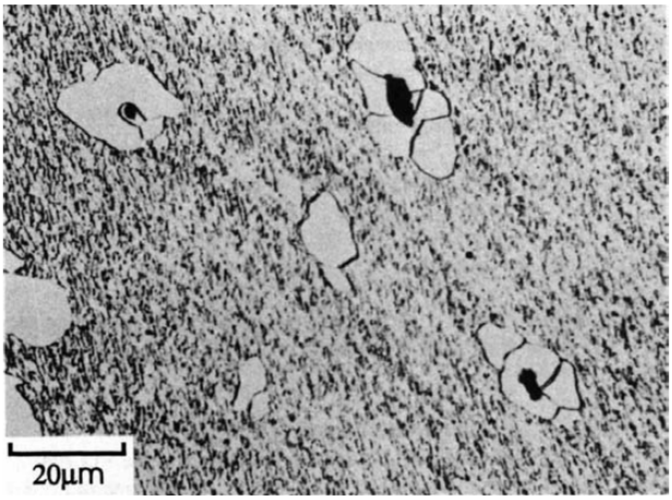

Figure 16 Nucleation of the recrystallisation at the oxide inclusions in iron [33]

Because the surface area of a migrating grain boundary is reduced during contact with the precipitates, the same area has to be formed again as it departs the precipitates. The cause of this hindrance is boundary tension, see **Figure 17**. The retarding force F_r is given by equation (13) [33].

$$F_\mathrm{r} = -2\pi r_\mathrm{p} \sin\theta \, \gamma \cos\theta \tag{13}$$

where

F_r	Retarding force per unit length of interfacial boundary in N·m^{-1}
r_p	Radius of precipitate in m
γ	Specific grain boundary energy in J·m^{-2}

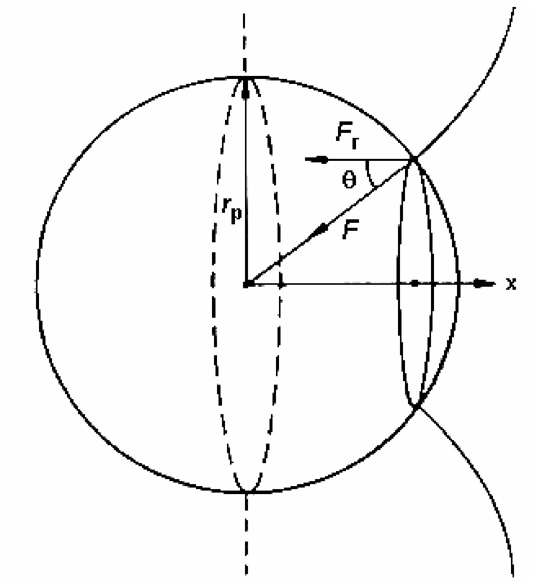

Figure 17 Retarding force F_r resulting from boundary tension of departing grain boundary [32]

The migrating grain boundary has to overcome the maximum value of equation (13) when $\theta = 45°$ in order to depart from a single precipitate. The negative sign indicates the retarding effect on recrystallisation, if we consider the driving pressure in the last chapter as being positive. The retarding pressure, commonly known as the *Zener drag*, is formulated by multiplication of the maximum retarding force with the number of momentary intersecting precipitates per unit area.

$$P_z = -2\pi r_p \frac{1}{\sqrt{2}} \gamma \frac{1}{\sqrt{2}} \cdot \frac{3f}{2\pi r_p^{\,2}} \tag{14}$$

$$P_z = -\frac{3}{2} \gamma \frac{f}{r_p} \tag{15}$$

where

P_z Zener drag in $J \cdot m^{-3}$

f Volume fraction of precipitates; dimensionless

It should be noted that the number of momentary intersecting precipitates is based on rigid and planar grain boundary, in which the retarding force would have compensated itself, see **Figure 18**. In reality, the grain boundary is flexible, and the pinning effect will take place on each precipitate, see **Figure 19**.

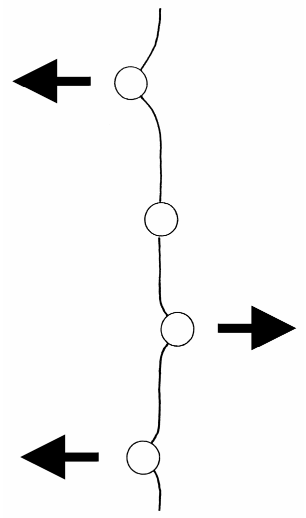

Figure 18 Compensation of retarding force in simplified grain boundary, redrawn from reference 44

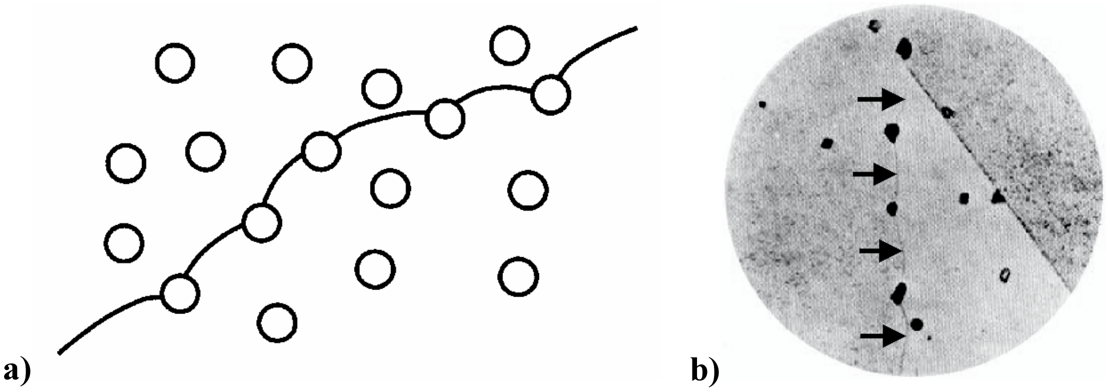

Figure 19 Pinning effect of flexible grain boundary: **a)** schematic [33] and **b)** in α-brass [32]

From equation (15), large Zener drag can be achieved by raising the value of ratio $\frac{f}{r_\mathrm{p}}$. In this work, scandium and zirconium will be used to produce the very fine and homogeneously distributed $Al_3(Sc_x,Zr_{1-x})$ precipitates.

2.2.4 Corrosion of aluminium alloys

Aluminium is, in fact, a very reactive metal with the standard electrode potential -1660 mV versus the standard hydrogen electrode (SHE) at 25°C. For the sake of consistency, the electrode potential is recalculated into -1904 mV versus the *saturated calomel electrode (SCE)* used in this work, which has a **+244 mV** potential shift from SHE [5].

The value of the standard electrode potential does not imply any corrosion resistance of pure aluminium in practice because during the above mentioned measurement, the surface of aluminium is always in the active state. The measurement of the standard electrode potential takes place in the electrolyte with 1 M hydronium ions, where the aluminium surface is not passivated.

In order to understand these circumstances, we will have to make a detour and first, explain how the aluminium surface is passivated. As stated in chapter 2.1.3.3, the passivation of the aluminium surface is due to the protective oxide layer, the passive layer.

$$4\,\mathrm{Al} + 3\,\mathrm{O}_2 \Leftrightarrow 2\,\mathrm{Al}_2\mathrm{O}_3 \tag{16}$$

The very first layer formed on the surface is called the barrier layer. It is formed almost within the order of milliseconds after contact with oxygen, or oxidising media [5]. The formation of the passive layer is also possible in an electrolyte. Huppatz has demonstrated the almost instantaneous re-formation of the passive layer during polarisation of alloy 5049, see **Figure 20**.

The observation made by Vernon shows that further oxidation has resemblance to the parabolic law [45]. Thus, the structure of the barrier layer can be assumed dense and compact, and the further oxidation is provided by the diffusion. The second layer will grow on the top of the barrier layer, which explains the parabolic law. The maximum thickness of the second layer is 4 nm [46].

The parabolic growth of the second layer is within a matter of weeks or even months, much slower than the barrier layer. The formation depends on the alloy compositions, and the environment such as temperature and humidity. In literature, the total thickness of a naturally formed passive layer is about 5-10 nm [5,45,47].

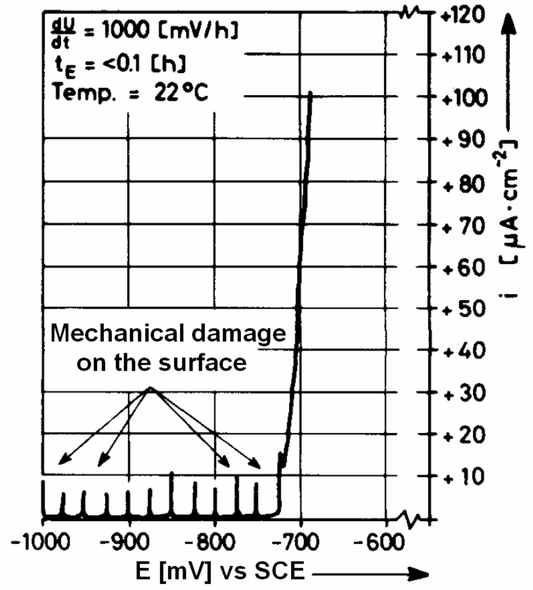

Figure 20 Re-formation of the passive layer of alloy 5049 during polarisation in artificial sea-water after mechanical damages [48]

The corrosion resistance of aluminium material is generally understood as the stability of the passive layer, which is commonly determined by the corrosion potential, see chapter 2.1.3.3. Normally, the oxidation of an aluminium surface will give aluminium oxide, which is an amphoteric compound, and will react in acidic as well as alkaline media. Therefore, in general, aluminium alloys may be considered stable in the solution with pH values between 4 to 9 as shown in **Figure 21**, which is the reason why the standard electrode potential of the aluminium is from the active state.

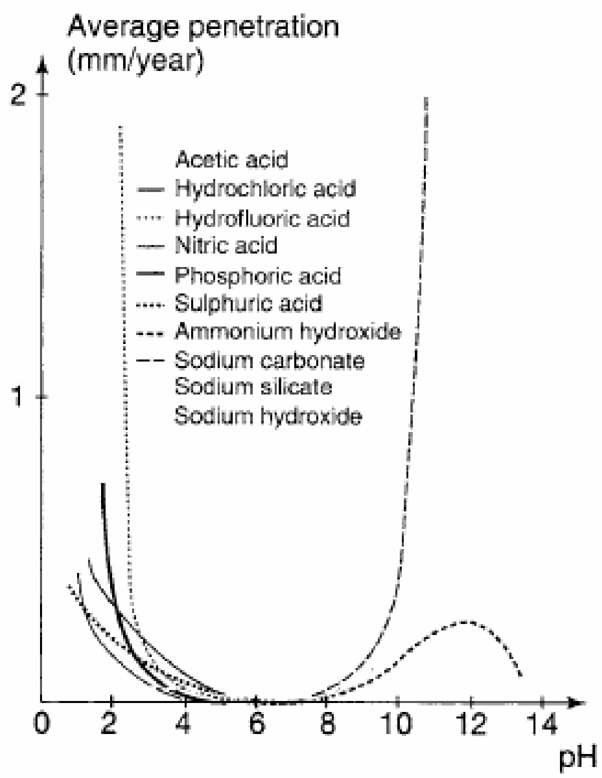

Figure 21 Corrosion of alloy 1100 in different acidic and alkaline media [5]

In the presence of chloride ions, the intermediate aluminium chloride $AlCl_3$ [47] or hydrochlorinated intermediate complex $AlCl_4^-$ [5] can be formed. These products are able to hydrolyse water molecules into hydrochloric acid, causing local acidity, in which the pH can be lower than 3 [5]. This will cause localised corrosion known as *pitting corrosion.*

$$AlCl_3 + 6\,H_2O \Leftrightarrow 2\,Al(OH)_3 + 3\,H_3O^+ + 3\,Cl^- \qquad (17)$$

Alloying elements can either increase or decrease the corrosion potential of aluminium alloys. **Figure 22** shows the effects of some alloying elements on the corrosion potentials of aluminium in standard solution according to ASTM G69.

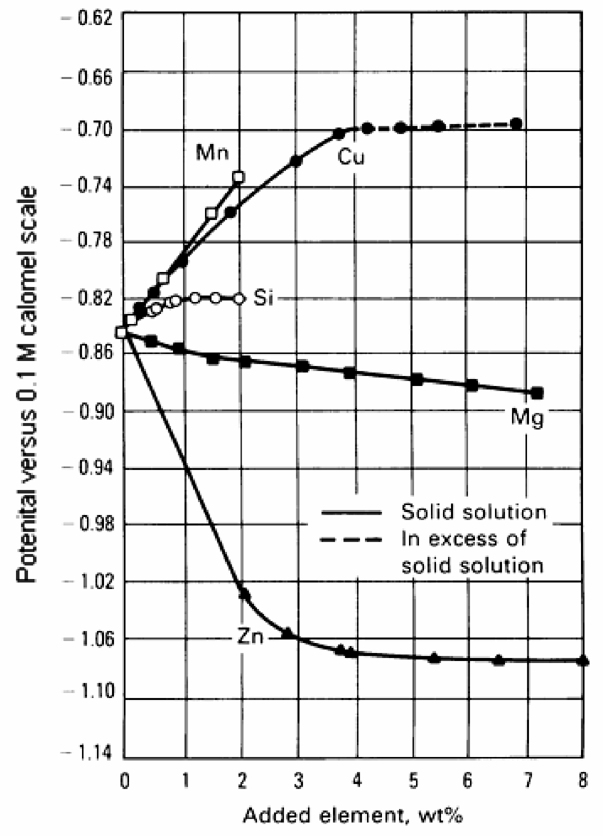

Figure 22 Effects of alloying elements on the corrosion potential of aluminium in 53 g/L NaCl plus 3 g/L H_2O_2 solution at 25°C [29]

The reference electrode used for the test is the *standard calomel electrode*. The concentration of potassium chloride (KCl) for this electrode is defined as 0,1 M instead of saturated KCl in SCE. Its potential shift from SHE is **+336 mV**, which explains the corrosion potential of aluminium without any alloying elements about -840 mV or -750 mV versus SCE.

It has to be emphasized that the condition of alloying elements in **Figure 22** is in a solid solution of the aluminium matrix. The influence of alloying elements as precipitates is different from the solid solution, because the precipitates themselves display different corrosion potentials from the matrix. As heat-treatable aluminium alloys rely on precipitates to gain more strength, the corrosion potentials of heat-treatable alloys are distinguishable in artificial aged conditions (T6-T8), see **Table 5**. The description of the heat treatment conditions can be taken from **Table 6**.

Alloy	Heat treatment condition	E_{Corr} vs SCE in mV
1050A		-750
1100		-740
2024	T3, T4	-600
	T8	-710
2219	T3, T4	-550
	T6, T8	-700
3003		-740
3004		-750

Alloy	Heat treatment condition	E_{Corr} vs SCE in mV
5042		-770
5083		-780
6061	T4	-710
	T6	-740
7075	T6	-740
	T7	-750
8090	T3	-700
	T7	-750

Table 5 Corrosion potentials of some aluminium alloys according to ASTM G69 [5]

Heat treatment condition	Description
T1	Quenched from hot work temperature Natural ageing
T2	Quenched from hot work temperature Strain hardening Natural ageing
T3	Solution heat treatment Strain hardening Natural ageing
T4	Solution heat treatment Natural ageing
T5	Quenched from hot work temperature Artificial ageing

Heat treatment condition	Description
T6	Solution heat treatment Artificial ageing
T7	Solution heat treatment Over ageing
T8	Solution heat treatment Strain hardening Artificial ageing
T9	Solution heat treatment Artificial ageing Strain hardening

Table 6 Definition of the heat treatment condition [47]

These potential differences will lead to the microscopic galvanic couple between the aluminium matrix and precipitates. Liao et al. has monitored the corrosion of polished 2024-T3 alloy in a 0,5 M NaCl solution for 24 hours. The surface before and after the test in **Figure 23** shows that the dissolution of the aluminium matrix took place intensively near the precipitates.

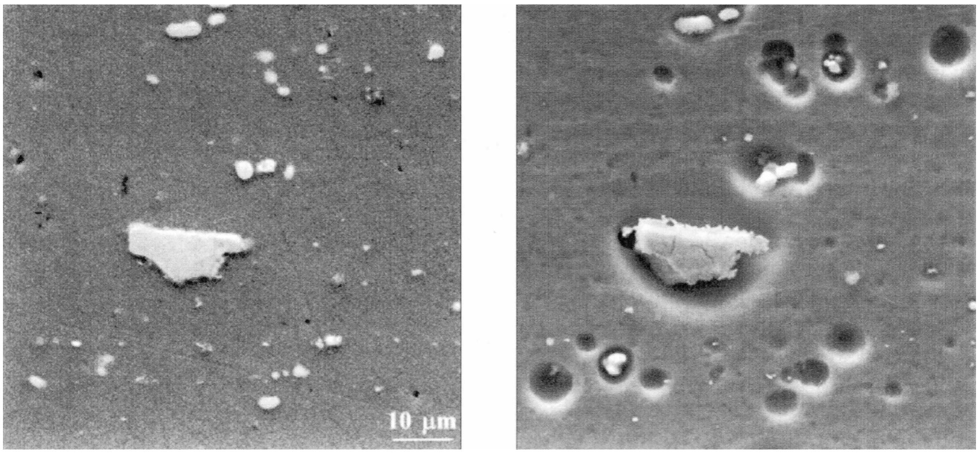

Figure 23 Surface comparison of 2024-T3 alloy before and after immersion in 0,5 M NaCl solution for 24 hours [49]

The corrosion potentials of solid solutions and precipitates can be found in **Table 7**. In general, if the galvanic couple has more than 100 mV corrosion potential difference, the galvanic corrosion has to be taken into consideration. Depending on microstructure, solution type, and the investigator himself, the results can be indicated as galvanic, intercrystalline or even pitting corrosion [5,47,49].

Nevertheless, the galvanic couple is not entirely undesirable. There is a specific type of alloys, which are designed to be less noble. Intentionally, they will be attached to protect another material by forcing the corrosion to occur upon themselves. Hence, they are given the names *sacrificial anodes* or *galvanic anode*.

Solid solution	Precipitate	E_{Corr} vs SCE in mV	Solid solution	Precipitate	E_{Corr} vs SCE in mV
	Si	-170	Al-3Mg		-780
	Al_3Ni	-430	Al-5Mg		-790
	Al_3Fe	-470	Al-1Zn		-850
Al-4Cu		-610		Al_2CuMg	-910
	Al_2Cu	-640		$MgZn_2$	-960
Al-1Mn		-650	Al-5Zn		-970
1050A		-750		Al_3Mg_2	-1150
	Al_6Mn	-760		Mg_2Si	-1190

Table 7 Corrosion potentials of solid solutions and precipitates according to ASTM G69 [5]

Moreover, oxide complexes above the precipitates also have diverse mechanical, chemical and electrochemical properties, which will modify the corrosion behaviour, see **Figure 24**. The volume difference between two oxides will create microscopic flaws on the passive layer. The oxide complexes may not have the same chemical resistance, and electrical conductivity as the passive layer. In general, the smaller precipitates will affect the surface less.

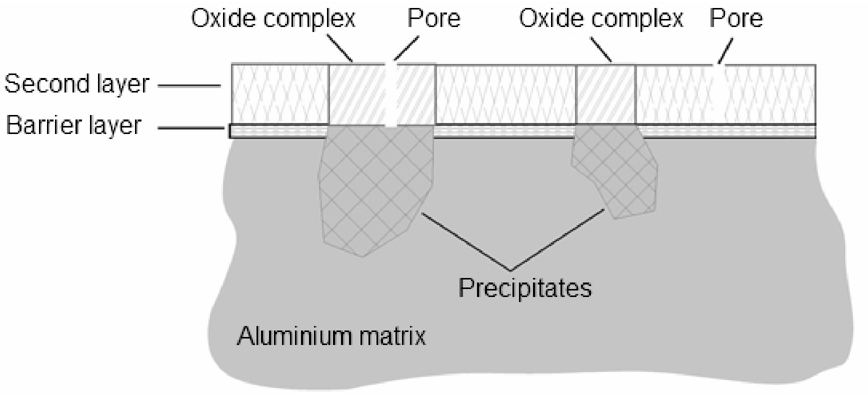

Figure 24 Structure of passive layer in aluminium alloys with precipitates [47]

3. Literature review

In this chapter, the effects of alloying elements added in our samples will be specified. Manganese (Mn) is the main alloying element for the 3000 series commercial wrought alloys. The intermetallic phase formed by scandium (Sc) and zirconium (Zr) is $Al_3(Sc,Zr)$ on the aluminium-rich corner. Therefore these two alloying elements will be reviewed together.

In the third section, the previous investigation results regarding physical properties, such as hardness, extrudability and electrical resistivity will be given for the aluminium alloys containing manganese, scandium and zirconium.

A small amount of antimony (Sb) and tin (Sn) are identified in the sample 3. According to the ASM Handbook, the presence of these elements will affect the passivation behaviour of aluminium in salt water [29]. For this reason, the influence of these elements on the corrosion resistance will also be included in this part.

3.1 Al-Mn alloys

Aluminium-manganese wrought alloy (Al-Mn) is a non-heat-treatable alloy known for its good formability, and corrosion resistance similar to pure aluminium alloys (1000 series). Yet, Al-Mn alloys have a generally higher strength than the 1000 series [50], see **Figure 25**.

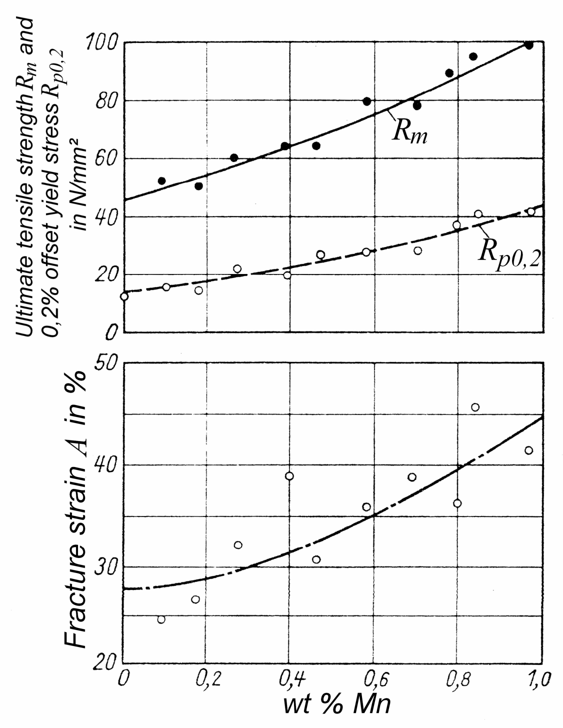

Figure 25 Effects of Mn-addition on the mechanical properties of Al99,95 base material [50]

The Al_6Mn intermetallic phase is a common phase on the Al-Mn alloys. The Al-Mn phase diagram on the aluminium-rich corner is shown in **Figure 26**. Aluminium and Al_6Mn form an eutectic system with the eutectic point at 1,95 wt% Mn. The maximum solubility of manganese in aluminium is 1,82 wt% at the eutectic temperature of 658°C.

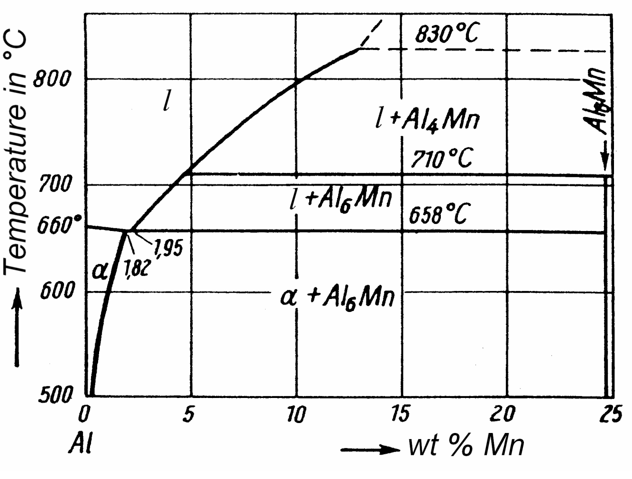

Figure 26 Phase diagram of the Al-Mn binary system [51]

The manganese solubility in aluminium declines rapidly as the temperature decreases as shown in **Table 8**. However, the aluminium matrix tends to be oversaturated with manganese in practical solidification. As an example see **Figure 27** for the microstructure of Al-1,9Mn cast alloy. It is obvious that despite the near-to-eutectic concentration of manganese, the alloy is solidified with only a little amount of eutectic structure. The oversaturation can be enhanced further in the manufacturing processes. This is the reason, why the manganese concentration can be as high as 1,5 wt% in commercial wrought alloys (3000 series) regardless of Al_6Mn formation [6,52].

Temperature in °C	**wt% Mn**
658[a]	1,82
626	1,35
600	0,95
570	0,78
500	0,36
400	0,09
300	0,02
200	0,003

[a]) eutectic temperature of Mn

Table 8 Solubility of manganese in aluminium [50-52]

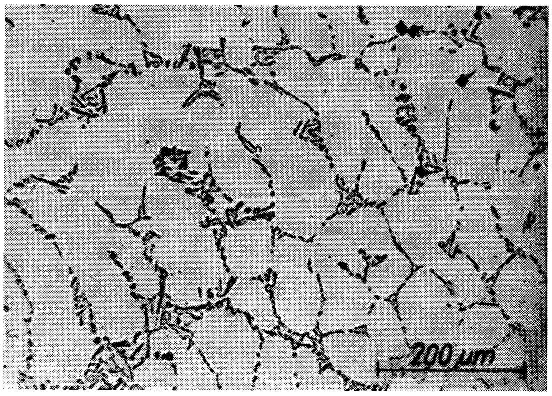

Figure 27 Microstructure of cast aluminium with 1,9 wt% Mn (magnification 100:1) [51]

Recrystallisation behaviour

The manganese addition up to about 1 wt% will raise the recrystallisation temperature from 250-300°C of the 1000 series alloys to 300-350°C [53-57]. The investigation by N. H. Lee et al. shows partial recrystallisation of aluminium alloy with 0,24 wt% Mn after annealing at 300°C, whereas no change is observed in aluminium alloy with 0,74 wt% Mn after the same annealing [56], see **Figure 28**.

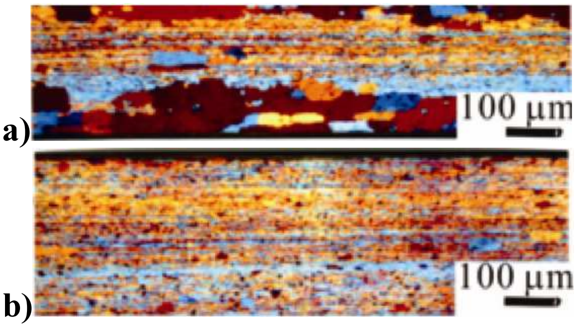

Figure 28 Microstructure of 95,5% cold-rolled aluminium alloys with **a)** 0,24 wt% Mn and **b)** 0,74 wt% Mn after annealing at 300°C for 3 hours [56]

Nevertheless, the recrystallisation temperature found in literature depends on several parameters, e.g., other alloying elements, deformation rate and annealing time as well. The formation of Al_6Mn intermetallic phase is suggested to benefit the recrystallisation resistance. W.C. Liu and B. Radhakrishnan have demonstrated diverse recrystallisation possibilities of the AA3003 alloy (EN AW-Al Mn1Cu) by annealing at different temperatures [58].

The recrystallisation at 371°C annealing in **Figure 29** displays similar recrystallisation as in **Figure 28a**. At 399°C annealing, the recrystallisation has started from the middle of the sample. This is in contradiction to the general concept of recrystallisation, in which the recrystallisation should have started from high dislocation density such as on the top and bottom of cold-rolled surfaces.

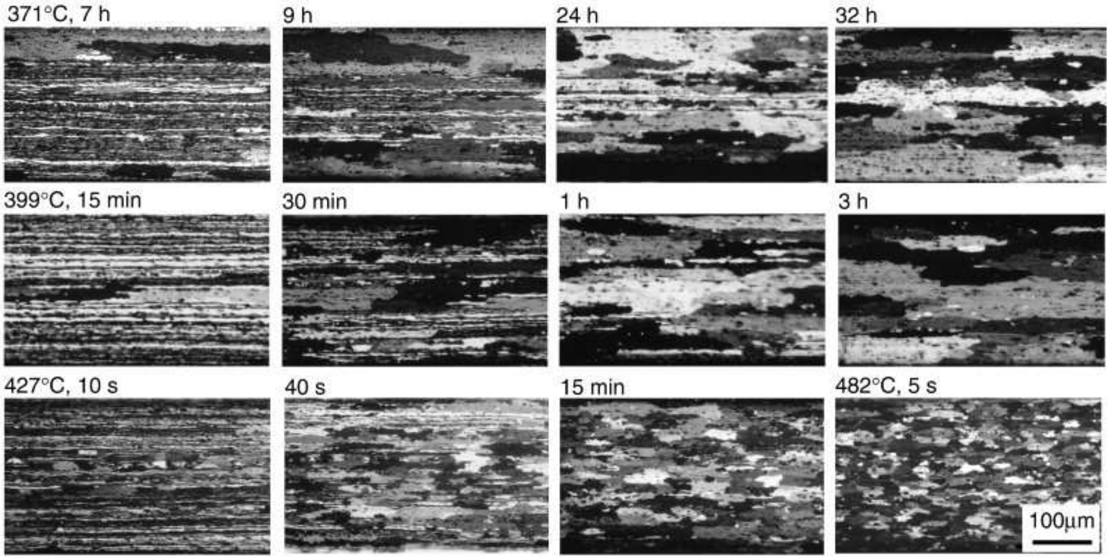

Figure 29 Microstructure of 90% cold-rolled 3003 alloy annealed at different temperatures [58]

The reason for this phenomenon is, the Al_6Mn intermetallic phase precipitated at high temperature is able to pin down the migrating grain boundary during the recrystallisation. The fine recrystallised grains from the annealing at 427°C and 482°C are explained by the formation of finer and more disperse Al_6Mn precipitates.

Corrosion behaviour

In general, the alloying elements in the matrix are depleted by the formation of the precipitation. The corrosion potential of the depleted matrix may be considered about the value of the 1000 series (-750 mV versus SCE).

In case of Al-Mn alloys, Al_6Mn shows almost the same corrosion potential (-760 mV) as the 1000 series, see **Table 7**. Therefore, the Al-Mn alloys are much less susceptible to corrosion reaction induced by the microscopic galvanic couple.

3.2 Al-Sc-Zr alloys

Scandium and zirconium are transition metals with the atomic numbers 21 and 40 respectively. Unlike manganese, these elements are not the main alloying elements of any commercial aluminium alloys. Both elements have low solubility in aluminium, which decrease rapidly with decreasing temperature as shown in **Table 9**. Under practical conditions, these elements tend to be oversaturated in the solid solution, because of the narrow temperature interval between the melting point of aluminium at 660°C and the temperature of the eutectic reaction of scandium as well as that of the peritectic reaction of zirconium. In the literatures, the eutectic temperature of scandium is between 655-660°C [59,60]. For zirconium, its peritectic temperature is 660-663°C [61].

T in °C	wt% Sc[a]	wt% Zr
663[b]	-	0,28
655[c]	0,35	-
640	0,31	0,23
600	0,22	-
500	0,08	0,14
450	-	0,11
350	-	0,08

[a]) recalculated from at%
[b]) peritectic temperature of Zr
[c]) eutectic temperature of Sc

Table 9 Solubility of scandium and zirconium in aluminium binary system [59]

The binary phase diagram of system Al-Sc and Al-Zr are displayed in **Figure 30** and **Figure 31** respectively. The intermetallic phases formed at the aluminium-rich corner have the same stoichiometry, namely Al_3Sc and Al_3Zr.

More importantly, the Al_3Zr does not precipitate as a stable tetragonal type $D0_{23}$ during heat treatment. Instead, a metastable face-centred cubic (FCC) type $L1_2$ is formed, which is the same structure as the stable Al_3Sc [12,13,40,62,63]. This coincidence allows the solubilities of 34-36 wt% zirconium in Al_3Sc and 5 wt% scandium in Al_3Zr at 600°C [59]. Their corresponding isothermal section is shown in **Figure 32**. Thus, both Al_3Sc and Al_3Zr are commonly referred to altogether as $Al_3(Sc_x,Zr_{1-x})$ or just $Al_3(Sc,Zr)$ [11,63-66].

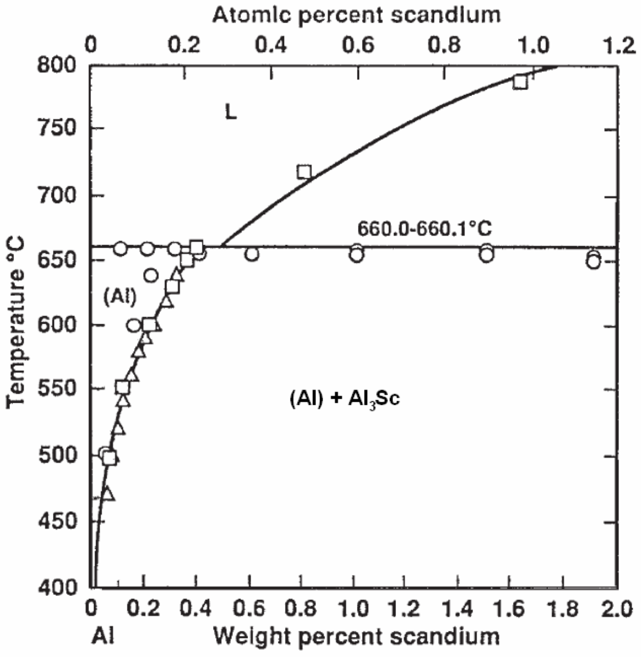

Figure 30 Phase diagram of the Al-Sc binary system [60]

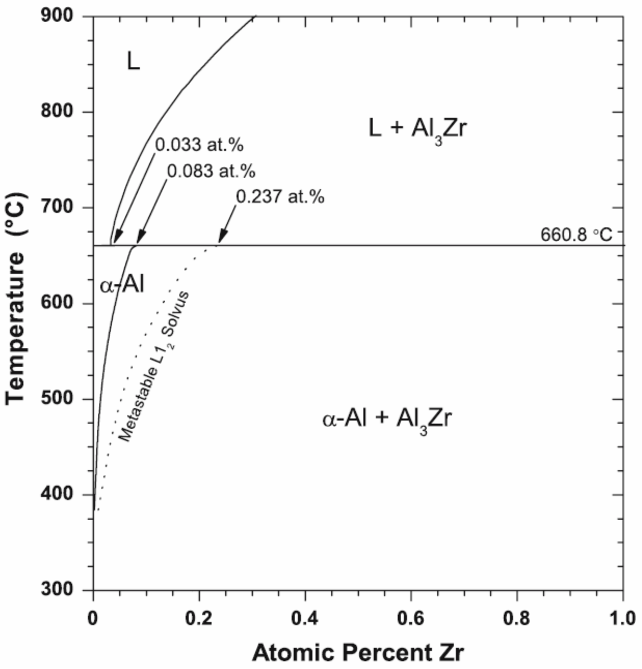

Figure 31 Phase diagram of the Al-Zr binary system [61]

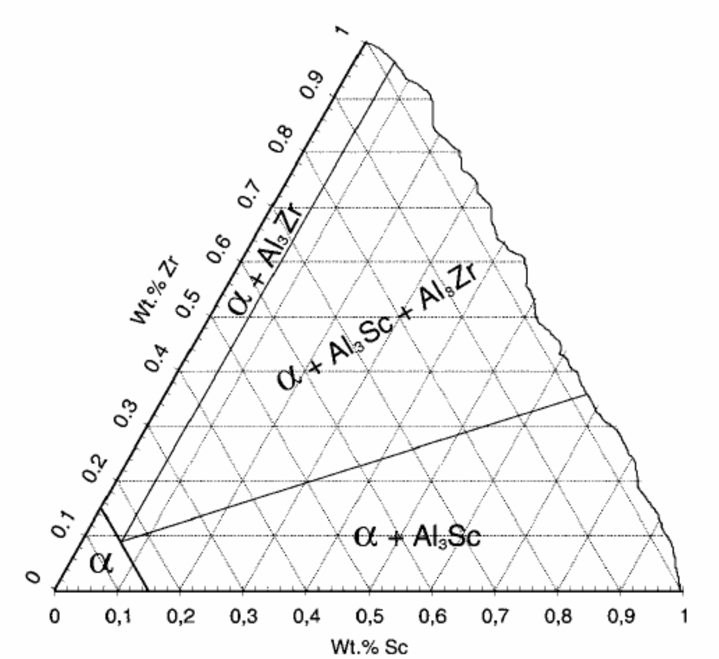

Figure 32 Isothermal section of the aluminium-rich corner of Al-Sc-Zr system at 600°C [37]

The advantages of $Al_3(Sc,Zr)$ compared to Al_3Sc and Al_3Zr are the uniform distribution and the temperature stability of the precipitates. At first glance, these combined benefits do not seem to be compatible with each other. The uniform distribution can be explained by the high diffusivity of scandium over zirconium, see **Figure 33** and **Figure 34**. The investigation by Jia Zhi-hong et al. indicates that the 0,05 wt% addition of scandium will decrease the radius of the precipitates dramatically, while further addition will mainly increase the number density of the $Al_3(Sc,Zr)$ precipitates [14].

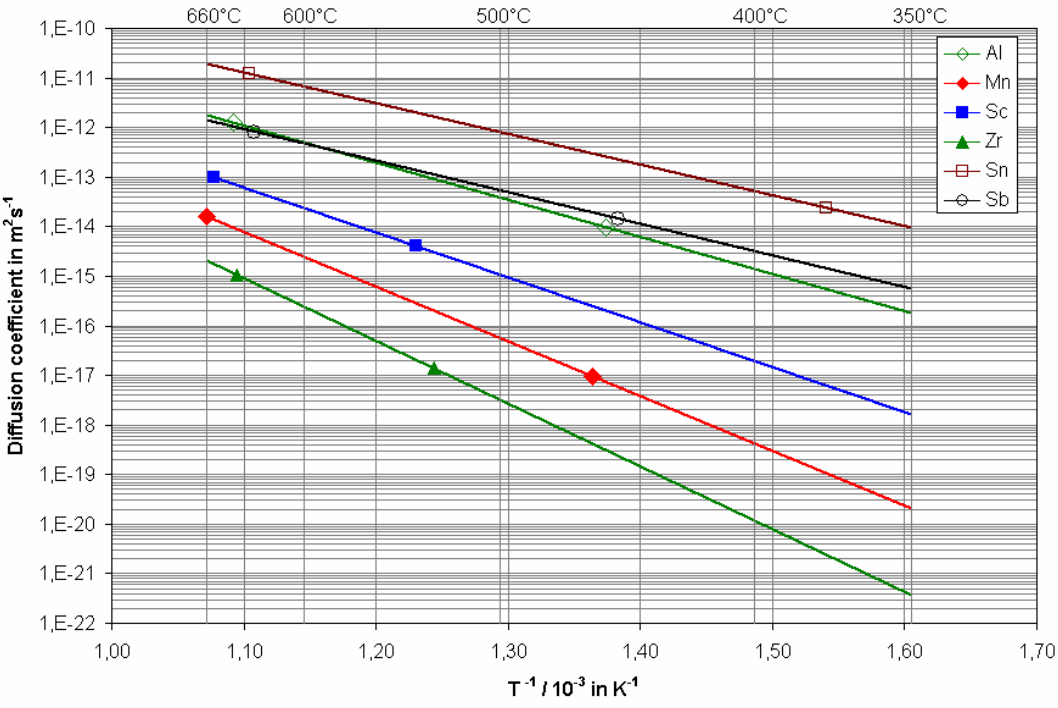

Figure 33 Arrhenius plot comparing diffusion coefficients of impurities in pure aluminium between temperature range 350 and 660°C, extrapolated from the data in references 67-72

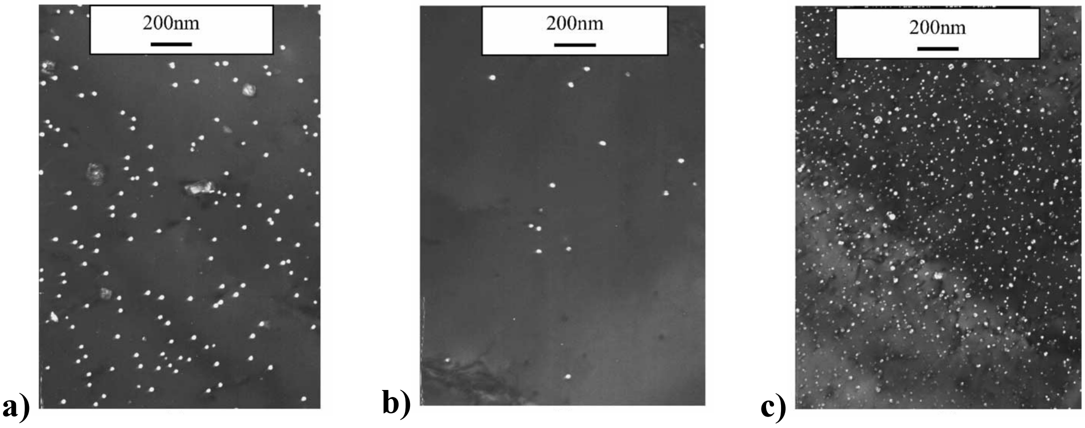

Figure 34 Area with **a)** high and **b)** low density of the Al_3Zr precipitates and the **c)** uniform distribution of $Al_3(Sc,Zr)$ in Al-Mn-Zr alloys without and with Sc respectively [11]

By analogy of the diffusivity, the coarsening of the precipitates containing scandium should have been easier too, but instead, the $Al_3(Sc,Zr)$ precipitates are stabilised by the addition of zirconium [7,13,65]. The alloys containing $Al_3(Sc,Zr)$ show considerably better temperature resistance than the alloys containing Al_3Sc. The hardness drop from the coarsening of the precipitates is distinguishable in Al-0,3Sc alloy as compared to Al-0,2Sc-0,04Zr alloy at a temperature above 350°C, see **Figure 35**.

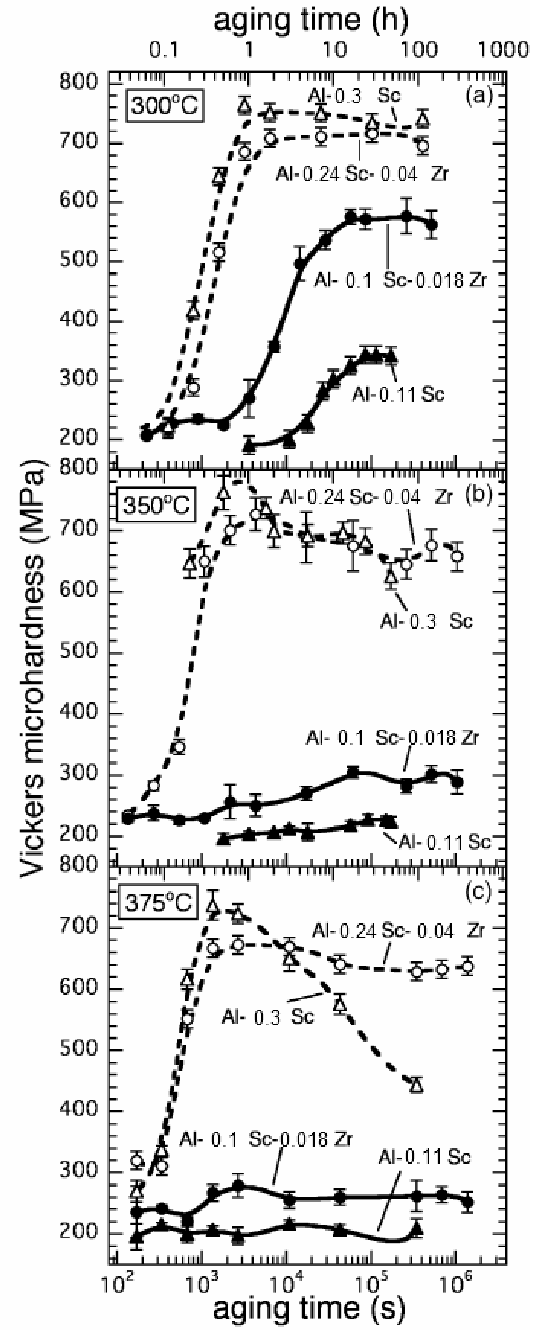

Figure 35 Hardness development of Al-Sc alloys[a] with and without Zr during isothermal annealing at **a)** 300°C, **b)** 350°C and **c)** 375°C [65]

[a]) For the consistency, the alloy compositions in the figure are recalculated from at% to wt%.

Further understanding of this phenomenon is provided by the investigation using three dimensional atom probe analyses [73]. The concentration profile of an $Al_3(Sc,Zr)$ precipitate is displayed in **Figure 36**. The precipitate consists of the Al_3Sc core and the zirconium-rich $Al_3(Sc,Zr)$ shell as shown in **Figure 37**.

The precipitation kinetics has been suggested by Lefebvre et al. [74] as follows: At 250°C, the scandium is able to diffuse, while zirconium remains stationary. The formation of the Al_3Sc precipitates is controlled by scandium diffusion, until the diffusion of zirconium becomes significant from 350°C [12,39]. The zirconium is enriched at the precipitate interfaces, and the zirconium-rich $Al_3(Sc,Zr)$ shells are formed.

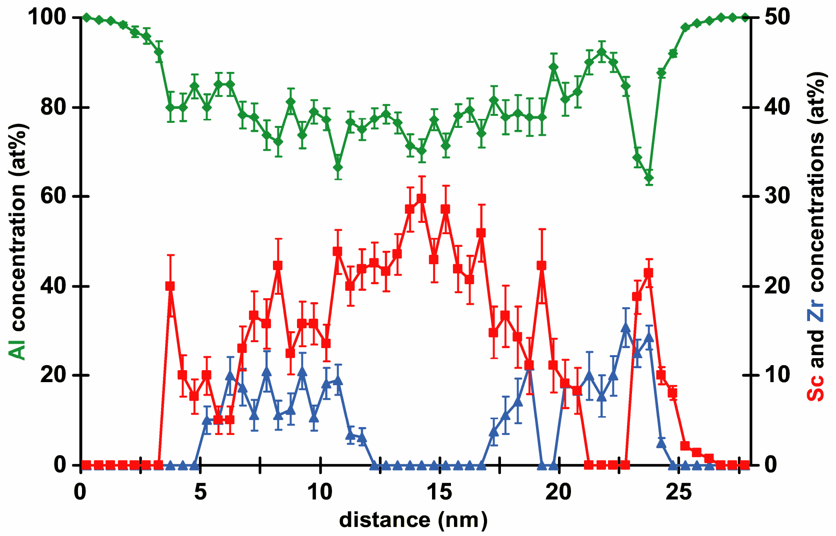

Figure 36 Concentration profile of an $Al_3(Sc,Zr)$ precipitate in Al-0,15Sc-0,08Zr heated from room temperature with 50°C/h and hold at 475°C for 15 hours [73]

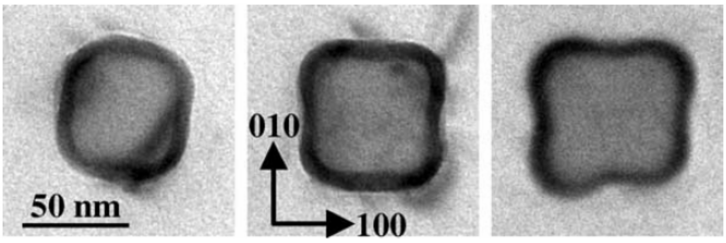

Figure 37 An $Al_3(Sc,Zr)$ precipitate in Al-0,61Sc-0,4Zr after annealing at 450°C for 69 hours [38]

The temperature resistance of aluminium alloy containing zirconium at 375°C in **Figure 35** can be explained by the low diffusivity of zirconium, as the coarsening of the precipitates is controlled by the zirconium diffusion [40].

3.3 Al-Mn-Sc-Zr alloys

Addition of manganese does not affect the solubility of scandium in aluminium, while scandium decreases the manganese solubility. The solubilities of manganese and scandium have been reported as Al-0,2Mn-0,08Sc at 500°C and Al-0,55Mn-0,2Sc at 600°C [59], compare with **Table 8** and **Table 9**. No ternary phase has been reported in the Al-Mn-Sc system. The ternary eutectic temperature of (Al), Al_6Mn and Al_3Sc is 649°C.

In the Al-Mn-Zr system, two ternary phases have been reported as Al_6Mn_6Zr and $Mn_2(Al_x,Zr_{1-x})$. The latter is formed by the substitution of aluminium atoms in Mn_2Zr [75]. Since both phases are not found in the aluminium-rich corner, they will not be taken into consideration in this work.

The isothermal sections of the tetrahedron system Al-Mn-Sc-Zr with 0,18 wt% Sc are constructed by Rokhlin et al. [76]. No manganese-rich phase other than Al_6Mn has been reported at the aluminium-rich corner between 500-640°C, see **Figure 38**. The scandium and zirconium are determined in the Al_3Zr and Al_3Sc precipitates respectively, which confirm the existence of the $Al_3(Sc,Zr)$ precipitates in the Al-Mn-Sc-Zr system. Their solubilities are negligible in Al_6Mn precipitates.

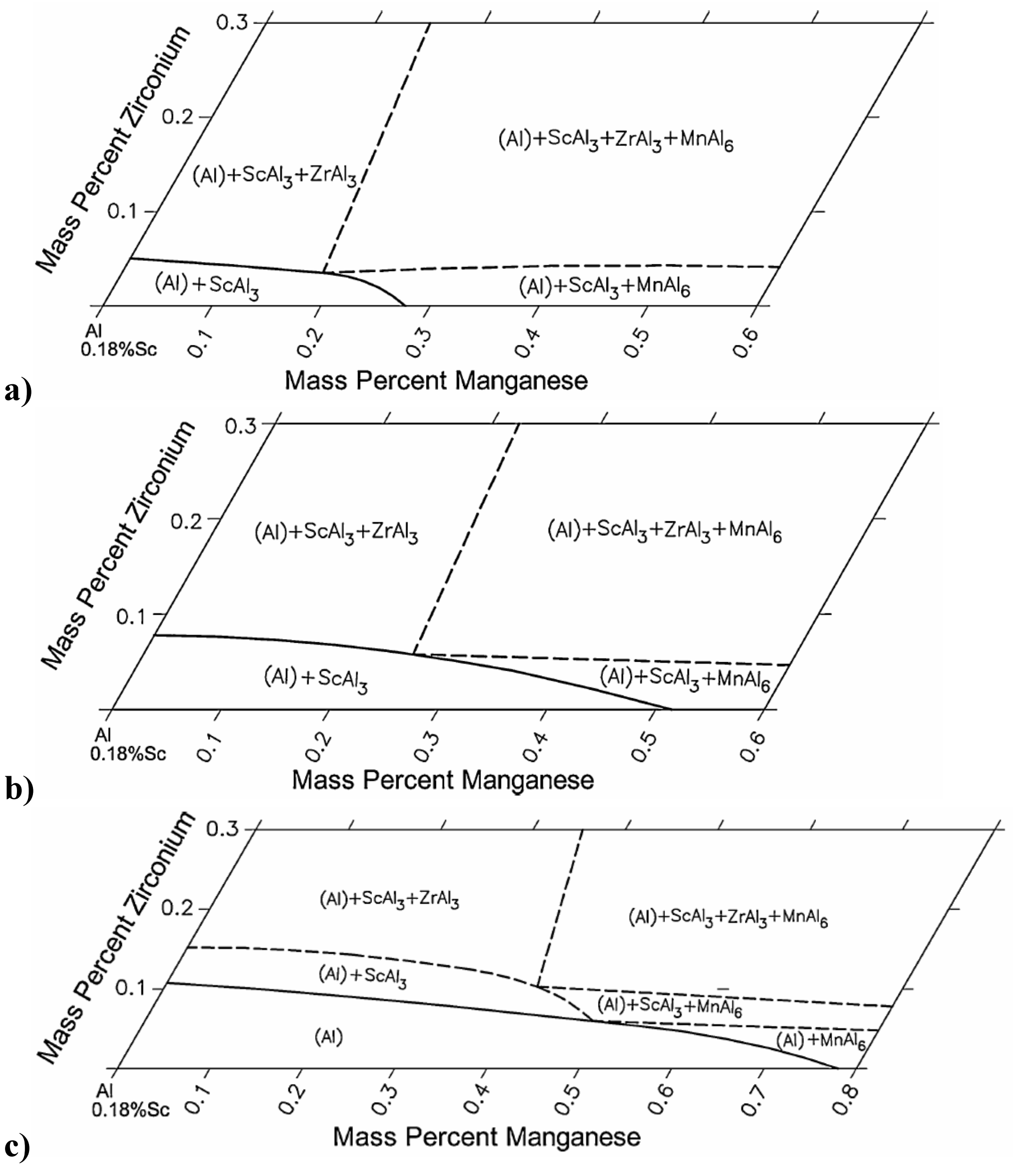

Figure 38 Isothermal section of the aluminium-rich corner with 0,18 wt% Sc of Al-Mn-Sc-Zr system at **a)** 500°C, **b)** 600°C and **c)** 640°C [77]

His further investigation also discovers that the aluminium alloy containing 0,34 wt% Mn, 0,13 wt% Sc and 0,053 wt% Zr shows the first sign of the recrystallisation after the annealing at 600°C for 1 hour , whereas Al-0,79Mn-0,17Sc-0,12Zr has to be annealed at 630°C for the same duration before the recrystallisation can be observed.

Forbord et al. suggests that the manganese addition has neither effect on the formation nor on the coarsening kinetics of $Al_3(Sc,Zr)$ in extruded Al-0,91Mn-0,17Sc-0,13Zr [39,40]. No recrystallisation can be observed in the samples with and without the precipitation annealing at 450°C for 12 hours prior to the hot extrusion, and their extrudabilities are also the same. These results indicate the rapid precipitation of $Al_3(Sc,Zr)$ within 5 minutes of pre-heating or during the hot extrusion at 480°C. The shorter production route can be made due to the unnecessity of an extra precipitation annealing.

The effect of cold roll has been studied in Al-1,26Mn-0,24Sc-0,13Zr by Vlach et al. [78,79]. The electrical resistivity measurements display the same change in resistivity during the $Al_3(Sc,Zr)$ precipitation in all samples, while the stronger response for the precipitation of Al_6Mn can be distinguished in 50% cold-rolled sample. The response is even stronger in the 75% cold-rolled sample.

3.4 Al-Sb and Al-Sn alloys

In the binary system of aluminium (Al) and antimony (Sb), aluminium is in the equilibrium of the eutectic type with the intermetallic phase, aluminium antimonide (AlSb), at 657°C, see **Figure 39**. The solubility of antimony in aluminium is 0,1 wt% at the eutectic temperature. Aluminium also forms the eutectic system with tin (Sn) at 228°C as shown in **Figure 40a**.

Normally, the maximum solubilities of eutectic, peritectic as well as monotectic systems lie upon the temperatures of the associated invariant reactions. However, the Al-Sn system possesses a unique aluminium solid solution. **Figure 40b** shows the *retrograde solubility* at the aluminium-rich corner [80]. While aluminium has practically no tin solubility at the eutectic temperature (0,02 wt%), the tin solubility in aluminium is reported to be 0,026 at% or about 0,12 wt% at 625±20°C [81]. This extended solubility will play an important role in the specific resistivity result.

The eutectic temperature of the ternary system Al-Sb-Sn is 227°C, located at about 99 wt% Sn. The isothermal section of Al-Sb-Sn system at 200°C is displayed in **Figure 41**. According to the database, no ternary phase has been reported [82]. The equilibrium phases consist of an aluminium solid solution, almost pure tin and AlSb.

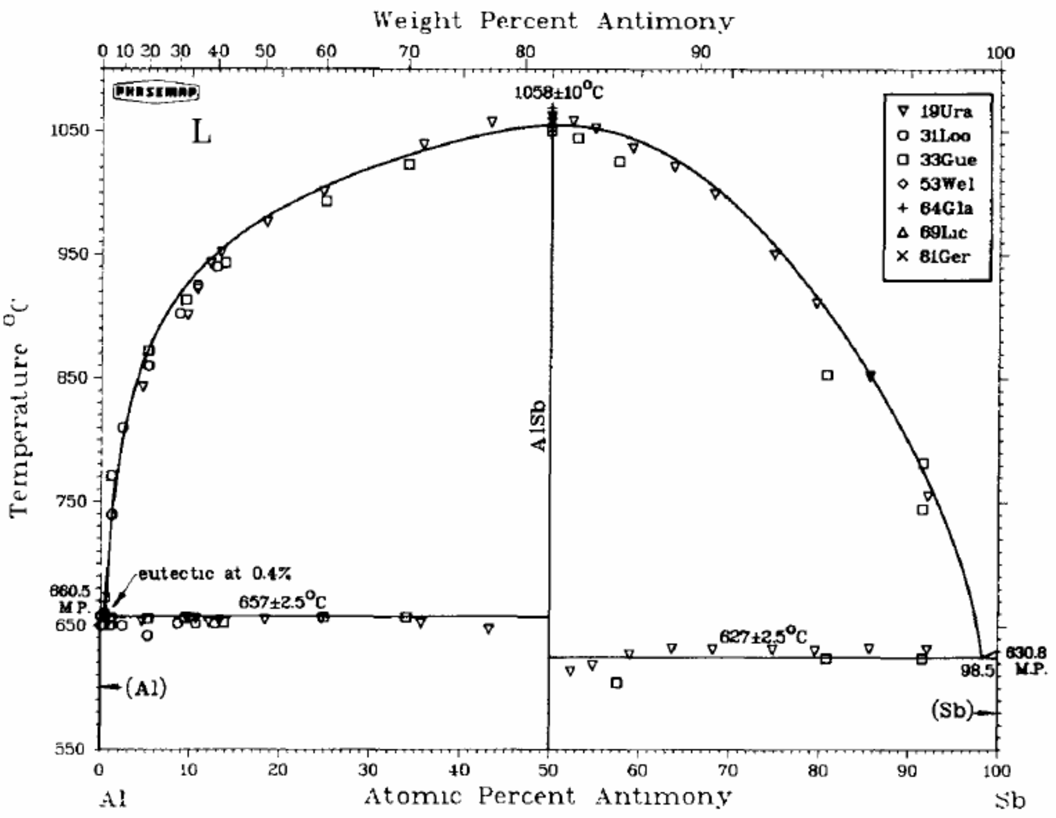

Figure 39 Phase diagram of the Al-Sb binary system [83]

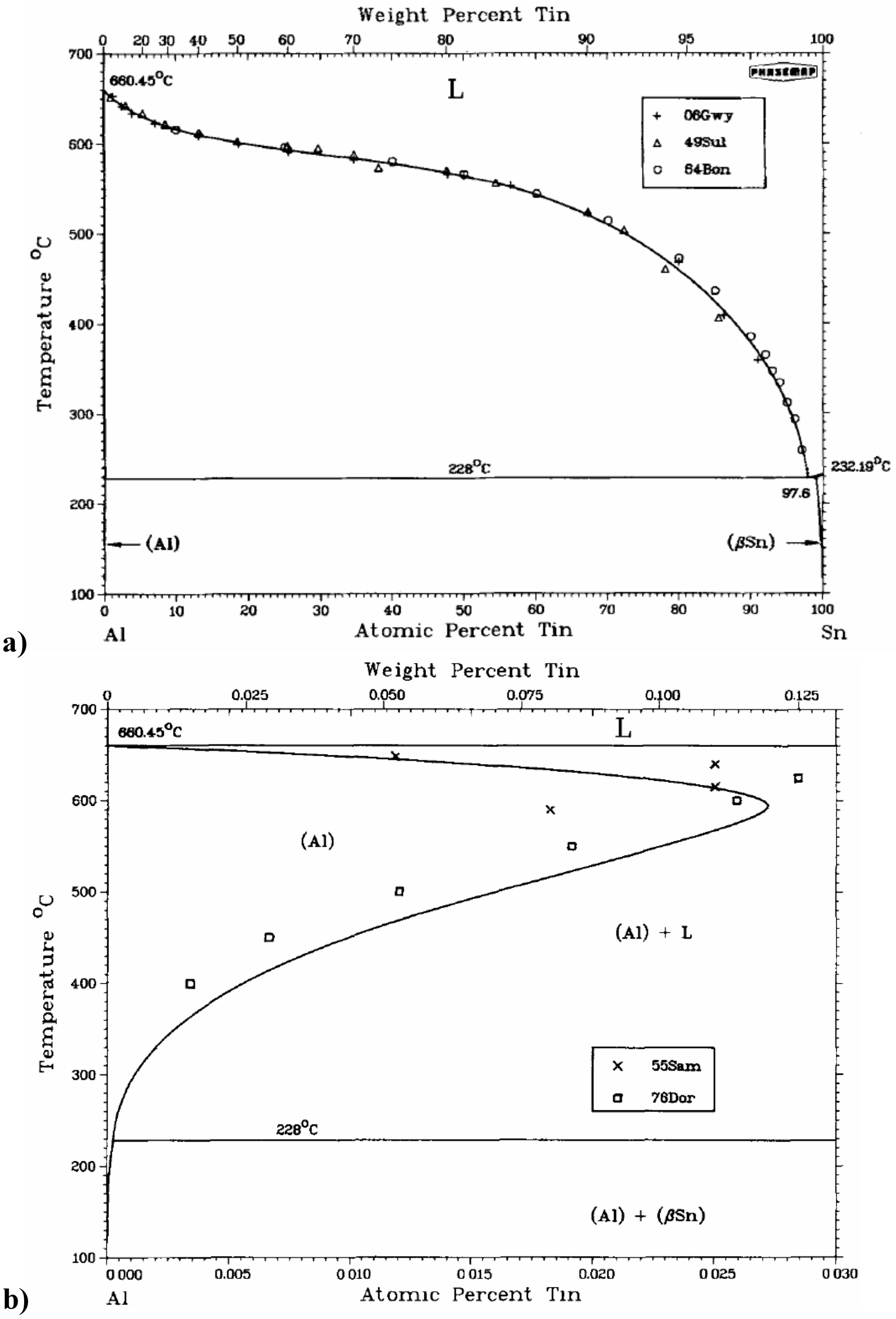

Figure 40 Phase diagram of **a)** the Al-Sn binary system and **b)** the retrograde solubility at the Al-rich corner showing retrograde solubility [81]

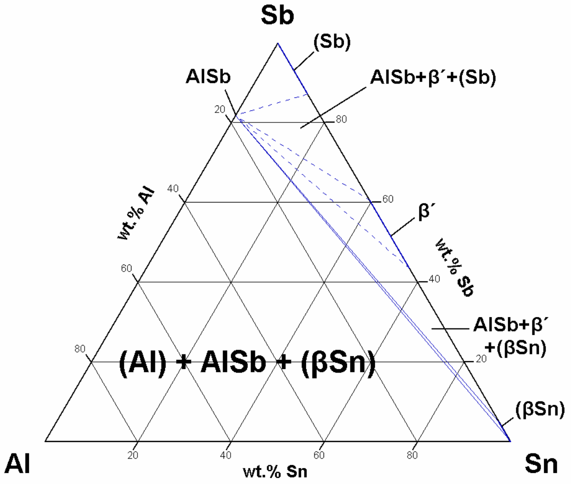

Figure 41 Isothermal section of the Al-Sb-Sn system at 200°C [82]

Although antimony (Sb) and tin (Sn) are used to inhibit dezincification, a selective corrosion attack, and enhance corrosion resistance of brasses respectively [29], these elements behave differently in aluminium alloys.

The polarisation result from Krasovskii indicates that the addition of antimony up to 0,1 wt% will improve the corrosion potential (E_{Corr}) via a more stable passive layer, which is in compliance with the claim made in ASM Handbook [80,84].

However, his potentiodynamic polarisation results also show the earlier emersion of pitting corrosions. In other words, the passive state becomes narrower as the antimony content increases, see **Figure 42**. So, in a sense, the addition of antimony could be considered as the negative effect on aluminium alloys.

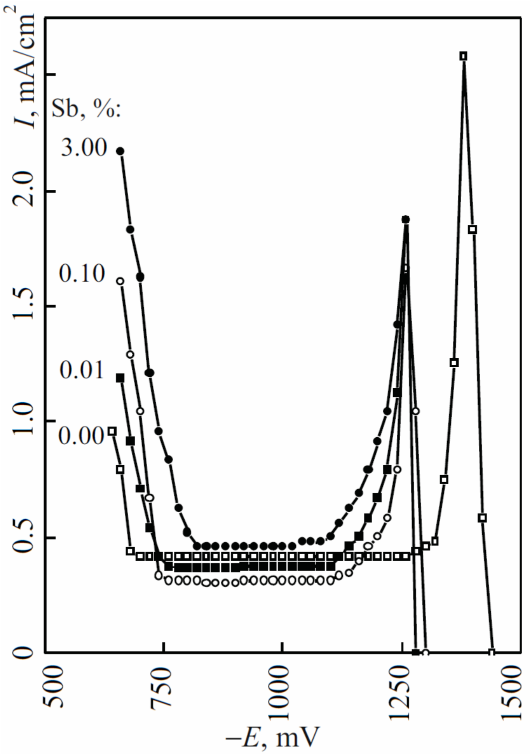

Figure 42 Polarisation curve of Al-Sb with different concentrations of antimony in 1 M NaCl solution [84]

Tin is known to suppress the passivation of aluminium. Even 0,01 wt% Sn is enough to make aluminium alloys susceptible to corrosion [80]. The effect is so remarkable that about 0,1-0,2 wt% tin is added together with 5-8 wt% zinc to make a sacrificial anode for offshore construction [5,29,85], see also chapter 2.2.4.

Erb and Aust proposed the corrosion mechanism of the aluminium alloy containing 0,13 wt% Sn in 20% hydrochloric acid as the pitting corrosion initiated by the tin-rich particles [86]. The surface will not be passivated if the mean distance between the tin-rich particles is smaller than the diameter of the pits themselves because the further particles will be exposed to the corrosive medium.

The potentiostatic polarisation curves of aluminium alloys containing 0,02 and 0,4 wt% Sn were performed in a 2 M NaCl solution by Kliškić et al. [87], see **Figure 43**. Before the results are elaborated further, it should be pointed out that the samples were polarised from the anodic to cathodic area as opposed to the polarisation of this work. To avoid any confusion, all characteristic parameters are re-labelled as the definitions in chapter 2.1.3.3.

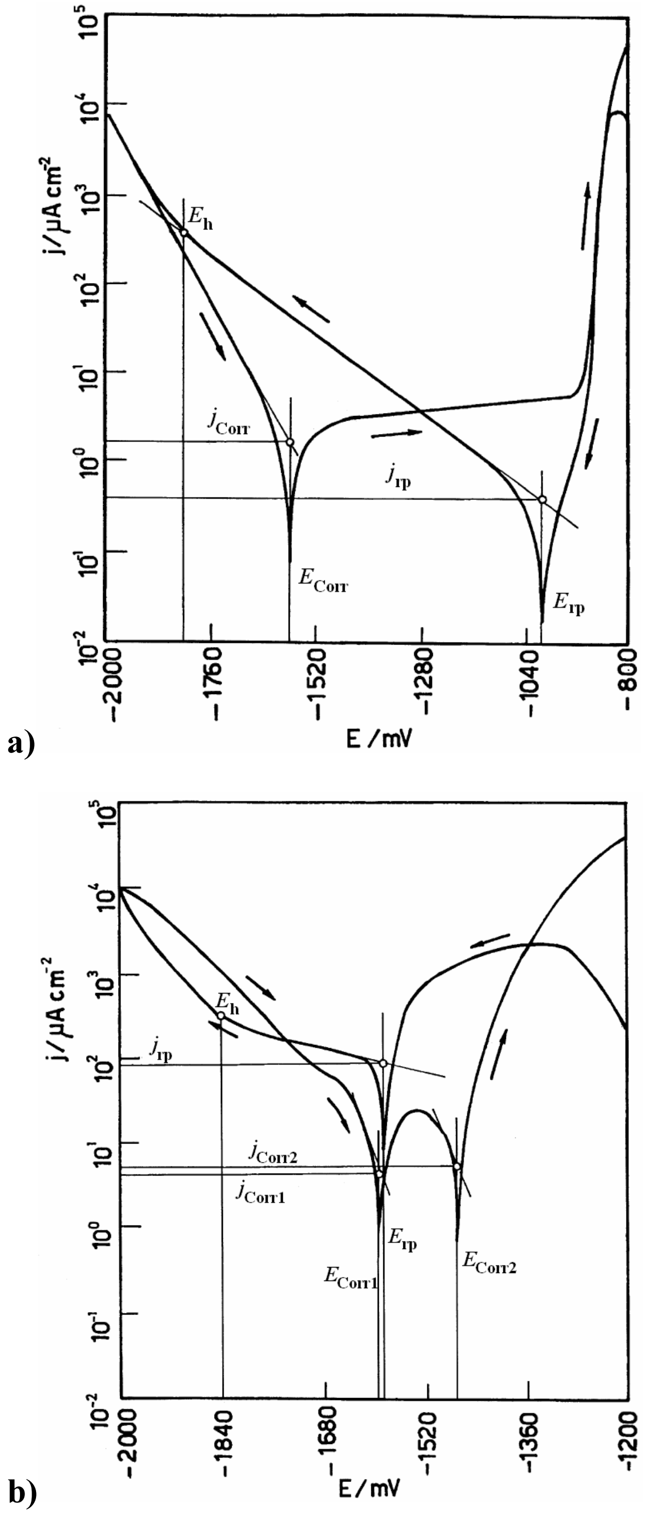

Figure 43 Polarisation curve of **a)** Al-0,02Sn and **b)** Al-0,4Sn in 2 M NaCl solution [87]

From his result, the 0,4 wt% tin addition will shift the open-circuit potential (OCP) about 350 mV in the negative direction in comparison to pure aluminium, whereas the OCP is not affected by 0,02 wt% tin addition.

During the polarisation from the cathodic to the anodic area, the alloy containing 0,02 wt% Sn shows the passivation behaviour. In case of the alloy containing 0,4 wt% Sn, this plateau is replaced by another corrosion potential E_{Corr2}, which indicates the activation of the surface by tin. For this reason, only one potential, E_{rp}, can be found during the scan in the opposite direction. Additionally, E_{h} is the hydrogen evolution potential, which is outside the polarisation range in this work.

4. Experimental procedures

This work will focus on the changes of hardness, electrical resistivity and corrosion behaviour of a novel aluminium alloy after several heat treatments. All tests will be performed on the samples from the same alloy produced by casting. In total, three samples are produced from this alloy. The samples are distinguished by the different production routes, namely the cast, cast-extruded and cast-atomized-extruded samples. They will be designated as sample 1, 2 and 3 respectively.

4.1 Samples preparation

The novel alloy Al-1,5Mn-0,3Sc-0,15Zr was prepared by melting 99,9% aluminium, Al-10Mn, Al-2Sc and Al-10Zr master alloys in a resistance furnace at 850°C. This alloy composition was chosen from the maximum concentrations indicated by the commercial Al-Mn alloys and from the previous studies [6,7,12,52]. The alloy was cast into a cylindrical steel mould with 7 cm diameter. Subsequently, the alloy was cut into three pieces. One of them was taken as sample 1.

Sample 2 was made by heating the alloy to 350°C for 1 hour with following extrusion to 1,5 cm diameter bar. For sample 3, the alloy was remelted and atomised under protective atmosphere. The powder was compacted by cold isostatic pressing (CIP). Finally, the compacted cylinder was extruded in the same manner as sample 2. **Figure 44** illustrates the preparation processes of three samples.

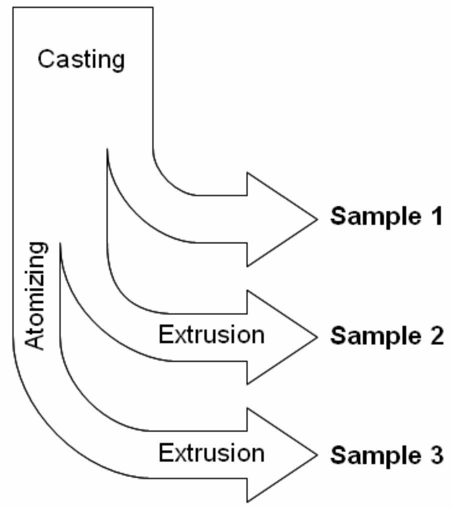

Figure 44 Sample overview

The powder composition was verified by X-ray fluorescence spectroscopy (XRF), and the compositions of the samples were determined by spectral analysis (Clausthal University of Technology). It should be noted that the scandium content could not be obtained from the latter method. Therefore, the scandium content as well as the other intentionally alloyed elements were verified by the inductively coupled plasma (ICP) method (IfG-Service GmbH). The compositions are listed in **Table 10**.

Sample		**Composition in wt%**									
		Al	**Mn**	**Sc**	**Zr**	**Sb**	**Sn**	**Mg**	**Si**	**Fe**	**Cu**
1	SA	Bal.	1,60	n/a	0,15	0,00	0,00	0,00	0,03	0,11	0,00
	ICP	-	1,38	0,26	0,16	-	-	-	-	0,10	-
2	SA	Bal.	1,52	n/a	0,15	0,00	0,00	0,00	0,03	0,10	0,00
	ICP	-	1,38	0,27	0,19	-	-	-	-	0,09	-
3	SA	Bal.	1,59	n/a	0,14	0,04	0,23	0,04	0,03	0,10	0,02
	ICP	-	1,50	0,22	0,18	-	-	-	-	0,10	-
Powder	XRF	Bal.	2,45	0,30	0,24	-	0,35	-	0,06	0,17	0,02
	ICP	-	1,42	0,21	0,17	-	-	-	-	0,10	-

Table 10 Chemical compositions verified by spectral analysis (SA), inductively coupled plasma (ICP) and X-ray fluorescence spectroscopy (XRF)

4.2 Heat treatment

The samples were annealed in two different programmes. The first programme was the accumulative annealing in eight steps in total. During this heat treatment, the following tests were performed: the hardness, resistivity and potentiostatic electrochemical measurement. The other heat treatment is the recrystallisation annealing to demonstrate the recrystallisation in the extruded samples.

4.2.1 Step annealing

All samples were annealed stepwise in a resistance furnace at constant temperatures ranging from 200°C to 600°C. The course of the annealing steps will be referred to as *stage*. The overview of the heat treatments can be found in **Table 11**. After each step, the samples were quenched in water to room temperature in order to proceed to the test methods in chapter 4.4, 4.5 and 4.6.

Stage	**Steps of annealing**						
1	as cast / as extruded						
2	200°C 1 h						
3	200°C 1 h	+ 300°C 1 h					
4	200°C 1 h	+ 300°C 1 h	+ 400°C 1 h				
5	200°C 1 h	+ 300°C 1 h	+ 400°C 1 h	+ 500°C 1 h			
6	200°C 1 h	+ 300°C 1 h	+ 400°C 1 h	+ 500°C 1 h	+ 600°C 1 h		
7	200°C 1 h	+ 300°C 1 h	+ 400°C 1 h	+ 500°C 1 h	+ 600°C 1 h	+ 600°C 1 h	
8	200°C 1 h	+ 300°C 1 h	+ 400°C 1 h	+ 500°C 1 h	+ 600°C 1 h	+ 600°C 1 h	+ 600°C 1 h

Table 11 Annealing steps

4.2.2 Recrystallisation annealing

For the sake of comparison, sample 2 and 3 were annealed at 600°C for 48 hours in order to observe the recrystallisation. For this heat treatment, only the metallography was performed on the samples.

4.3 Characterisation methods and metallography

The microstructure of the samples was characterised using a light microscope and a scanning electron microscope (SEM). Due to the size of the atomised powder, the presence of the phases was detected by X-ray diffraction (XRD). The phase compositions were determined by the energy dispersive X-ray spectroscopy (EDX). The observation of fibrous microstructure in sample 2 and 3 was made by the electron backscatter diffraction (EBSD). Transmission electron microscopy (TEM) was used to determine the $Al_3(Sc,Zr)$ precipitate.

The metallographic specimens were ground down with silicon carbide (SiC) paper, and subsequently polished with an oxide polishing suspension. The surfaces were etched according to the examination methods.

For general observation of the microstructure with a microscope, the samples were electrolytically etched with Barker's etchant, diluted HBF_4 in distilled water. This was done to distinguish the grains depending on their orientations.

Flick's etchant, diluted HCl and HF in distilled water, was used to make the Al_6Mn precipitates visible. As opposed to Barker's etchant, the surface was not excessively oxidised. Thus, the investigation with SEM was not interfered. The compositions of alloying elements across the grain were measured with EDX.

Due to the deformed structure of sample 2 and 3, the observation of the microstructure was carried out by EBSD. After the mechanical polishing, the specimens for EBSD as well as TEM were electrolytically polished with diluted $HClO_4$ and HNO_3 in ethyl alcohol.

4.4 Hardness measurement

The Vickers hardness was measured according to DIN EN ISO 6507-1 with a 49,03 N load (HV5) and 15 s loading time, see chapter 2.1.1. After quenching, the samples were ground down with 1200-grit silicon carbide (SiC) paper to remove the oxide layer from the heat treatment. In this work, the hardness values are the average of 5 measurements.

The hardness measurement was performed on the middle area of the cross section in sample 1, which was the position with the slowest cooling rate during casting. The hardness of sample 2 and 3 was obtained from the section parallel to the extrusion.

4.5 Resistivity measurement

The electrical resistivity was measured using the DC four-point method. The pre-defined electrical current of 2 A was passed through the samples. The specific resistivities were subsequently calculated from the measured resistivities and the sample dimensions. The measurement devices were provided by the Faculty of Mathematics and Physics at the Charles University in Prague. From the past investigation, the accuracy of the measurement is about 0,05% [88].

As mentioned in chapter 2.1.2, the electrical resistivity of metals is temperature-dependent. The temperature has to be kept constant for all measurements. At the same time, the change in electrical resistivity due to phase transformations can be clearly distinguished at a low temperature. In order to achieve these two conditions, the electrical resistivities were measured in liquid nitrogen (-196°C).

4.6 Potentiostatic electrochemical measurement

The potentiostatic polarisations were performed in a 0,1 M NaCl aqueous solution at 30°C. As mentioned in chapter 1, the application field of aluminium-manganese alloys is dedicated to wrought alloys. For this reason, only sample 2 and 3 were subjected to the potentiostatic polarisation.

The samples were immersed in the electrolyte for 30 minutes to monitor the open-circuit potential (OCP). They were cathodically polarised about 500 mV away from OCP towards the anodic area. The average scan rate of 10 mV/s was implemented with the help of a computer. The polarisation consisted of the potential step 2,5 mV and the waiting time of 15 s before sampling.

The samples were polarised until the vertex current density of 0,1 mA/cm^2. After that, the samples were reversely scanned in the same manner until the polarisation went into the cathodic area again.

The collected data were smoothed using moving average. Subsequently, they were plotted on a logarithmic as well as a linear scale for the evaluation. The Tafel lines were drawn manually by the guideline mentioned in chapter 2.1.3.2 to determine the corrosion potential E_{Corr} and the corrosion current density j_{Corr}, see **Figure 6**.

The breakthrough potential E_b was obtained from the transition point between the passive and transpassive state, see **Figure 7**. The potential at the vertex current density was regarded as the pitting potential E_{pit}, and the corrosion potentials from the reverse scan was taken as the repassivation potential E_{rp}, see **Figure 8**.

According to the international standards, the uncertainty of this test method is not specified, and the reproducibility should be developed by the interlaboratory testing [28,89]. Because of the contamination in sample 3, only the measurement of sample 2 stage 1 will be repeated 5 times to demonstrate the reliability of the test. The standard deviations of the corrosion characteristics are shown in **Table 12**.

	j_{Corr} in µA/cm^2	E_{Corr} in mV	E_b in mV	E_{pit} in mV	E_{rp} in mV
	0,27	-890	-575	-554	-1007
	0,35	-876	-562	-542	-1010
	0,33	-920	-585	-559	-969
	0,36	-940	-594	-564	-978
	0,33	-891	-588	-571	-985
SD	0,04	26	13	11	18

Table 12 Statistical reproducibility of the potentiostatic electrochemical measurement conducted on sample 2 stage 1

5. Results

The results will be outlined by the investigation methods mentioned in the previous chapter. The microstructural changes of the samples will be illustrated with the help of the light microscope, scanning electron microscope (SEM) and transmission electron microscopy (TEM). The developments of hardness, resistivity and corrosion characteristics are subjected to comparison with other samples during the heat treatment as a preparation for the discussion in the next chapter.

However, the corrosion characteristics were, in fact, the evaluations of the polarisation curves plotted from the potentiostatic electrochemical measurements. Without the polarisation curves themselves, the corrosion behaviour of the samples during the heat treatment will not be shown. For this reason, the progression of the polarisation values will be additionally pointed out for each sample.

5.1 Microstructure

The main interest of this chapter is the microstructural change induced by the heat treatment. First the microstructure at stage 1 will be described. After that, the change will be elaborated.

5.1.1 Sample 1

The microstructure of sample 1 is globular with an average grain size of about 100 µm, see **Figure 45**. A small amount of Al_6Mn can be found at the grain boundaries as eutectic structure, see **Figure 46**. The observation with TEM also confirms the presence of $Al_3(Sc,Zr)$ precipitates with the $L1_2$ structure at stage 1, see **Figure 47**.

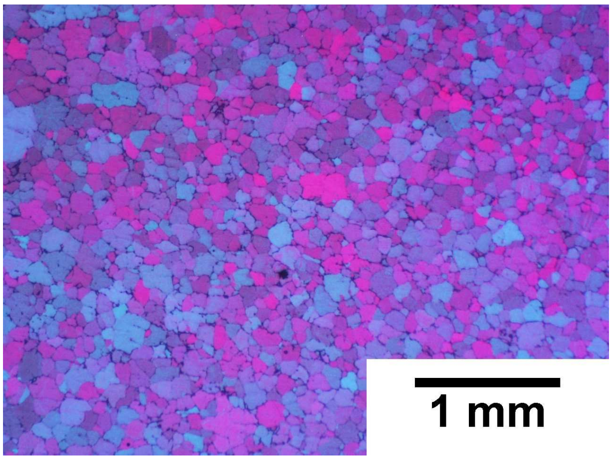

Figure 45 Light microscope image of globular grains in sample 1 stage 1

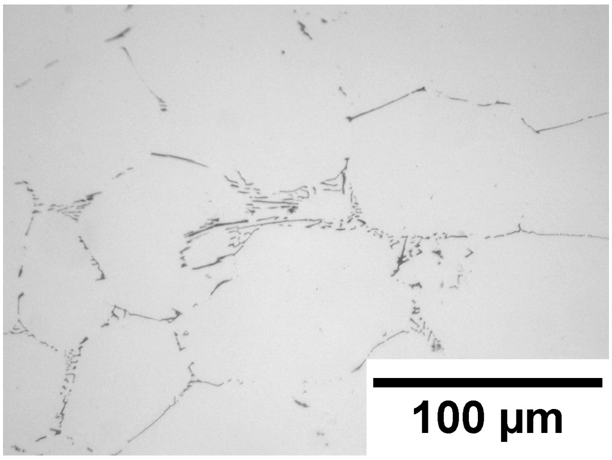

Figure 46 Light microscope image of Al_6Mn precipitates at the grain boundary in sample 1 stage 1

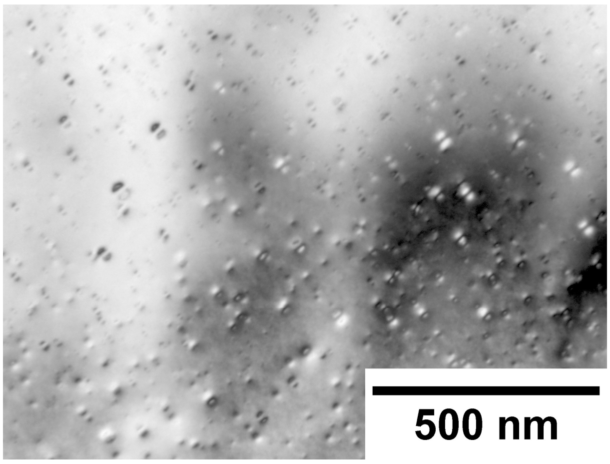

Figure 47 TEM image of $Al_3(Sc,Zr)$ precipitates inside a grain in sample 1 stage 1

At stage 6, fine precipitates are formed near the grain boundary. The number of precipitates is increased after prolonged annealing at 600°C (stage 7 and 8). They are identified as needle-shaped precipitates of Al_6Mn with the size of about 2 µm, see **Figure 48** and **Figure 49**.

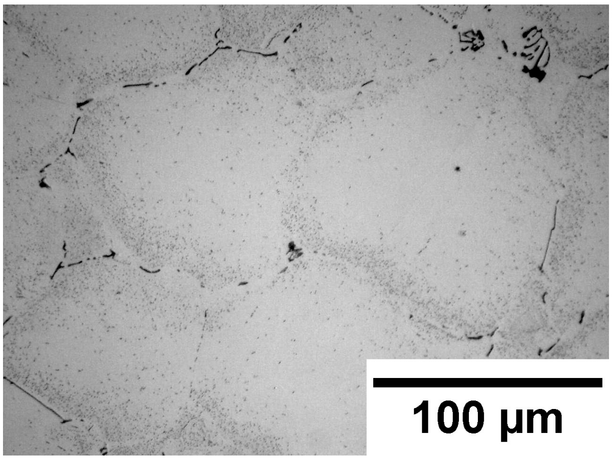

Figure 48 Light microscope image of small Al_6Mn precipitates (dots) near grain boundary in sample 1 stage 8

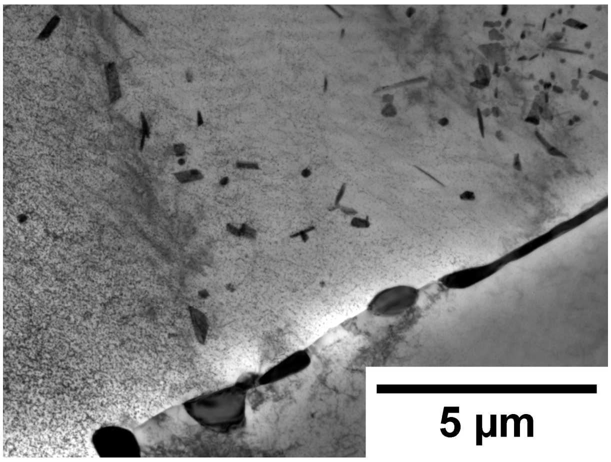

Figure 49 TEM image of needle-shaped Al_6Mn precipitates in sample 1 stage 8

5.1.2 Sample 2

Sample 2 shows a typical fibrous microstructure resulting from the extrusion. The thickness of the filaments is about 20 µm, see **Figure 50**. Inside these filaments, the subgrains of about 1 µm diameter can be observed by TEM and EBSD images, see **Figure 51** and **Figure 52**. The precipitates of $Al_3(Sc,Zr)$ are distributed within the subgrains, see **Figure 53**.

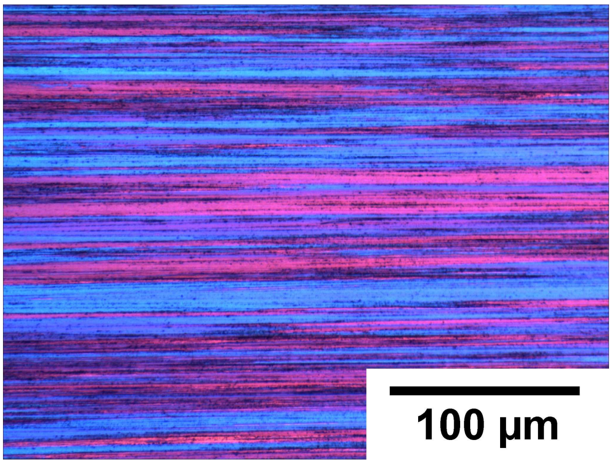

Figure 50 Light microscope image of sample 2 stage 1

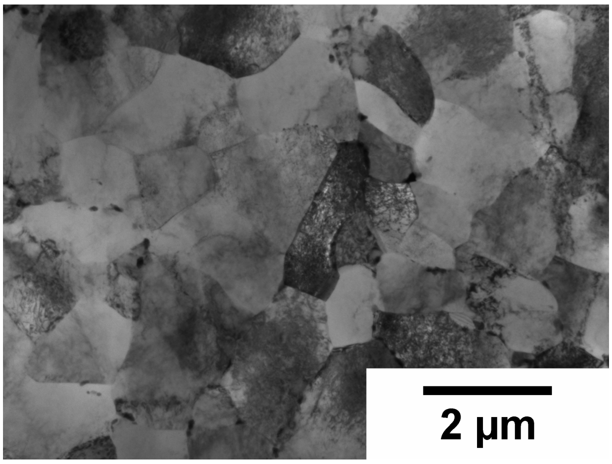

Figure 51 TEM image of subgrains in the cross section of sample 2 stage 1

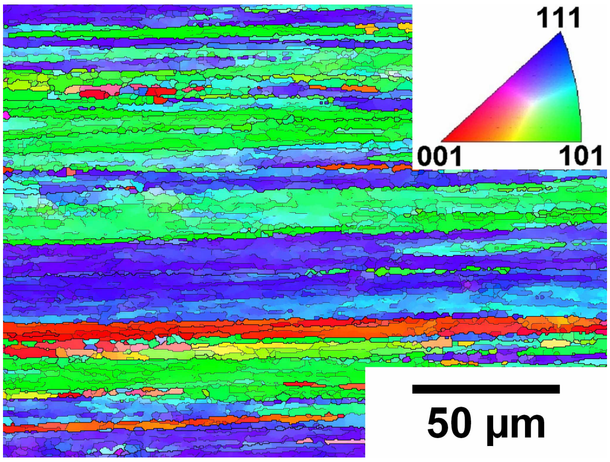

Figure 52 EBSD image of sample 2 stage 1

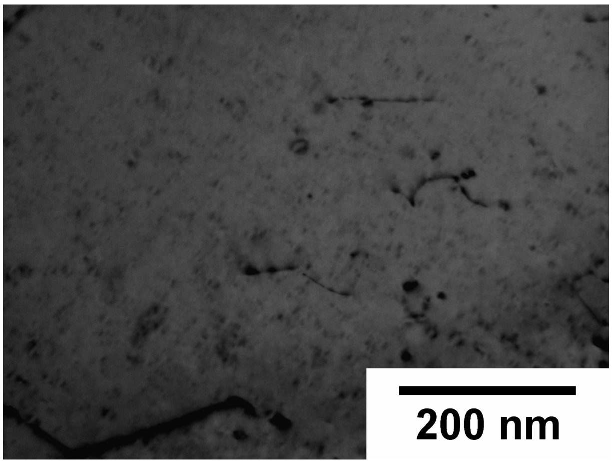

Figure 53 TEM image of $Al_3(Sc,Zr)$ precipitates inside the subgrains of sample 2 stage 1

As sample 2 was extruded from sample 1, it is no surprise that the Al_6Mn precipitates are also found here. However, the fine needle-shaped Al_6Mn precipitates are less likely to have been formed during the heat treatment. In **Figure 54**, Al_6Mn precipitates on the elongated grain boundary are clearly visible after annealing at 600°C. The microstructure of sample 2 remains unchanged throughout the heat treatment, and no recrystallisation is observed after the heat treatment at stage 8, see **Figure 55**.

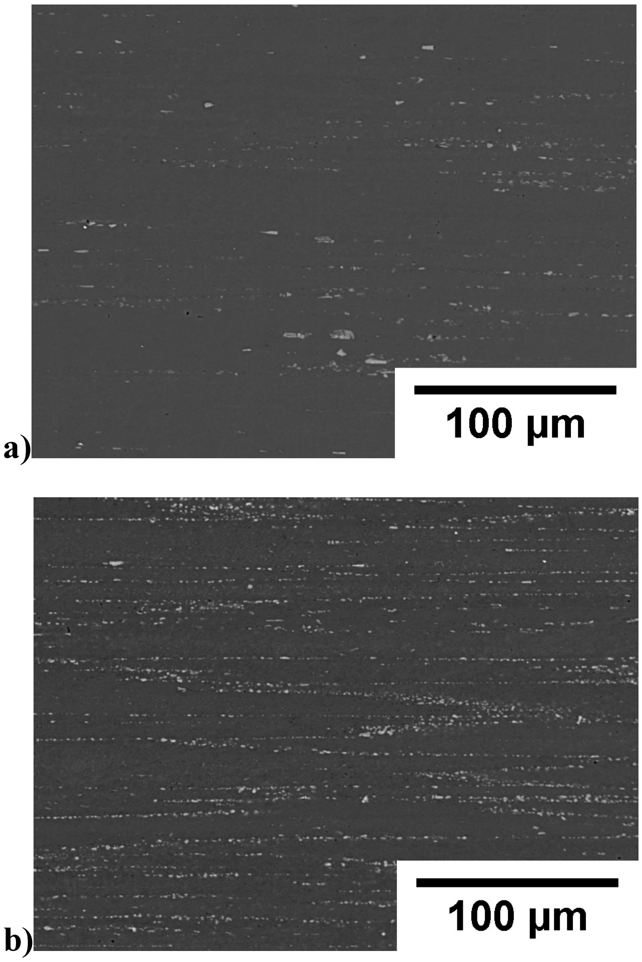

Figure 54 SEM images comparing the amount of Al_6Mn precipitates in sample 2 **a)** stage 1 and **b)** stage 6

After annealing at 600°C for 48 hours, the recrystallisation could be detected on the outside of sample 2. The recrystallisation shell has a thickness of 50 µm, see **Figure 56**. In the middle of sample 2, the recrystallisation was hardly noticeable.

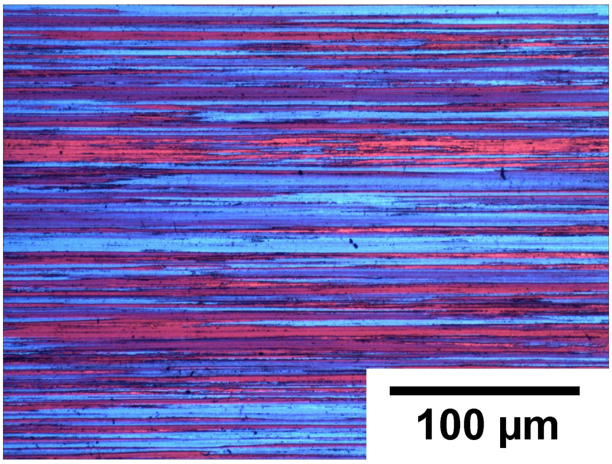

Figure 55 Light microscope image of sample 2 stage 8

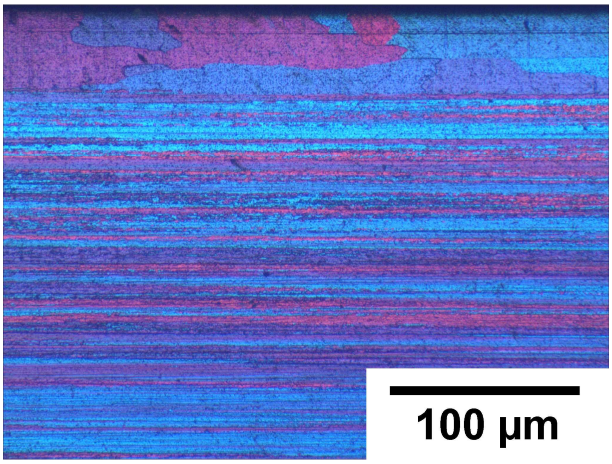

Figure 56 Light microscope image of recrystallisation in the outside of sample 2 after annealing at 600°C for 48 hours

5.1.3 Sample 3

The atomised powder displays globular grains of about 10 µm, see **Figure 57**. The size of the powder is between 20 to 100 µm, and the average diameter is 50 µm. The XRD result shows only the aluminium present in the powder, see **Figure 58a**.

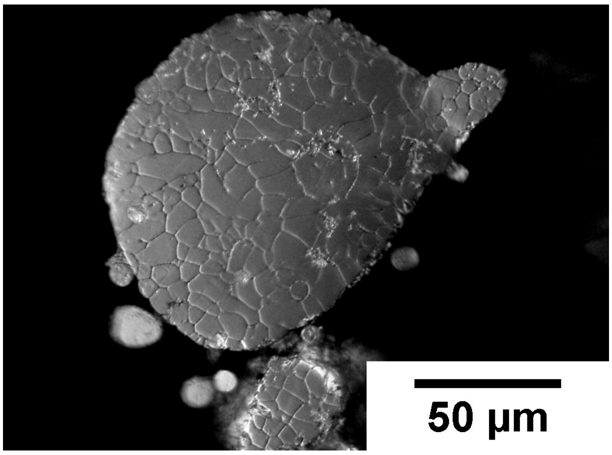

Figure 57 Light microscope image of powder cross section after atomising

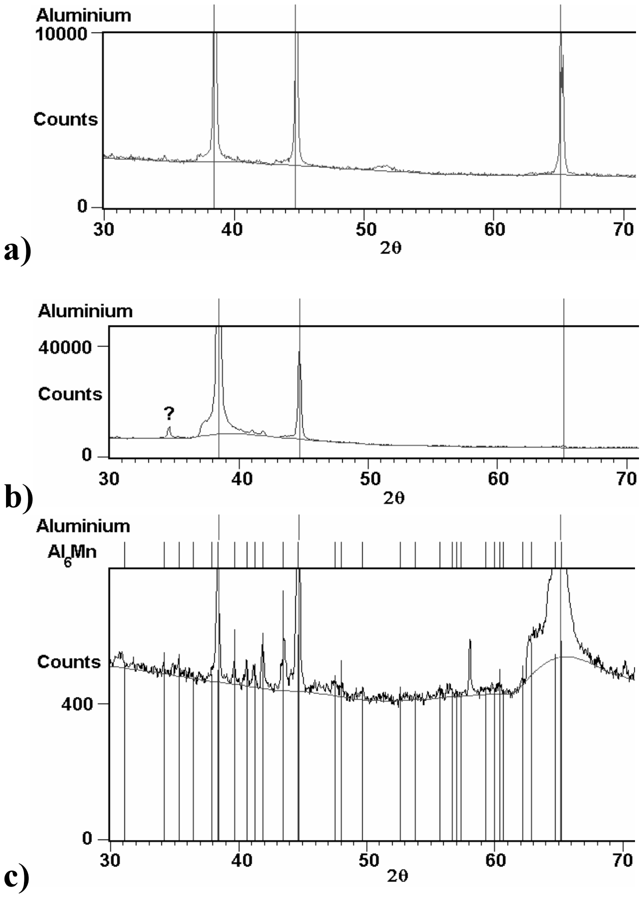

Figure 58 XRD spectrum of sample 3 **a)** powder, **b)** stage 1 and **c)** stage 8

On the XRD spectrum, an unidentified phase can be detected at position 34,6095°2θ after the extrusion. This phase is not in the database of the International Center for Diffraction Data (ICDD). The corresponding peak is marked with '?', see **Figure 58b**.

The very first difference between sample 2 and 3 is the surface quality. The surface of sample 3 is distinguishable by the surface tearing, which is clearly visible without any further preparation, see **Figure 59**.

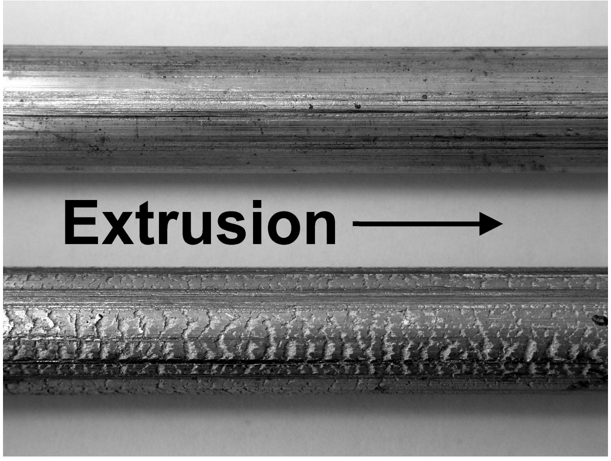

Figure 59 Different surface quality of sample 2 (top) and 3 (bottom)

The microstructure of sample 3 after the extrusion is shown in **Figure 60**. The EBSD image illustrates the subgrains within the filaments. The thickness of the subgrains is 2-3 µm, which is about the thickness of the filaments themselves, see **Figure 61**. The $Al_3(Sc,Zr)$ precipitates are also found inside the subgrains, see **Figure 62**.

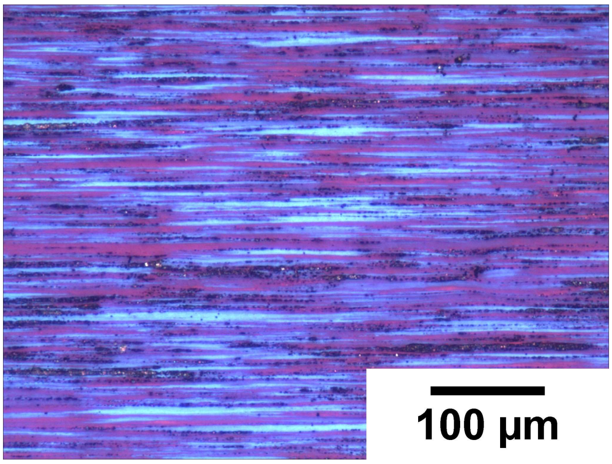

Figure 60 Light microscope image of sample 3 stage 1

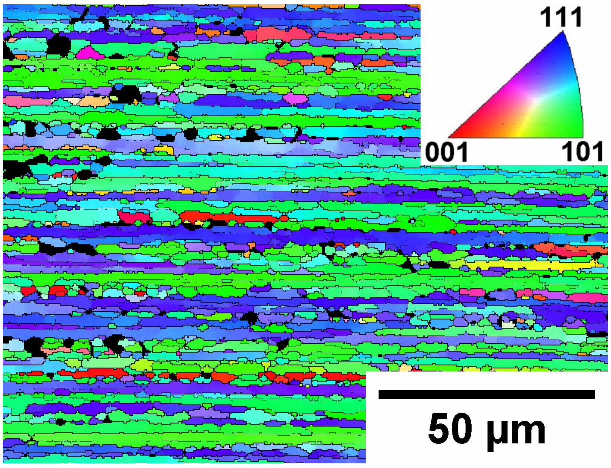

Figure 61 EBSD image of sample 3 stage 1

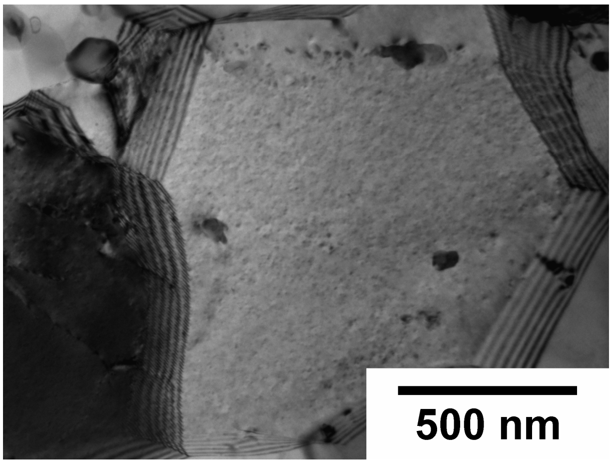

Figure 62 TEM image of a subgrain containing $Al_3(Sc,Zr)$ precipitates

Contamination in sample 3 was observed by an early reaction from the etchants, see **Figure 63**. High concentrations of antimony, tin and oxygen were verified in this area, see **Figure 64** and **Table 1**. The contaminations consist of tin-rich particles and antimony/tin oxides border. The evolution of this structure will be elaborated in chapter 6.3.1.2.

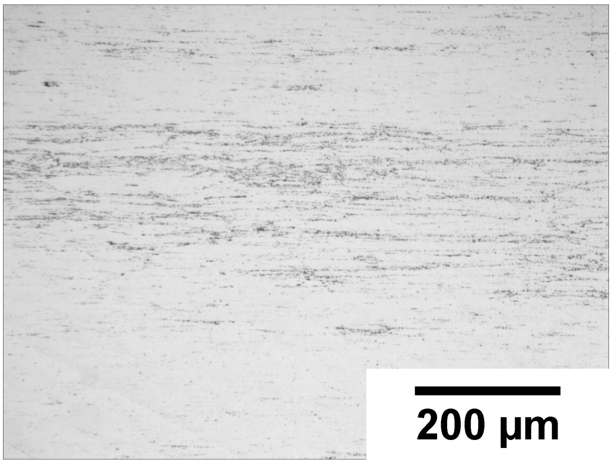

Figure 63 Light microscope image of an uneven chemical attack on the surface of sample 3 stage 1

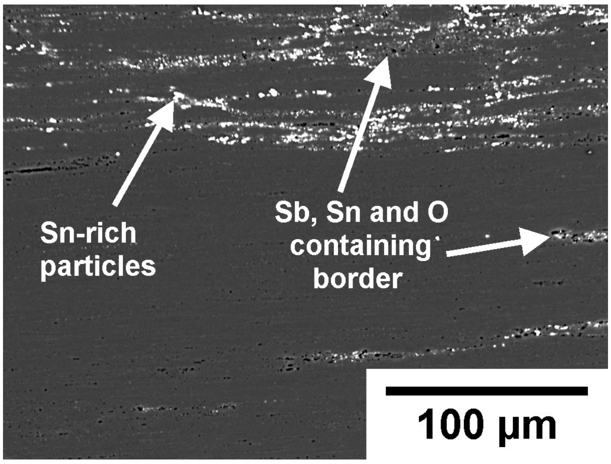

Figure 64 SEM image of contaminated area in sample 3 stage 1

Analysis point	**Composition in wt%**					
	Al	**Mn**	**Fe**	**Sb**	**Sn**	**O**
Sn-rich particle	91,83	1,63	0,43	0,00	4,77	1,34
Particle border	34,14	0,58	0,36	37,75	12,56	14,61
Matrix	95,71	1,41	0,35	0,64	0,21	1,68

Table 13 EDX analysis of contaminated area in sample 3 stage 1

The distribution of the contamination has been effected by the heat treatment. In **Figure 65**, it is obvious that the contamination has dispersed at stage 5 and does not form clusters anymore in comparison to stage 1.

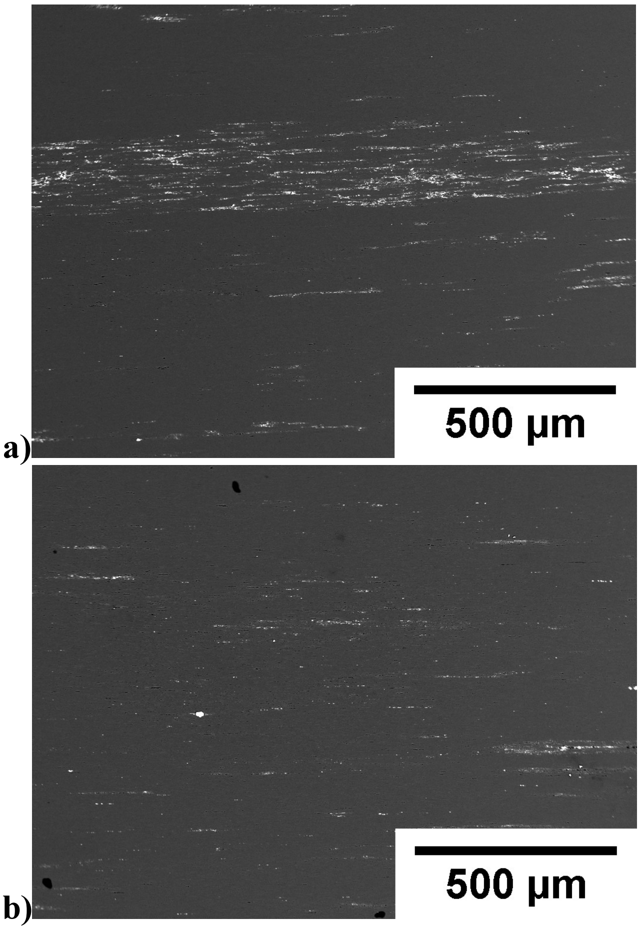

Figure 65 SEM images comparing the distribution of contaminated area in sample 3 **a)** stage 1 and **b)** stage 5

As already displayed in **Figure 58c**, Al_6Mn are formed during the heat treatment. The precipitates are located at the grain boundaries, see **Figure 66**. At the end of the experiment, no recrystallisation could be observed in sample 3. Even after 48 hours of annealing at 600°C, a recrystallisation is not detected, see **Figure 68**.

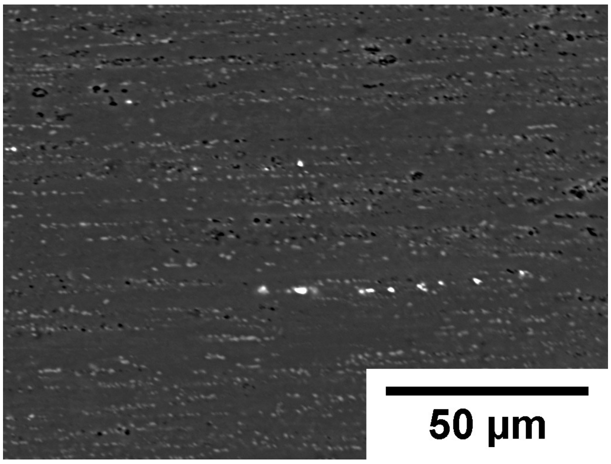

Figure 66 SEM image showing Al_6Mn (light grey) at the elongated grain boundary of sample 3 stage 6

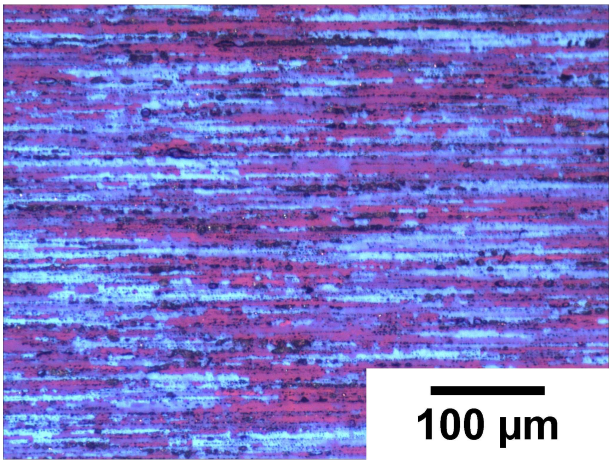

Figure 67 Light microscope image of sample 3 stage 8

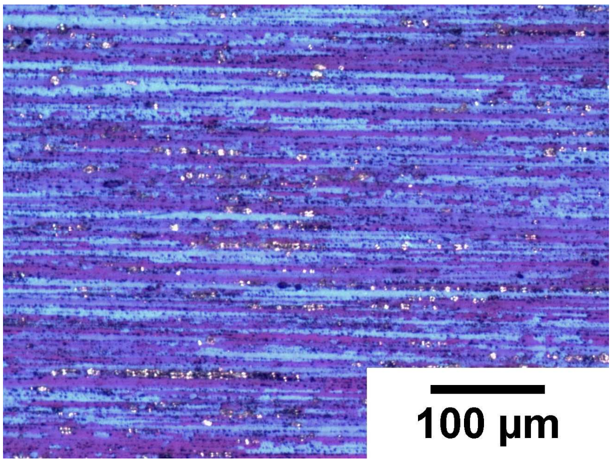

Figure 68 Light microscope image of sample 3 after annealing at 600°C for 48 hours

5.2 Hardness

The hardness development of three samples is roughly distinguished between cast (sample 1) and extruded (samples 2 and 3) samples. The progression of Vickers hardness (HV5) versus the course of step annealing is shown in **Figure 69**.

The hardness of sample 1 displays four regions of precipitation hardening. (1) The change was insignificant from stage 1 to stage 3, in which the hardness is about 52 HV5 (under ageing). (2) The hardness increase was detected at stage 4 (age hardening). (3) The maximum hardness of 77 HV5 was obtained at stage 5 (peak ageing). The hardness remains almost constant for one step. (4) After that, the hardness was gradually decreased from stage 6 onwards (over ageing).

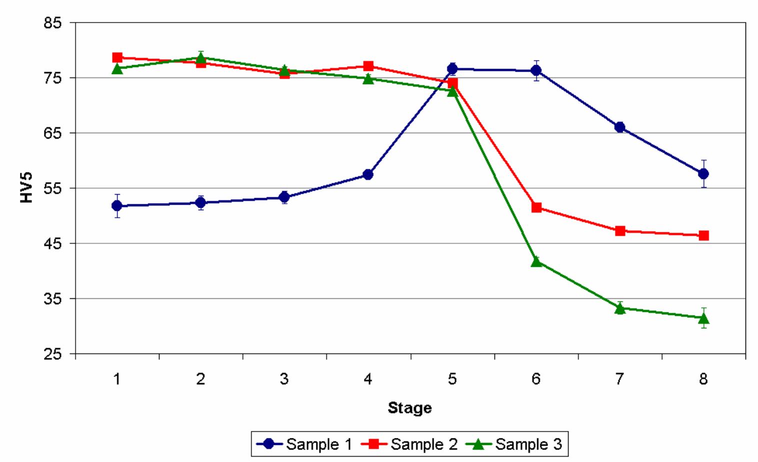

Figure 69 Hardness development during step annealing, see **Table 11** for the temperatures and durations

In the case of samples 2 and 3, the hardness changes between the stages 1 and 3 were also insignificant, like sample 1. The initial hardnesses were comparable to the hardness of sample 1 at stage 5. The average hardnesses from stage 1 to 3 were 77 HV5 in both samples.

From stage 4, their hardnesses were decreased slightly, and dropped dramatically at stage 6. Interestingly, the hardness values of samples 2 and 3 diverged from each other from stage 6. At the end of the experiment, the hardnesses of sample 1, 2 and 3 were 58, 46 and 32 HV5 respectively.

It should be noted that due to the large indentation area from the applied load of HV5, the hardness at the contaminated area is negligible. The measurements with the lowest load available showed a slightly noticeable hardness difference of 3-6 HV0,2.

5.3 Resistivity

From the results of resistivity measurements, we are able to observe the same tendencies, which come from the influence of the heat treatment. The specific resistivities of three samples during the heat treatment are plotted in **Figure 70**.

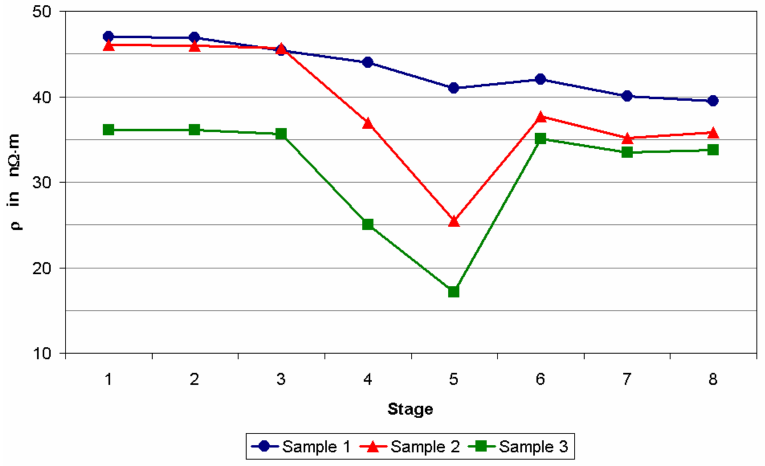

Figure 70 Specific resistivity development at -196°C (77 K) during step annealing

At stage 1 and 2, the specific resistivity of sample 2 was only about 1 nΩ·m less than that of sample 1 despite the huge hardness difference, which implied the effect of the precipitation hardening in sample 2.

The values of sample 3, on the other hand, were clearly below the others until stage 5. The offset between the specific resistivity of samples 2 and 3 was about 10 nΩ·m in this region. The difference started to narrow down after being annealed at 500°C (stage 5).

At stage 6, in which the values were rebounded in all samples, the specific resistivity of sample 3 was almost the same as at the beginning. In contrast, the specific resistivity of sample 2 from stage 6 until the end was around 10 nΩ·m lower than that of the starting value, which was rather strange considering the same precipitation process. The meaning of these offsets in different samples will be detailed again in the discussion section (chapter 6.3).

5.4 Corrosion behaviour

All five corrosion characteristics in this work will be presented by the polarisation order, namely the corrosion current density j_{Corr}, corrosion potential E_{Corr}, breakthrough potential E_{b}, pitting potential E_{pit} and repassivation potential E_{rp}.

The first chapter will be the comparison between the evaluated values, while the rest of this section will introduce the change of the polarisation curves themselves, especially the anodic current density parts in samples 2 and 3.

5.4.1 Corrosion characteristics

The first two corrosion characteristics we encountered during the polarisation are the corrosion current density and the corrosion potential. From the corrosion current density, sample 3 shows a higher corrosion rate from the beginning until the end of the experiment, see **Figure 71**. However, it is worth noting that the data scattering can be clearly seen at stage 2, 4 and 5.

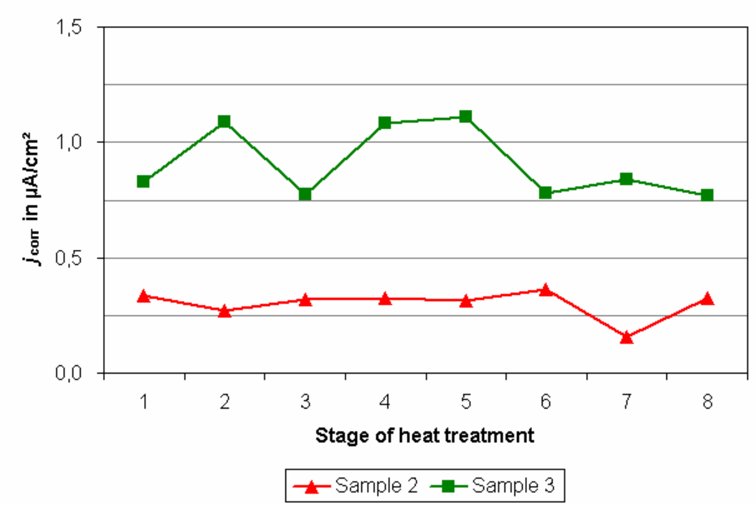

Figure 71 Corrosion current densities of sample 2 and 3 in 0,1 M NaCl solution during step annealing

The average corrosion potentials of samples 2 and 3 are about -900 mV and -1200 mV respectively, see **Figure 72**. It is the indication of the higher corrosion susceptibility in sample 3, which is also in agreement with the corrosion current density results mentioned above.

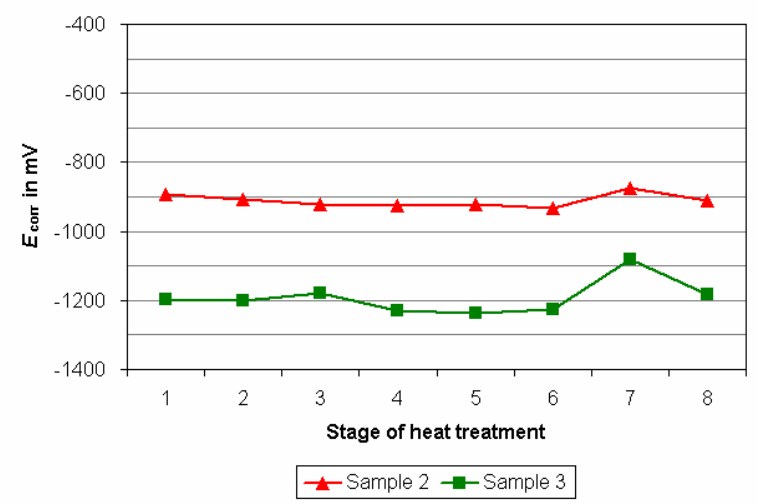

Figure 72 Corrosion potentials of sample 2 and 3 in 0,1 M NaCl solution during step annealing

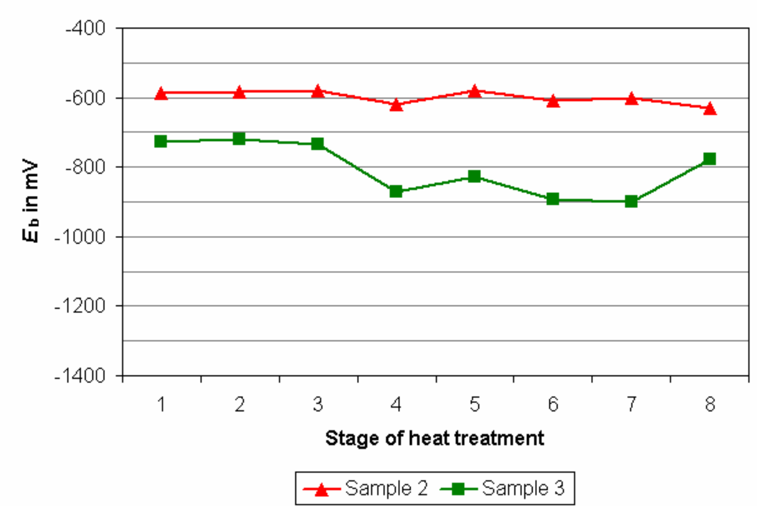

Figure 73 Breakthrough potentials of sample 2 and 3 in 0,1 M NaCl solution during step annealing

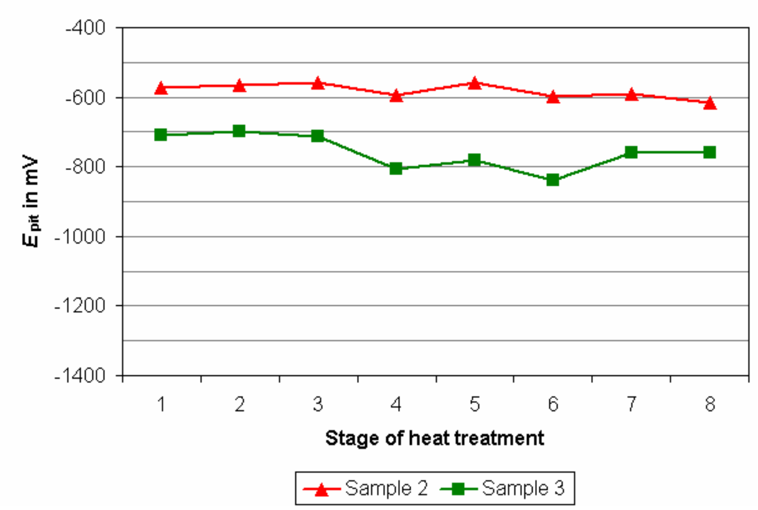

Figure 74 Potting potentials of sample 2 and 3 in 0,1 M NaCl solution during step annealing

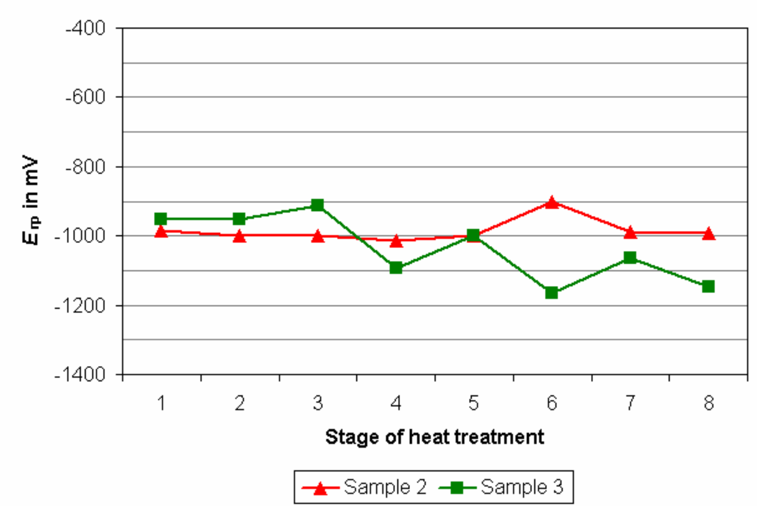

Figure 75 Repassivation potentials of sample 2 and 3 in 0,1 M NaCl solution during step annealing

Throughout the experimentation, we are able to observe the influence of the heat treatment only in sample 3. From stage 4 onwards, the potential drops from the initial values can be found for the breakdown, pitting and the repassivation potentials, see **Figure 73-76**. In sample 2, these characteristics can be regarded as unchanged, namely E_b -600 mV, E_{pit} -580 mV and E_{rp} -1000 mV.

It is interesting to consider the difference between E_{Corr} and E_{rp}. Sample 2 repassivates -100 mV from E_{Corr}. This negative potential shift confirms the damage of the passive layer, which has to be healed by the repassivation. Sample 3, on the other hand, has a positive potential shift despite its higher corrosion susceptibility. To be able to explain this contradiction, we have to detect the difference between the corrosion of these samples by analysing the polarisation curves first.

5.4.2 Polarisation curves of sample 2

Up to this point, the heat treatment seems to have no effect on sample 2, but in this chapter, the change induced by the heat treatment will be pointed out on the polarisation curves.

Although all corrosion characteristics do not show any significant changes, the repassivation capabilities are displayed by the hysteresis loops formed during the reverse scans. The polarisation curves of sample 2 are illustrated in **Figure 76**. The hysteresis loops have a similar shape from stage 1 up to stage 5. After sample 2 was annealed at 600°C (stage 6), the size of the hysteresis loop shrank dramatically and stayed in such a narrow form until the end of the experiment.

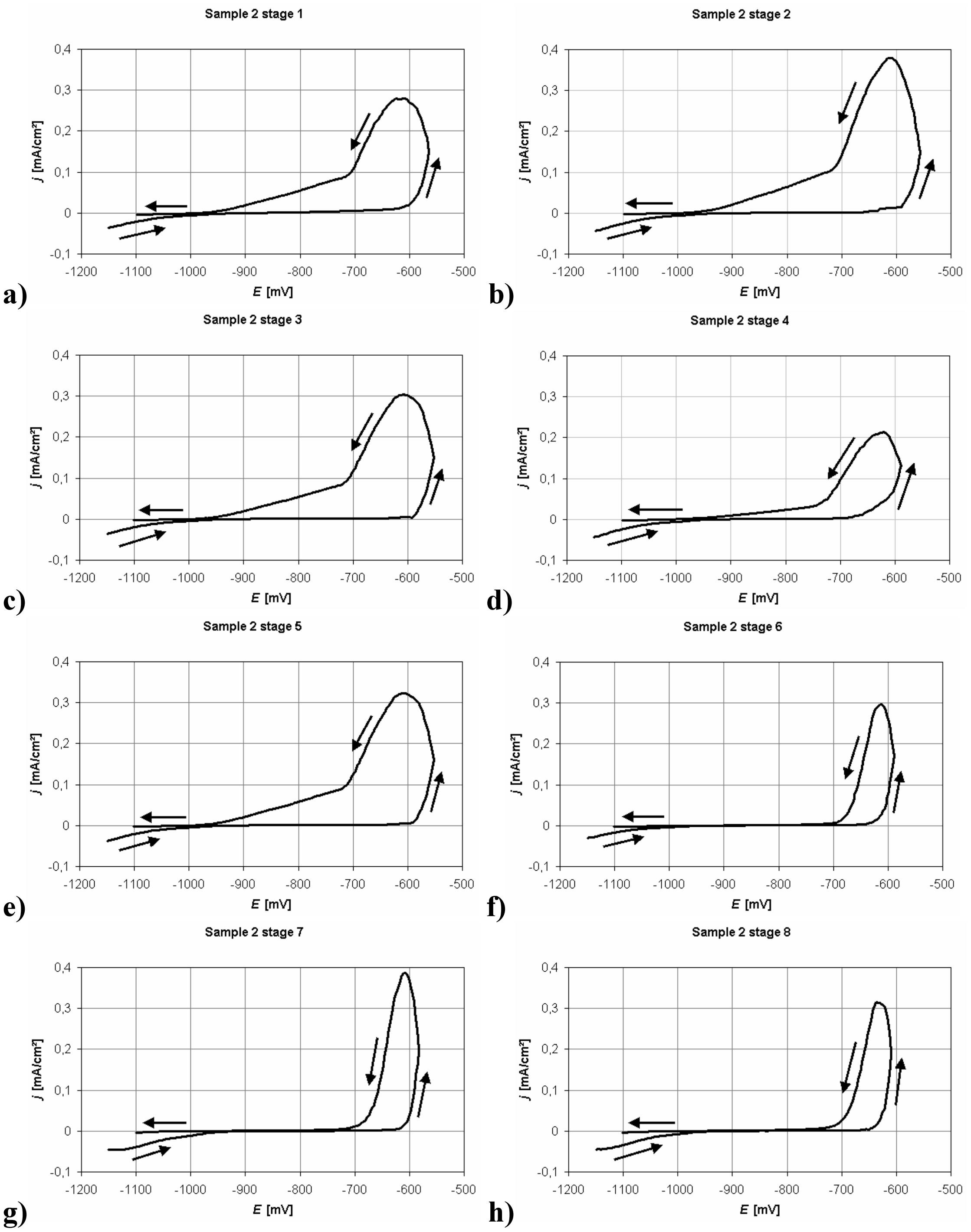

Figure 76 Polarisation curves of sample 2 in 0,1 M NaCl solution **a)** stage 1 **b)** stage 2 **c)** stage 3 **d)** stage 4 **e)** stage 5 **f)** stage 6 **g)** stage 7 **h)** stage 8

As mentioned in chapter 2.1.3.3, the smaller hysteresis loop in **Figure 76f-h** suggests that the pits on the surface of sample 2 were healed faster after stage 6 than they were in the earlier stages.

With the logarithmic plot of the Tafel diagram, we are able to observe the progress of the polarisation near the corrosion potential. **Figure 77** shows the Tafel diagrams of sample 2. The narrower hysteresis loops can also be seen in these diagrams from stage 6 onwards.

The intersection of the hysteresis loop at stage 6 suggests that the surface became more protective during the reverse scan. However, this is the only stage, that displays such behaviour, as E_{rp} at stages 7 and 8 are behind E_{Corr} once again, see **Figure 77f**. This one-time observation will be discussed again in chapter 6.2.2.2.

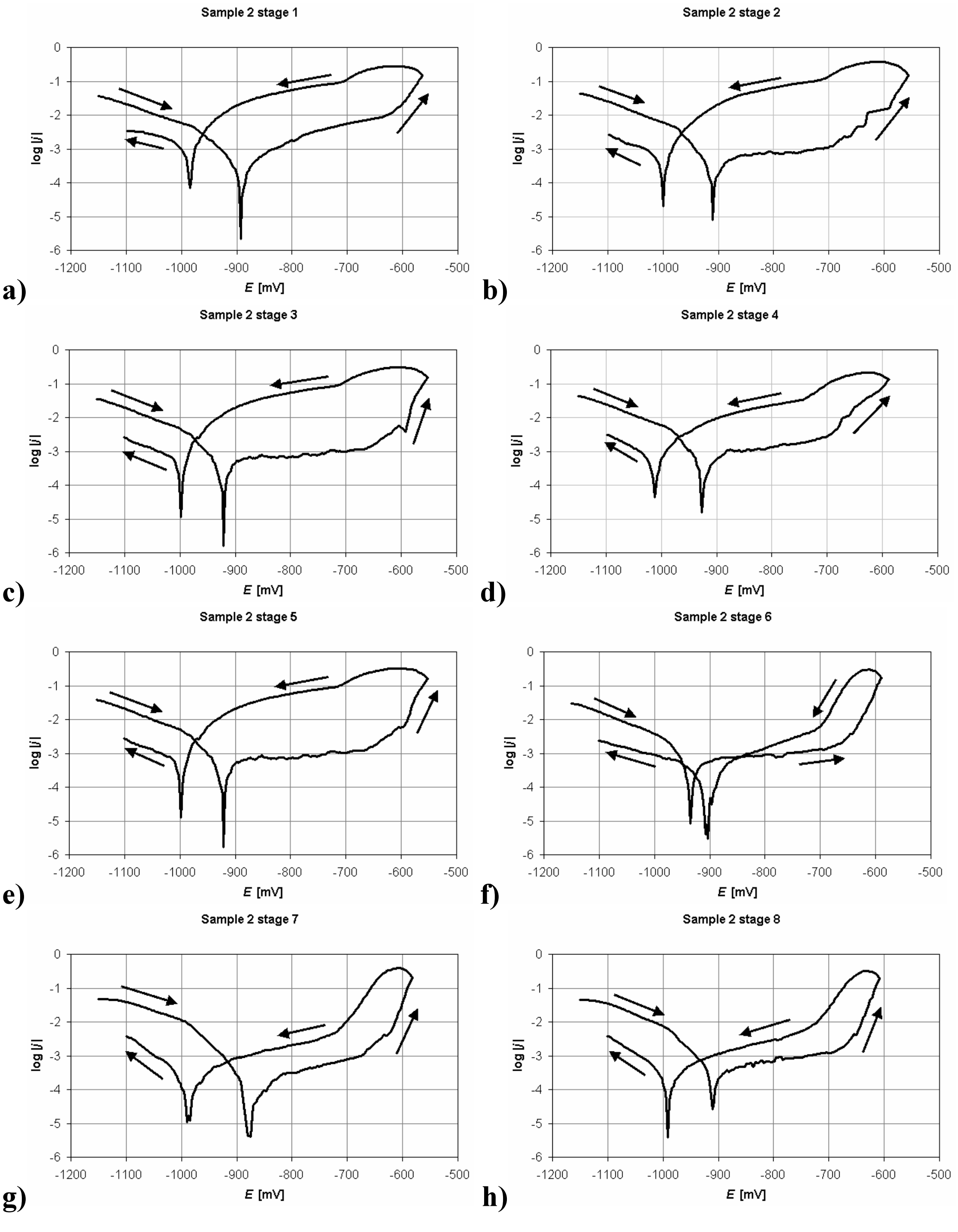

Figure 77 Tafel diagrams of sample 2 in 0,1 M NaCl solution **a)** stage 1 **b)** stage 2 **c)** stage 3 **d)** stage 4 **e)** stage 5 **f)** stage 6 **g)** stage 7 **h)** stage 8

5.4.3 Polarisation curves of sample 3

Aside from its lower corrosion resistance, the polarisation curves of sample 3 also show some considerable differences in the anodic area, which were constantly altered by the annealing. The cause of these changes will be discussed in chapter 6.3.2.2. As for this part, the corrosion behaviour of sample 3 will be underlined with the help of the polarisation curves.

Sample 3 shows the anodic current densities similar to the passivation process in the early stages, compare **Figure 78a-c** with **Figure 7**. Due to the very small passivation current densities j_p, it is simpler to observe the polarisation curves from the Tafel diagrams, see **Figure 79a-c**. In the Tafel diagrams, we are able to see the jagged lines on the curves, which began straight after the passivation of the surfaces. These jagged lines can be understood as the instability of the passivated surfaces.

At stages 4 and 5, j_p are clearly increased, which indicates some effects from the heat treatment, see **Figure 78d** and **e**. Despite this change, the passivation potentials E_p still remain unchanged at about -1100 mV.

At stage 4, the jagged lines from stages 1 to 3 are not visible anymore. But still, we are unable to say that the passive layer has become more stable because the passive anodic current densities j_{pass} have been gradually raised as shown in **Figure 79a-e**, implying more corrosion attack on the surface. The higher j_p and j_{pass} are followed by the narrower passive state approximately from -1030 to -870 mV in stage 4 in comparison to -950 to -850 mV in stage 5.

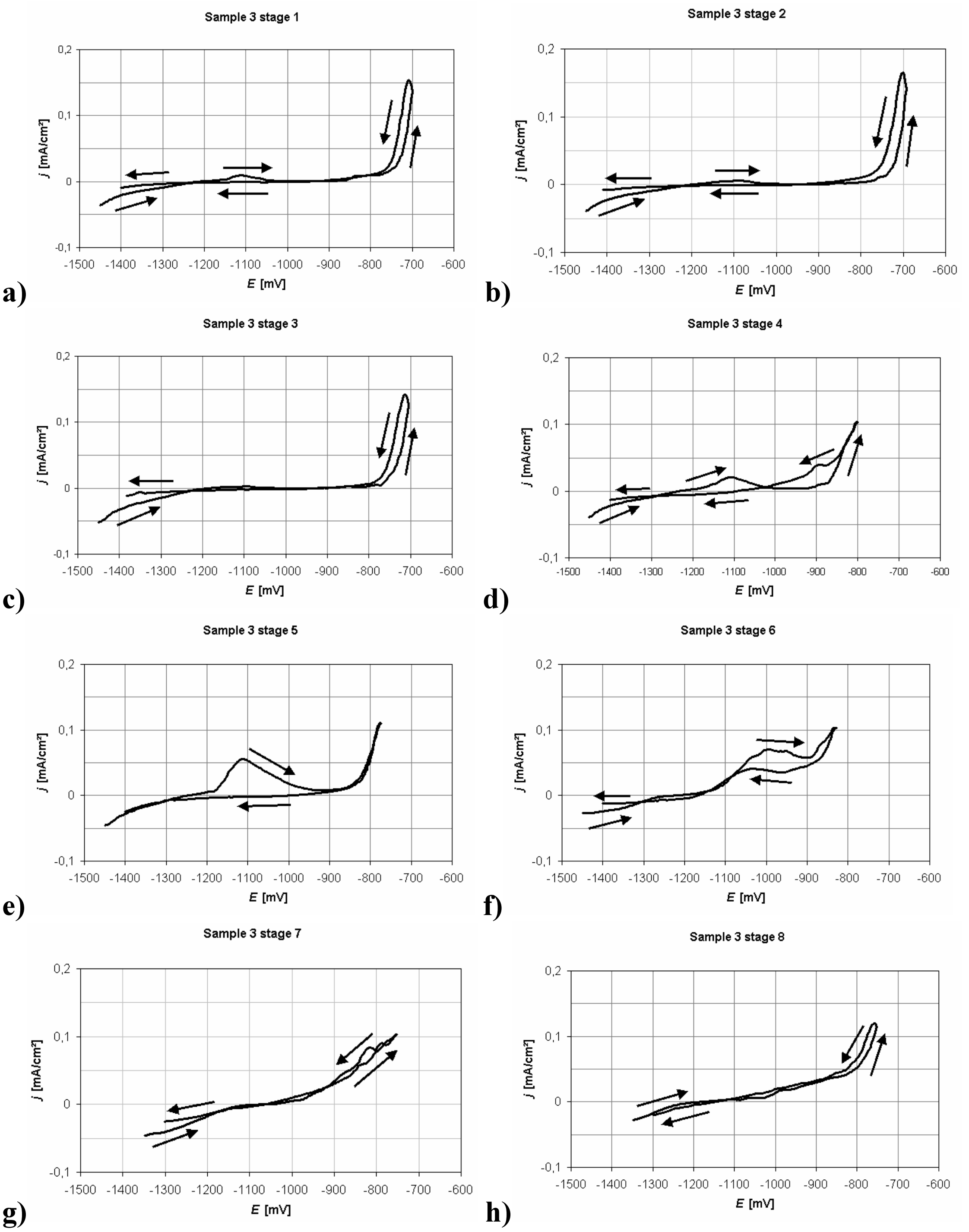

Figure 78 Polarisation curves of sample 3 in 0,1 M NaCl solution **a)** stage 1 **b)** stage 2 **c)** stage 3 **d)** stage 4 **e)** stage 5 **f)** stage 6 **g)** stage 7 **h)** stage 8

Although the corrosion characteristics and the corrosion behaviour indicate the greater corrosion susceptibility in sample 3, we have yet to find the reason for some irregularities of this sample such as the passivation process or the effect of the heat treatment on the passivation. The explanation is suggested by the reverse scan.

Throughout the experiment, the hysteresis loops formed during the reverse scan of sample 3 are even smaller than those of sample 2. The smaller loops are understood as less pitting corrosion, which is in contradiction with the main results from the corrosion characteristics themselves. Not to mention that at stage 6 and later, the sample can not be considered passive anymore, as the anodic current density continues to increase without forming a plateau near the x-axis, see **Figure 78f-h** and **Figure 79f-h**. The cause of this phenomenon will be enlightened upon in the discussion.

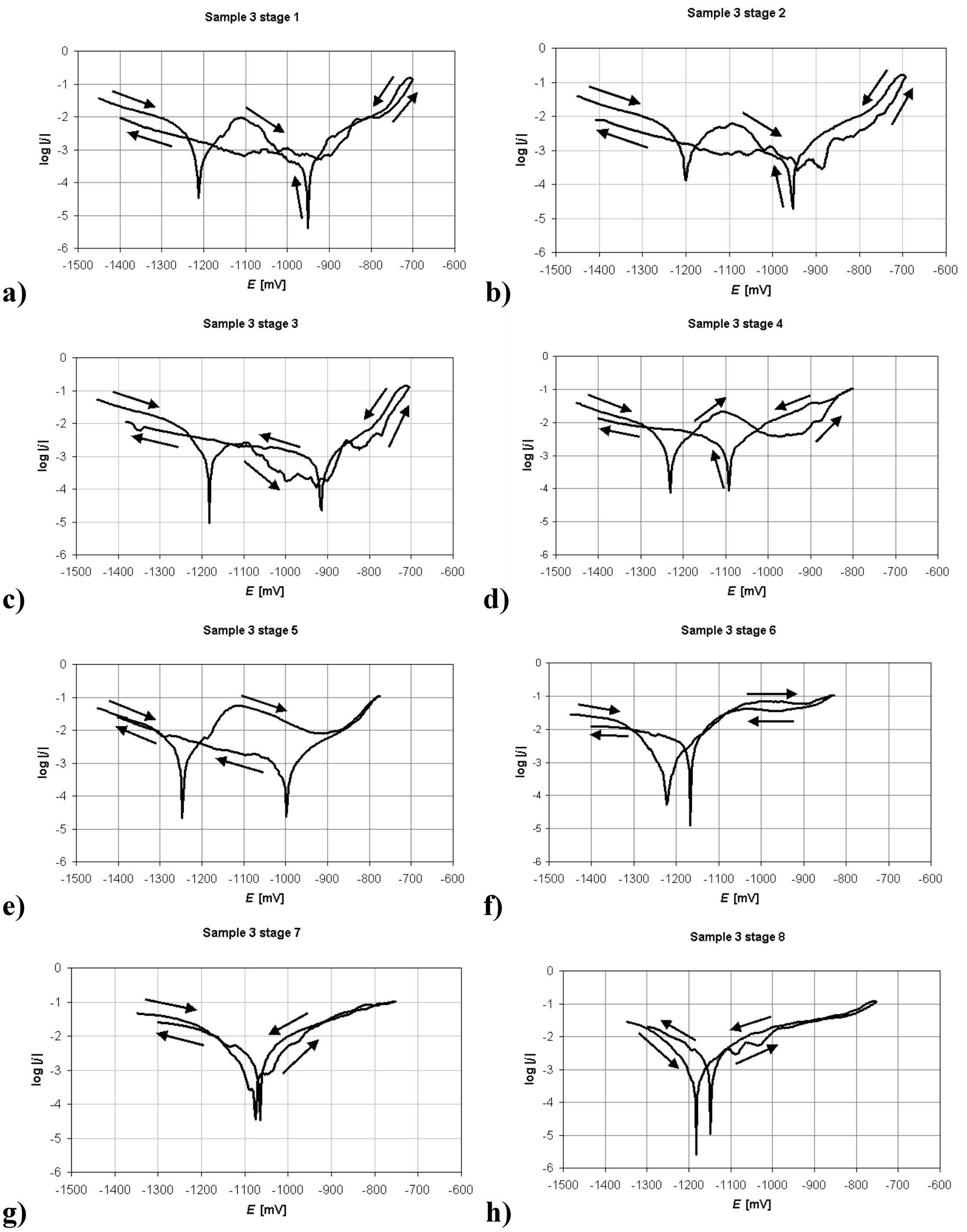

Figure 79 Tafel diagrams of sample 3 in 0,1 M NaCl solution **a)** stage 1 **b)** stage 2 **c)** stage 3 **d)** stage 4 **e)** stage 5 **f)** stage 6 **g)** stage 7 **h)** stage 8

6. Discussion

The main purpose of this work remains the investigation of the precipitation hardening in an Al-Mn alloy obtained by the scandium and zirconium addition. Meanwhile, the alloy has benefited from the nanoscale $Al_3(Sc,Zr)$ in regards to the recrystallisation resistance and the unaffected corrosion behaviour thanks to its small size.

In this chapter, the results from the previous chapter will be discussed for each sample. The hardness change will be compared alongside the specific resistivity to provide information about the phase transformations. The corrosion resistance is monitored by the corrosion characteristics.

While the hardness and the specific resistivity can be used to examine the effect of the production routes, the corrosion characteristics of the extruded samples can not be simply compared in such a way because of the interferences by the contaminations in sample 3. Instead, the development of the polarisation curves during the heat treatment will be discussed from the point of view of the microstructure.

6.1 Sample 1

6.1.1 Precipitation during under ageing condition

The hardness and the specific resistivity development of sample 1 are summarised in **Figure 80**. We are able to see from **Table 14**, that the starting hardness of sample 1 is comparable to that of the alloys without Sc and Zr. So, it is arguable that the presence of $Al_3(Sc,Zr)$ precipitates has not contributed to the hardness increase at stage 1 yet.

Even though the hardness at stage 3 does not show much difference from the first two stages, the specific resistivity drop implies the increased purity of the matrix by the precipitation as opposed to stage 2. If we consider that the effective diffusion of Sc is activated at a temperature above 250°C [13,39,74] and 350°C for Mn and Zr [12,58,90,91], the specific resistivity drop would not have been caused by the precipitation of Al_6Mn but rather by the additional Al_3Sc, which has not yet been precipitated during the cast process.

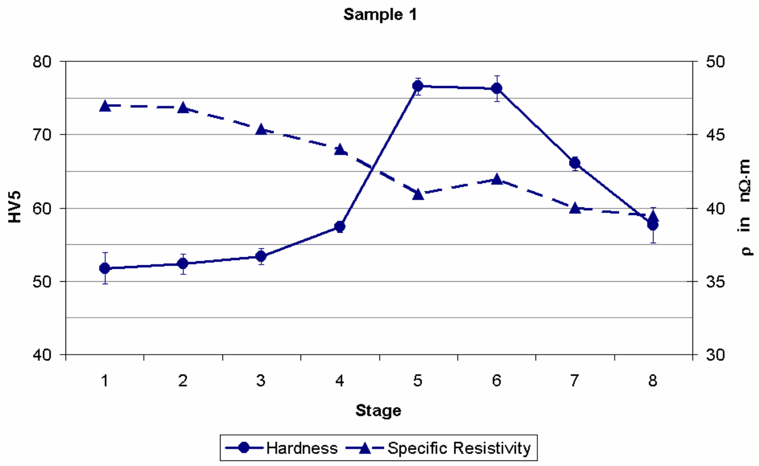

Figure 80 Hardness and specific resistivity development of sample 1 during step annealing

Composition in wt%					Measurement	Hardness	Reference
Mn	Sc	Zr	Fe	Si			
1,19	-	-	0,61	0,16	HV0,3	55	[55]
0,48	-	-	0,21	0,11	HV, the load not mentioned	56	[56]
0,74	-	-	0,21	0,17		61	
1,38	0,26	0,16	0,11	0,03	HV5	52	This work

Table 14 As cast hardness of the Al-Mn alloys without Sc and Zr in comparison to the hardness of sample 1 stage 1

6.1.2 Precipitation hardening

For the same reason mentioned above, we should take the precipitation of Al_6Mn into consideration from stage 4 onwards, although the precipitates may not be observable on the light microscope. However, as the general precipitation hardening effect of the Al-Mn alloys is negligible [59,78,92,93], it is safe to assume that the hardness increase at stage 4 is mainly the result from Al_3(Sc,Zr) either by the decomposition of the matrix or the coarsening of the existing precipitates. Either way, the radius of the Al_3(Sc,Zr) precipitates will increase to the optimum radius at stage 5.

6.1.3 Specific resistivity increase and subsequent hardness decline

An increasing annealing temperature has a beneficial effect on the diffusivity of the alloying elements and, subsequently, their decomposition as precipitates. Nevertheless, the solubilities of the alloying elements in the matrix also increase with the temperature. In this scenario, the existing precipitates will be partially dissolved into the matrix again, which is the reason for the slightly increasing specific resistivity at stage 6.

Not only the dissolution of the precipitates should be held responsible for the hardness drop because the specific resistivities continue to decrease in stages 7 and 8. The hardness drop is partly the result of the Ostwald ripening - the coarsening of the $Al_3(Sc,Zr)$ precipitates, while the increasing number and size of Al_6Mn in stages 7 and 8 signify more precipitation of this phase and the further decreasing specific resistivity.

6.2 Sample 2

6.2.1 Hardness and specific resistivity

6.2.1.1 Influence of the hot extrusion

As mentioned at the beginning of this work, the intermediate results obtained from sample 1 will be taken into consideration in samples 2 and 3. The difference in the starting condition between the cast (1) and the extruded samples (2 and 3) is caused by the production route. The pre-heating at 350°C before the extrusion is more than enough to induce the precipitation of $Al_3(Sc,Zr)$ or even Al_6Mn, see stage 3 in **Figure 80**. The unchanged specific resistivities from stages 1 to 3 are also the implication of the prior precipitation, see **Figure 81**.

From the maximum hardness of sample 1 (77 HV5), it is obvious that the hot extrusion does not yield any noticeable strain hardening effect in sample 2, whereas the hardness increase in cold-rolled Al-Mn alloy of the comparable engineering strain without any Sc and Zr addition can be as high as 17 HV0,3 [55]. In other words, the peak ageing condition is already attained even before the experimentation begins, and the hardness increase as a result of the hot extrusion is negligible.

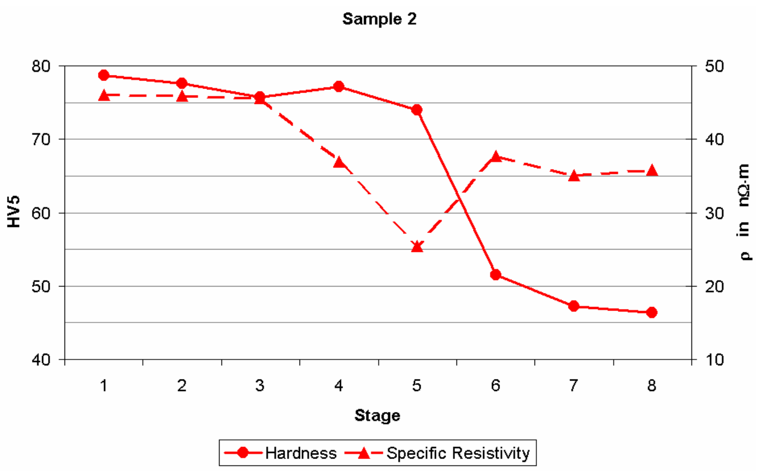

Figure 81 Hardness and specific resistivity development of sample 2 during step annealing

Still, the starting value of the specific resistivity is not added on to our explanation yet because as mentioned in chapter 5.3, the specific resistivity of sample 2 stage 1 is only 1 nΩ·m less than that of sample 1 regardless of the precipitation. According to the results from Knipling et al., the specific resistivity changes of about 5 and 7 nΩ·m are required to obtain the peak ageing condition in the aluminium alloys Al-0,12Sc-0,26Zr and Al-0,15Sc-0,31Zr respectively [12,13]. This argumentation should give us a fair reason to assume that the specific resistivity drop from the precipitates in sample 2 is compensated by the dislocation density induced by the extrusion.

6.2.1.2 Specific resistivity change in comparison to sample 1

When the dislocation comes into consideration, it is crucial to elaborate further the meaning of the specific resistivity drop at stage 4 and stage 5, as the dislocation reduction could deliver a significant change in specific resistivity. But if the reduction of the dislocations is the only significant factor here, we would not be able to observe the rebound at stage 6 at all. So, we can be sure, that at least this rebound of about 12 nΩ·m belongs to the dissolution of the prior precipitation.

The reason for more precipitation and a subsequently bigger rebound in sample 2 lies within the deformed microstructure. The positive effect of a deformation on the precipitation of Al_6Mn has been confirmed by the previous investigations [78,79,93,94]. From our observation in the previous chapter, the deformation would help shorten the diffusion distance of Mn atoms, and promote the precipitation of the Al_6Mn phase. Eventually, we are able to observe the Al_6Mn precipitates at the grain boundary more than inside the deformed grains in **Figure 54**.

6.2.1.3 Hardness drop

Up to this point, the hardness drop has been deemed as the coarsening of the $Al_3(Sc,Zr)$. Still, it is interesting to consider why the hardness has dropped sharply in sample 2, while sample 1 can maintain the hardness for 1 hour after annealing at 600°C before it declined slowly.

Even with their uniform distribution, the coarsening of the $Al_3(Sc,Zr)$ precipitates is also promoted by the deformation due to the improving diffusion along the elongated grain boundary. Further more, the pre-heating before the extrusion is undoubtedly counted towards the heat treatment. This basically means, the extruded samples are affected by the heat more than sample 1, which might accelerate the coarsening of the $Al_3(Sc,Zr)$ precipitates

6.2.1.4 Recrystallisation annealing

Nevertheless, considering how quick the Al-Mn alloy in **Figure 29** can be recrystallised at a temperature below 500°C, the $Al_3(Sc,Zr)$ precipitates should be able to suppress the recrystallisation even after the hardness drop. The recrystallisation, however, takes place near the surface, unlike the recrystallisation at high temperature in **Figure 29** probably because the $Al_3(Sc,Zr)$ precipitates are able to prevent the particle stimulated nucleation from the coarsening Al_6Mn precipitates above the critical size, see chapter 2.2.3. So, the recrystallisation has to start from the location with a higher dislocation density.

6.2.2 Corrosion behaviour

6.2.2.1 Corrosion characteristics

The corrosion characteristics from the other investigations are listed in **Table 15**. In order to compare the results, we will use the corrosion characteristics from this stage as the peak ageing condition of sample 2 is already represented at stage 1. The corrosion current density (j_{Corr}) shows that sample 2 has a slightly higher corrosion rate in 0,1 M NaCl solution than the high purity aluminium. Its more negative corrosion potential (E_{Corr}) also suggests less corrosion resistance in sample 2, which coincides with the claim made in chapter 3.1.

Alloys composition	**j_{Corr} in µA/cm^2**	**E_{Corr} in mV**	**E_b in mV**	**E_{pit} in mV**	**E_{rp} in mV**	**Reference**
High purity Al	0,253	-828	-	-615	-	[95]
Al-0,5Sc-0,4Zr	0,138	-754	-	-625	-	[95]
Al-1,38Mn-0,27Sc-0,19Zr	0,33	-891	-588	-571	-985	This work (sample 2 stage 1)

Table 15 Comparison of the corrosion characteristics of the aluminium alloys obtained from the polarisation in 0,1 M NaCl solutions

The excellent corrosion resistance of Al-0,5Sc-0,4Zr is partly based on the powder metallurgical preparation method, which enhances E_{Corr} even further. The manganese addition is responsible for a marginal improvement on E_{pit}. Unfortunately, it is not possible in this work to confirm the effect of the powder metallurgical preparation due to the contamination in sample 3.

6.2.2.2 Polarisation curves

Besides the corrosion characteristics, the main interest of this section is to explain the hysteresis loop, which has been drastically shrinking after the annealing at 600°C, but first, we should clarify some small details about the polarisation curve at stage 6. It is very unlikely for a metal to have an improved corrosion resistance only during the first hour of the annealing (stage 6) and then revert back to the similar corrosion characteristics as before. For this reason, the improved value of E_{rp} in **Figure 77f** should be regarded as an experimental error.

With reference to our test condition, the hysteresis loop is formed according to the pitting corrosion, which is repassivated during the reverse scan. The dissolution of the precipitates due to heat treatment has already been discussed in chapter 6.1.3, but we have yet to expand the scope to cover the effect of the alloying elements in the solid solution.

The Mn atoms in the solid solution are known to raise the corrosion potential of the aluminium matrix, see **Figure 22** and **Table 7**. As a result, the matrix will be more noble than the Al_6Mn precipitates, making them a target in the corrosion reaction. Thus, the Al_6Mn dissolution at stage 6 does not only help to increase the Mn in the solid solution, but indirectly reduces the potential corrosion sites. Ultimately, the improved corrosion resistance is reflected in the smaller hysteresis loops.

6.3 Sample 3

6.3.1 Hardness and specific resistivity

6.3.1.1 Influence of the powder metallurgical preparation

The fine globular grains within the powder are the product of the atomisation. The high cooling rate of this production route has suppressed the formation of the other phases. Even so, we can not exclude the existence of the $Al_3(Sc,Zr)$ precipitates in the powder due to their volume fraction and the size of the powder itself, which is confirmable neither by the X-ray diffraction (XRD) nor the hardness measurement.

Theoretically, we should be able to observe only the Al and Al_6Mn phases on the XRD spectrum. However, **Figure 58b** shows an unknown phase '?' after the extrusion. Considering its visible peak and the absence of the Al_6Mn phase, this unknown phase could have consisted of the contaminants, Al and Mn.

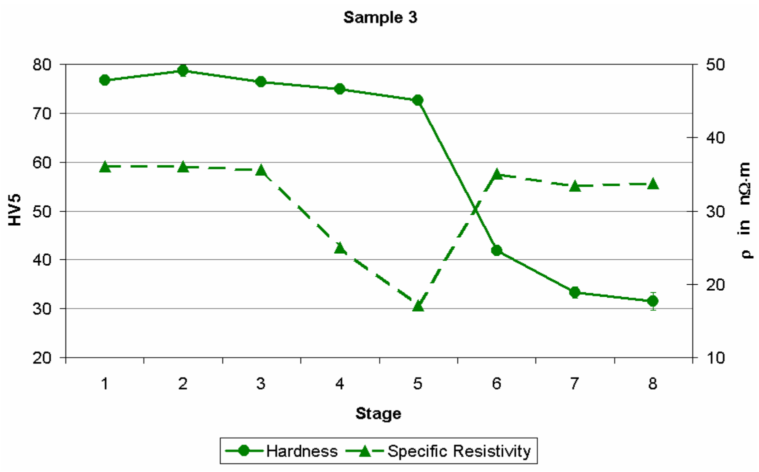

Figure 82 Hardness and specific resistivity development of sample 3 during step annealing

The hardness of sample 3 can be understood the same way as sample 2. The $Al_3(Sc,Zr)$ precipitates are responsible for the initial hardness. On the other hand, the specific resistivity offset of about 10 nΩ·m, observed up to stage 4, indicates a difference caused by the production routes.

From the aspect of the grain size, the crystallographic defects at the grain boundaries should hinder or scatter the flow of the electrons, and the specific resistivity of the sample should have increased [18,19]. The same tendency can be expected from the additional substitutional or interstitial atoms brought on by the contamination. Even if the low solubilities of Sb and Sn in Al are negligible, the specific resistivity would be unaffected by these elements.

The offset can be explained from an indirect effect from the powder material. The deformation behaviour of the loosely compacted powder cylinder is, by no means, identical to a solid material. While the deformation of the cast alloy is ruled by the material flow, the powder is able to squeeze itself through the opening.

Hence, the dislocation density is lower in sample 3, and the specific resistivity is not compensated as it was in sample 2. Unfortunately, the comparison of the microstructure before and after the deformation is not a suitable demonstration for this statement due to a very high reduction ratio (reduction in area) about 95% by the extrusion.

The lower dislocation density might be the possible explanation for the non-recrystallised microstructure of sample 3 after the recrystallisation annealing despite the much smaller grain size in comparison to sample 2, see **Figure 68**.

6.3.1.2 Evolution of the contaminants

The uneven chemical attack in **Figure 63** is the result of the distribution of the contaminants. Their non-uniform distribution indicates that the re-molten aluminium was not contaminated in the first place. Instead, the aluminium powder has probably come into contact with the contaminants during or after the atomisation.

Due to its low melting point of Sn, the contaminants are able to form a liquid phase during the pre-heating at 350°C before the extrusion. After the extrusion, this liquid phase is cooled down and the oxide border is the segregation resulting from the solidification. This is the reason for the shape of the contaminants, which are surrounded by oxide borders and have the Sn-riched particle in the centre, see **Figure 64**.

During the heat treatment, the high temperature will allow the diffusion of the alloying elements. The contaminants are no exception. As a result, the contaminants do not form a cluster anymore at the later stages, but rather are distributed over the sample, see **Figure 65b**.

6.3.1.3 Greater hardness drop in comparison to sample 2

By analogy with sample 2, the finer grains of sample 3 would help the diffusion of Sc and Zr atoms even further. More over, the investigation on this sample by Vlach et al. shows an earlier precipitation of Al_3Sc during the isochronal annealing if the sample is extra cold rolled prior to the annealing [94]. As a result, the hardness of sample 3 declines even lower than sample 2.

6.3.1.4 Specific resistivity offset at the end of the experiment

It was discussed earlier in chapter 6.3.1.1 that the offset between the specific resistivities of sample 2 and sample 3 is caused by the different dislocation density, which scatters the electron flow. However, the smaller offset becomes smaller at stage 5, and it is clear that the bigger rebound at stage 6 is responsible for the narrower offset. Its specific resistivity is almost identical to the beginning as opposed to samples 1 and 2.

Since the narrower offset shows up at stage 6, it might be tempting to think that the dissolution of the precipitates was stronger in sample 3. If that really was the case, the XRD spectrum in **Figure 58c** should have displayed nothing except aluminium. More over, with a lower dislocation density than sample 2, it is hardly possible for sample 3 to have recovered more than the former. All these contradictions lead us to consider the influence of the contaminations on this rebound.

As mentioned above, the sample was contaminated when it was still aluminium powder. The clusters of contaminants are less likely to interfere with the electron flow. Additionally, the main element of the contamination is Sn, which has a very low solubility in Al (0,02 wt%). Therefore, the specific resistivities are not affected by the contaminations during the annealing at low temperatures.

However, the contaminants are scattered over the sample when annealed at a higher temperature due to the higher diffusivity. At the same time, the retrograde solubility of Sn allows the Al solid solution to contain more Sn at higher temperatures than at the eutectic. The Sn solubility is about 0,12 wt% at 600°C according to **Figure 40b**. For us, at least the half of Sn should be stored in the Al solid solution when sample 3 is annealed at 600°C. Thus, it is plausible that the dissolution of Sn and/or the other contaminants is responsible for the stronger rebound at stage 6.

6.3.2 Corrosion behaviour

6.3.2.1 Corrosion characteristics

The corrosion characteristics are evaluated by the definitions given in chapter 2.1.3. As the corrosion reaction takes place at the interface of the sample and the environment, the microstructure is automatically understood to be the same as in the given states, that is, the similar distribution of the precipitates. Unfortunately, this is not the case for sample 3.

Definitely, the corrosion characteristics are affected by the randomly found clusters of contaminants. Based on the background from chapter 3.4, Sn would be the main element, which alters the corrosion behaviour of sample 3. The first effect we encounter, is the data scattering of j_{Corr}, which occurs randomly before the annealing at 600°C.

The observation indicates that the corrosion of sample 3 is accelerated by the presence of Sn. Moreover, Sn is responsible for the potential shift of about 300 mV between E_{Corr} of samples 2 and 3. The gap is considerably large, even for the heat-treatable alloys, see **Table 5**. Ultimately, with the analysis of the hysteresis loops, the corrosion reaction of sample 3 can be considered as the galvanic corrosion rather than the pitting corrosion.

The type of the corrosion reaction is very crucial for our further discussion since it can directly impact the validity of our evaluation in the first place. In this respect, the author believes that the other corrosion characteristics - E_{b}, E_{pit} and E_{rp} - should be discussed in chapter 6.3.2.3 after the discussion of the polarisation curves.

6.3.2.2 Polarisation curves

Normally, we would not be able to observe the passivation of aluminium alloys because of the instantaneous passivation of the surface, see chapter 2.2.4. But as far as the results are concerned, the surface of sample 3 has to be active in order to show such behaviour, see **Figure 79a**.

As suggested in the previous chapter, the corrosion should be induced by Sn. Hence, the corrosion reaction should arise excessively near the contaminations. The jagged lines in **Figure 79a-c** are caused by the inhomogeneity, which makes the passivation unstable. The smoothed polarisation curves of stages 4 and 5 are the result of the diffusion of Sn.

The further the Sn atoms travel, the higher the anodic current density will become. At the same time, the passive state will be narrower due to the presence of Sn. Nevertheless, the data scattering of j_{Corr} suggests that the contaminants are still not distributed over the sample until stage 6.

From stage 6 onwards, the passive state does not exist anymore as shown in **Figure 78f-h**. At this point, the Sn atoms are more or less distributed over the sample, making the surface constantly active, and that goes against the definitions of the rest of the corrosion characteristics.

6.3.2.3 Hysteresis loops and the validity of E_{b}, E_{pit} and E_{rp}

In spite of the higher j_{Corr}, the hysteresis loops of sample 3 are very small in comparison to that of sample 2. If the reaction had been the pitting corrosion, we should have observed much larger hysteresis loops, which would be necessary for the healing of more severe pitting. On top of that, the polarisation curve of stage 6 shows a negative hysteresis loop, which indicates the faster formation of the oxide layer than the corrosion rate. In other words, on the basis of the hysteresis loops, we are able to confirm that the corrosion reaction of sample 3 during the polarisation is definitely not a pitting corrosion. Together with the influence of Sn on the corrosion, it is safe to conclude that the corrosion of sample 3 is a galvanic corrosion between Sn and the aluminium matrix.

Considering our conclusion, we may use the values of E_{Corr} for E_{b} in stages 6, 7 and 8 because the active surface of the sample should be used to compare with the transpassive states in the earlier stages. The correction of E_{b} is displayed in **Figure 83**.

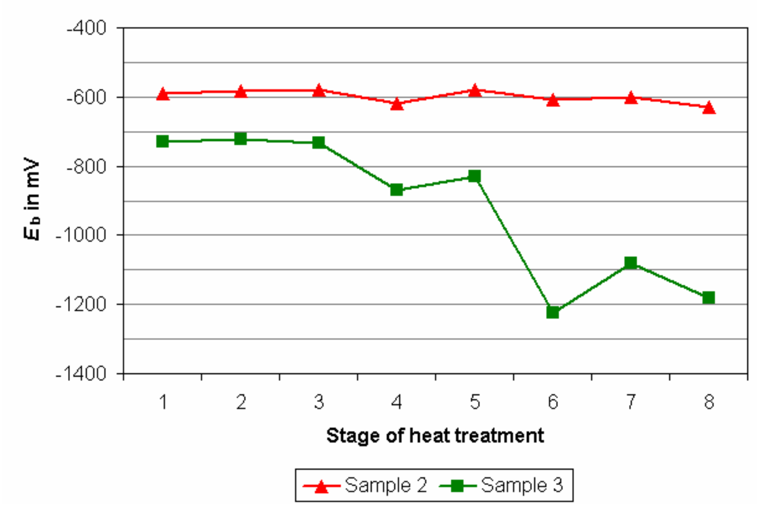

Figure 83 Breakthrough potentials of sample 2 and 3 (correction) in 0,1 M NaCl solution during step annealing

The evaluation of E_{pit}, on the other hand, would be invalid simply because the reaction is not a pitting corrosion to begin with. As for E_{rp}, the results of stages 6, 7 and 8 should be deemed invalid because the surface is unable to passivate itself in the given stages. The galvanic corrosion will just start and stop according to our polarisation, which can be clearly seen from the similarity between E_{Corr} and E_{rp} of these stages.

7. Conclusion

The precipitation hardening effect and the corrosion behaviour of the aluminium alloys containing Mn, Sc, Zr with and without the trace elements (contaminations) have been investigated during the step annealing. Sample 1 and sample 2 are produced by cast and cast-hot extrusion respectively. Sample 3 is prepared by the atomisation following the hot extrusion. The contaminations are found in the latter sample. They consist mainly of Sb, Sn and O.

The Vickers hardness test is used to monitor the hardness change in all samples. The potentiostatic electrochemical measurement is utilised to determine the corrosion characteristics - j_{Corr}, E_{Corr}, E_{b}, E_{pit} and E_{rp} - of samples 2 and 3. The additional corrosion behaviour is observed from the polarisation curves. Together with the light microscope, SEM and TEM images, the following results are observed and discussed:

1) The hardness of the Al-Mn-Sc-Zr alloy containing about 1,4 wt% Mn is not influenced either by the Mn atoms in solid solution or the additional Al_6Mn precipitates with the diameter of about 2 µm.

2) The peak ageing of the aluminium alloy containing 0,25 wt% Sc and 0,15 wt% Zr contributes an additional hardness of about 20 HV5.

3) The $Al_3(Sc,Zr)$ precipitates are responsible for the hardness increase. They are found at stage 1 (as prepared) in all samples. However, the precipitation hardening of sample 1 does not take full effect until the annealing at stage 5, while the peak ageing condition is already obtained in samples 2 and 3 during or after the extrusion.

4) The hardness increase by the hot extrusion at 350°C is negligible. Nevertheless, the increasing dislocation density from this process is still detectable by the resistivity measurement at -196°C (77 K).

5) The precipitation of the Al_6Mn phase is benefited by the extrusion. The filament grain structure also promotes the Al_6Mn precipitation at the grain boundaries in comparison to the cast structure.

6) The hardness drop in the over ageing condition is due to the coarsening and the (partial) dissolution of the $Al_3(Sc,Zr)$ precipitates.

7) The retrograde solubility of Sn can be accounted for the stronger rebound of the specific resistivity in sample 3 at stage 6.

8) The $Al_3(Sc,Zr)$ precipitates and/or Al_6Mn precipitates can prevent the recrystallisation during the step annealing.

9) After the recrystallisation annealing at 600°C for 48 hours, sample 2 is partially recrystallised near the surface, whereas the recrystallisation can not be observed in sample 3. However, the lower dislocation density (stored deformation energy) of sample 3 might be the reason for this.

10) The corrosion behaviour of sample 2 remains unchanged during the step annealing. Its corrosion characteristics determined from the potentiostatic polarisation in the 0,1 M NaCl solution are j_{Corr} 0,3 µA/cm² , E_{Corr} -900 mV, E_{b} -600mV, E_{pit} -580 mV and E_{rp} -1000 mV. The corrosion rate (j_{Corr}) is slightly higher than the high purity aluminium, but E_{pit} indicates a better resistance to the pitting corrosion.

11) The contaminants, mainly Sn, are responsible for the erratic corrosion behaviour in the 0,1 M NaCl solution. As opposed to the pitting corrosion in sample 2, the corrosion reaction of sample 3 is the galvanic corrosion.

12) The contaminations are distributed over the sample during the heat treatment. As a result, the surface of sample 3 is always active after the annealing at 600°C.

13) The Mn atoms in the solid solution have a more superior resistance to the pitting corrosion than the Al_6Mn precipitates.

The investigation results have displayed the precipitation hardening effect in the Al-Mn alloys, which are considered non-heat treatable, by the additions of Sc and Zr. It is shown that the peak ageing condition can be achieved straight after the hot extrusion, which is advantageous for the shorter production route.

The hot-extruded alloy can withstand the recrystallisation up to 600°C for at least 3 hours due to the presence of $Al_3(Sc,Zr)$ and/or Al_6Mn precipitates. On the other hand, the alloy prepared by the atomisation and hot extrusion has retained the non-recrystallised microstructure after 48 hours at the same temperature, though the less deformation of the sample has to be taken into account. Still, the result could be seen as an additional recrystallisation resistance to the Al-Mn alloys, which will increase the temperature service of this material.

The corrosion resistance of the extruded Al-Mn-Sc-Zr alloy in the 0,1 M NaCl solution is only slightly lower than the high purity aluminium. The unchanged corrosion characteristics mean that the corrosion behaviour is not affected by the precipitates during the heat treatment. With this, we are be able to suggest the combination of Sc 0,25 wt% and Zr 0,15 wt% as the additional alloying elements for Al-Mn alloys without affecting the corrosion resistance.

8. Reference

1 François Cardarelli (2008) Materials Handbook: A Concise Desktop Reference 2nd ed., Springer, London

2 Hans-Jürgen Bargel, Günter Schulze (1988) Werkstoffkunde 5th ed., VDI, Düsseldorf

3 Eberhard Roos, Karl Maile (2011) Werkstoffkunde für Ingenieure: Grundlagen, Anwendung, Prüfung 4th ed., Springer, Berlin, Heidelberg

4 Ian Polmear (2006) Light Alloys: From Traditional Alloys to Nanocrystals 4th ed., Elsevier/Butterworth Heinemann, Amsterdam, Boston

5 Christian Vargel, Michel Jacques, Martin P. Schmidt (2004) Corrosion of Aluminium, Elsevier, Amsterdam, Boston

6 DIN EN 573-3 (2009) Aluminium and aluminium alloys - Chemical composition and form of wrought products - Part 3: Chemical composition and form of products, Deutsches Institut für Normung e. V., Beuth, Berlin

7 V.G. Davydov, T.D. Rostova, V.V. Zakharov et al. (2000) Scientific principles of making an alloying addition of scandium to aluminium alloys, Materials Science and Engineering **A280**: 30-36

8 T.D. Rostova, V.G. Davydov, V.I. Yelagin et al. (2000) Effect of Scandium on Recrystallization of Aluminum and its Alloys, Materials Science Forum **331-337**: 793-798

9 M.J. Jones, F.J. Humphreys (2003) Interaction of recrystallization and precipitation: The effect of Al_3Sc on the recrystallization behaviour of deformed aluminium, Acta Materialia **51**: 2149-2159

10 Zaki Ahmad (2003) The Properties and Application of Scandium-Reinforced Aluminum, JOM **55**: 35-39

11 Børge Forbord, Håkon Hallem, Nils Ryum et al. (2004) Precipitation and recrystallisation in Al-Mn-Zr with and without Sc, Materials Science and Engineering **A287-289**: 936-939

12 Keith E. Knipling, Richard A. Karnesky, Constance P. Lee et al. (2010) Precipitation evolution in Al-0.1Sc, Al-0.1Zr and Al-0.1Sc-0.1Zr (at.%) alloys during isochronal aging, Acta Materialia **58**: 5184-5195

13 Keith E. Knipling, David N. Seidman, David C. Dunand (2011) Ambient- and high-temperature mechanical properties of isochronally aged Al-0.06Sc, Al-0.06Zr and Al-0.06Sc-0.06Zr (at.%) alloys, Acta Materialia **59**: 943-954

14 Jia Zhi-hong, Jostein Røyset, Jan Ketil Solberg et al. (2012) Formation of precipitates and recrystallization resistance in Al-Sc-Zr alloys, Transactions of Nonferrous Metals Society of China **22**: 1866-1871

15 DIN EN ISO 6507-1 (2005) Metallic materials - Vickers hardness test - Part 1: Test method, Deutsches Institut für Normung e. V., Beuth, Berlin

16 Paul Dobrinski, Gunter Krakau, Anselm Vogel (1984) Physik für Ingenieure 6th ed., B. G. Teubner, Stuttgart

17 Wolfgang Bergmann (1984) Werkstofftechnik Teil 1: Grundlagen, Carl Hanser, München, Wien

18 J. M. Ziman (1958) Transport Properties of Solids, Il Nuovo Cimento **7**: 353-376

19 Arun K. Pal, S. Chaudhuri (1976) Effect of grain-boundary scattering on the electrical resistivity of indium films, Journal of Materials Science **11**: 872-876

20 Carl H. Hamann, Wolf Vielstich (1985) Elektrochemie I: Leitfähigkeit, Potentiale, Phasengrenzen 2nd ed., VCH, Weinheim, Florida, Basel

21 Gerd Wedler (1982) Lehrbuch der physikalischen Chemie, Verlag Chemie, Weinheim, Florida, Basel

22 Gustav Kortüm, Walter Braun (1972) Lehrbuch der Elektrochemie 5th ed., Verlag Chemie, Weinheim

23 Peter W. Atkins (1987) Physikalische Chemie, VCH, Weinheim, Basel, Cambridge, New York

24 Carl H. Hamann, Wolf Vielstich (1985) Elektrochemie II: Elektrodenprozesse, Angewandte Elektrochemie, Verlag Chemie, Weinheim

25 Robert G. Kelly, John R. Scully, David W. Shoesmith, Rudolph G. Buchheit (2003) Electrochemical Techniques in Corrosion Science and Engineering, Marcel Dekker Inc., New York, Basel

26 P. J. Gellings (1976) Introduction to corrosion prevention and control for engineers, Delft University Press, Rotterdam

27 DIN EN ISO 8044 (1999) Corrosion of metals and alloys - Basic terms and definitions, Deutsches Institut für Normung e. V., Beuth, Berlin

28 DIN EN ISO 17475 (2008) Corrosion of metals and alloys - Electrochemical test methods - Guidelines for conducting potentiostatic and potentiodynamic polarization measurements, Deutsches Institut für Normung e. V., Beuth, Berlin

29 ASM International (1987) ASM Handbook (Metals Handbook) Volume 13: Corrosion 9th ed., ASM International, Ohio

30 E. Wendler-Kalsch, H. Gräfen (1998 reprinted 2012) Korrosionsschadenkunde, Springer-Verlag, Berlin, Heidelberg

31 ASTM G150 (1999 reapproved 2010) Standard Test Method for Electrochemical Critical Pitting Temperature Testing of Stainless Steels, ASTM International, Pennsylvania

32 Günter Gottstein (2007) Physikalische Grundlagen der Materialkunde 3rd ed., Springer, Berlin, Heidelberg

33 F. J. Humphreys, M. Hatherly (2004) Recrystallization and Related Annealing Phenomena 2nd ed., Elsevier, Amsterdam, Boston

34 K. L. Kendig, D. B. Miracle (2002) Strengthening mechanisms of an Al-Mg-Sc-Zr alloy, Acta Materialia **50**: 4165-4175

35 V. V. Zakharov (2003) Effect of Scandium on the Structure and Properties of Aluminum Alloys, Metal Science and Heat Treatment **45**: 246-253

36 M. Ferry, N. E. Hamilton, F. J. Humphreys (2005) Continuous and discontinuous grain coarsening in a fine-grained particle-containing Al-Sc alloy, Acta Materialia **53**: 1097-1109

37 J. Røyset, N. Ryum (2005) Scandium in aluminium alloys, International Materials Review **50**: 19-44

38 A. Tolley, V. Radmilovic, U. Dahmen (2005) Segregation in $Al_3(Sc,Zr)$ precipitates in Al-Sc-Zr alloys, Scripta Materialia **52**: 621-625

39 B. Forbord, L. Auran, W. Lefebvre et al. (2006) Rapid precipitation of dispersoids during extrusion of an Al-0.91 wt.% Mn-0.13 wt.% Zr-0.17 wt.% Sc-alloy, Materials Science and Engineering **A424**: 174-180

40 B. Forbord, H. Hallem, J. Røyset et al. (2008) Thermal stability of $Al3(Sc_x,Zr_{1-x})$-dispersoids in extruded aluminium alloys, Materials Science and Engineering **A475**: 241-248

41 I. G. Brodova, T. I. Yablonskikh, I. G. Shirinkina et al. (2008) Effect of Rapid Hardening of Melt, Annealing, and Severe Plastic Deformation on Formation of Scandium and Zirconium Aluminides in Al - Mg - Mn Alloys, Metal Science and Heat Treatment **50**: 495-501

42 Woei-Shyan Lee, Tao-Hsing Chen, Chi-Feng Lin et al. (2010) Impact deformation behaviour and dislocation substructure of Al-Sc alloy, Journal of Alloys and Compounds **493**: 580-589

43 Yiyou Tu, Huan Qian, Xuefend Zhou (2014) Effect of Scandium on the Interaction of Concurrent Precipitation and Recrystallization in Commercial AA3003 Aluminum Alloy, Metallurgical and Materials Transactions **A45**: 1883-1891

44 O. Hunderi, E. Nes, N. Ryum (1989) On the Zener Drag-Addendum, Acta Metallurgica **37**: 129-133

45 W. H. J. Vernon (1927) Second experimental report to the Atmospheric Corrosion Research Committee (British Non-Ferrous Metals Research Association), Transactions of the Faraday Society **23**: 113-183 Section V

46 N. F. Mott (1939) A theory of the formation of protective oxide films on metals, Transactions of the Faraday Society **35**: 1175-1177

47 Friedrich Ostermann (2007) Anwendungstechnologie Aluminium 2nd ed., Springer, Berlin, Heidelberg

48 W. Huppatz, H. Krajewski (1979) Untersuchungen zur Korrosionsresistenz von einigen gebrauchlichen Aluminiumwerkstoffen in Meerwasser, Materials and Corrosion **30**: 673-684

49 C. M. Liao, J. M. Olive, M. Gao et al. (1998) In-Situ Monitoring of Pitting Corrosion in Aluminium Alloy 2024, Corrosion **54**: 451-458

50 H. Nielsen, W. Hufnagel, G. Ganoulis, (1974) Aluminium-Taschenbuch 13th ed., Aluminium-Verlag, Düsseldorf

51 H. Schumann (1983) Metallographie 11th ed., VEB Deutscher Verlag für Grundstoffindustrie, Leipzig

52 D. Altenpohl (1965) Aluminium und Aluminiumlegierungen, Springer, Berlin, Göttingen, Heidelberg, New York

53 Du Yu-xuan, Zhang Xin-ming, Ye Ling-ying et al. (2006) Recrystallization behavior of high purity aluminum at 300°C, Transactions of Nonferrous Metals Society of China **16**: 1307-1312

54 Malgorzata Lewandowska, Tomasz Wejrzanoski, Krzysztof J. Kurzydłowski (2008) Journal of Materials Science **43**: 7495-7500

55 Yucel Birol (2009) Impact of homogenization on recrystallization of a supersaturated Al-Mn alloy, Scripta Materialia **60**: 5-8

56 N. H. Lee, P. W. Kao, T. Y. Tseng (2012) Effect of manganese addition on the tensile properties of cold-rolled and recovery-annealed aluminum alloy sheets, Materials Science and Engineering **A535**: 297-305

57 S. Wronski, J. Tarasiuk, B. Bacroix (2013) Microstructure heterogeneity after the ECAP process and its influence on recrystallization in aluminium, Materials Characterization **78**: 60-68

58 W. C. Liu, B. Radhakrishnan (2010) Recrystallization behavior of a supersaturated Al-Mn alloy, Materials Letters **64**: 1829-1832

59 L. S. Toropova, D. G. Eskin, M. L. Kharakterova et al. (1998) Advanced Aluminum Alloys Containing Scandium: Structure and Properties, Gordon and Breach Science Publishers, Amsterdam

60 E. A. Marquis, D. N. Seidman (2001) Nanoscale Structural Evolution of Al_3Sc Precipitates in Al(Sc) Alloys, Acta Materialia **49**: 1909-1919

61 K. E. Knipling, D. C. Dunand, D. N. Seidman (2007) Nucleation and Precipitation Strengthening in Dilute Al-Ti and Al-Zr Alloys, Metallurgical and Materials Transactions **38A**: 2552-2563

62 C. B. Fuller, A. R. Krause, D. C. Dunand et al. (2002) Microstructure and mechanical properties of a 5754 aluminum alloy modified by Sc and Zr additions, Materials Science and Engineering **338A**: 8-16

63 N. A. Belov, A. N. Alabin, D. G. Eskin (2006) Optimization of hardening of Al-Zr-Sc cast alloys, Journal of Materials Science **41**: 5890-5899

64 A. F. Norman, P. B. Prangnell, R. S. Mc Ewen (1998) The Solidification Behaviour of Dilute Aluminium Scandium Alloys, Acta Materialia **46**: 5715-5732

65 C. B. Fuller, D. N. Seidman, D. C. Dunand (2003) Mechanical properties of Al(Sc,Zr) alloys at ambient and elevated temperatures, Acta Materialia **51**: 4803-4814

66 A. K. Lohar, B. N. Mondal, S. C. Panigrahi (2010) Influence of cooling rate on the microstructure and ageing behavior of as-cast Al-Sc-Zr alloy, Journal of Materials Processing Technology **210**: 2135-2141

67 S. Badrinarayanan, H. B. Mathur (1968) Impurity Diffusion of Antimony and Silver in Aluminium, The International Journal of Applied Radiation and Isotopes **19**: 353-360

68 G. M. Hood, R. J. Schultz (1971) The Diffusion of Manganese in Aluminium, Philosophical Magazine **23**: 1479-1489

69 T. Marumo, S. Fujikawa, K. Hirano (1973) Diffusion of Zirconium in Aluminum, Journal of Japan Institute of Light Metals **23**: 17-25

70 S.-I. Fujikawa (1997) Impurity Diffusion of Scandium in Aluminum, Defect and Diffusion Forum **143-147**: 115-120

71 G. Erdélyi, K. Freitag, H. Mehrer (1991) Diffusion of tin implanted in aluminium, Philosophical Magazine **63A**: 1167-117

72 G. Neumann, C. Tuijn (2002) Impurity diffusion in aluminium, Solid State Phenomena **88**: 129-137

73 B. Forbord, W. Lefebvre, F. Danoix et al. (2004) Three dimensional atom probe investigation on the formation of Al_3(Sc,Zr)-dispersoids in aluminium alloys, Scripta Materialia **51**: 333-337

74 W. Lefebvre, F. Danoix, H. Hallem et al. (2009) Precipitation kinetic of Al_3(Sc,Zr) dispersoids in aluminium, Journal of Alloys and Compounds **470**: 107-110

75 G. Petzow, G. Effenberg (1993) Ternary Alloys: A Comprehensive Compendium of Evaluated Constitutional Data and Phase Diagrams Volume 7: Al-Mg-Se to Al-Ni-Ta, VCH, Weinheim, New York

76 L. L. Rokhlin, N. R. Bochvar, I. E. Tarytina et al. (2010) Phase Composition and Recrystallization of Al-Based Al-Sc-Mn-Zr Alloys, Russian Metallurgy (Metally) **2010**: 241-247

77 V. Raghavan (2012) Al-Mn-Sc-Zr (Aluminum-Manganese-Scandium-Zirconium), Journal of Phase Equilibria and Diffusion **33**: 74-75

78 M. Vlach, I. Stulíková, B. Smola (2012) Phase transformations in non-isothermally annealed as-cast and cold-rolled AlMnScZr alloys, International Journal of Materials Research **103**: 814-820

79 M. Vlach, I. Stulikova, B. Smola et al. (2012) Effect of cold rolling on precipitation processes in Al-Mn-Sc-Zr alloy, Materials Science and Engineering **548A**: 27-32

80 ASM International (1992) ASM Handbook (Metals Handbook) Volume 2: Properties and Selection : Nonferrous Alloys and Special-Purpose Materials 10th ed., ASM International, Ohio

81 A. J. Mc Alister, D. J. Kahan (1983) The Al-Sn (Aluminum-Tin) System, Bulletin of Alloy Phase Diagrams **4**: 410-414

82 H. Lukas, E. Lysova, Q. Ran et al. (1993) Al-Sb-Sn Ternary Phase Diagram Evaluation, in MSI Eureka G. Effenberg (Ed.), Document ID: **10.19331.1.3**, MSI Materials Science International Services, Stuttgart

83 A. J. Mc Alister (1984) The Al-Sb (Aluminum-Antimony) System, Bulletin of Alloy Phase Diagrams **5**: 462-465

84 M. O. Krasovskii, V. O. Lavrenko, L. M. Kostenko (2010) Anodic Behavior of Al-Bi and Al-Sb Alloys in 3% NaCl Solution, Powder Metallurgy and Metal Ceramics **49**: 347-350

85 W. v. Baeckmann, W. Schwenk, W. Prinz et al. (1997) Handbook of cathodic corrosion protection: Theory and practice of electrochemical protection processes 3rd ed., Gulf Publishing Co., Texas

86 U. Erb, K. T. Aust (1984) Microstructure and corrosion behaviour of aluminium containing a small addition of tin, Journal of Materials Science Letters **3**: 585-587

87 M. Kliškić, J. Radošević, S. Gudić et al. (1998) Cathodic polarization of Al-Sn alloy in sodium chloride solution, Electrochimica Acta **43**: 3241-3255

88 M. Vlach (2005) WDS'05 Proceedings of Contributed Papers Part III: 637-642

89 ASTM G5 (1994 reapproved 2004) Standard Reference Test Method for Making Potentiostatic and Potentiodynamic Anodic Polarization Measurements, ASTM International, Pennsylvania

90 S. P. Bhat, T. R. Ramachandran, A. K. Jena (1974) Splat cooling of aluminium-manganese alloys, Journal of Materials Science, **9**: 1759-1763

91 H. Huang, B. Ou (2009) Evolution of precipitation during different homogenization treatments in a 3003 aluminum alloy, Materials & Design **30**: 2685-2692

92 M. Vlach, I. Stulíková, B. Smola et al. (2012) Microstructure, Thermal and Mechanical Properties of Non-Isothermally Annealed Al-Sc-Zr and Al-Mn-Sc-Zr Alloys Prepared by Powder Metallurgy, Acta Physica Polonica **A122**: 439-443

93 M. Vlach, I. Stulíková, B. Smola et al. (2013) Response of Hot-Extruded Al-Mn-Sc-Zr Alloy to Annealing with Constant Heating Rate, Defect and Diffusion Forum **334-335**: 161-166

94 M. Vlach, I. Stulíková, B. Smola et al. (2013) Precipitation in cold-rolled Al-Sc-Zr and Al-Mn-Sc-Zr alloys prepared by powder metallurgy, Materials Characterization **86**: 59-68

95 V. Neubert, B. Smola, I. Stulíková et al. (2007) Microstructure, mechanical properties and corrosion behaviour of dilute Al-Sc-Zr alloy prepared by powder metallurgy, Materials Science and Engineering **A464**: 358-364

Curriculum Vitae

Personal Information

Date of Birth	17 October 1982
Place of Birth	Bangkok, Thailand
Citizenship	Thai

Education

From 03/2009	**Research Assistant**, Institut für Materialprüfung und Werkstofftechnik Dr. Neubert GmbH, Clausthal-Zellerfeld
2002-2009	**Diplomingenieur** (Graduate Engineer), Clausthal University of Technology, Clausthal-Zellerfeld Course of Studies: Metallurgy Student Research Project (Studienarbeit): Experimentelle Untersuchung der Phasengleichgewichte im System Ce-Mg-Sr Thesis (Diplomarbeit): Einfluss eisenhaltiger Phasen auf die Warmfestigkeit einer neu entwickelten Al-Mn-Gusslegierung
2001-2002	**Eligibility of University Admission** (Hochschulzugangsberechtigung): Feststellungsprüfung, Niedersächsisches Studienkolleg, Hannover
2000-2001	**German Language Course**, Goethe-Institut, Göttingen
2000	**Thai High School Degree** (Mathayom), Chulalongkorn University Demonstration Secondary School (Satit Chula)

Publications

1. Microstructure, Thermal and Mechanical Properties of Non-Isothermally Annealed Al-Sc-Zr and Al-Mn-Sc-Zr Alloys Prepared by Powder Metallurgy

   M. Vlach, I. Stulíková, B. Smola, H. Císařová, J. Piešová, S. Daniš, R. Gemma, D. Tanprayoon and V. Neubert

   Acta Physica Polonica A, Vol. 122 (2012), pp. 439-443

2. Phase transformations in non-isothermally annealed as-cast and cold-rolled AlMnScZr alloys

   Martin Vlach, Ivana Stulíková, Bohumil Smola, Hana Císarová, Jaroslava Piešová, Stanislav Daniš, Ryota Gemma, Jaroslav Málek, Dhritti Tanprayoon, and Volkmar Neubert

   International Journal of Materials Research: Vol. 103 (2012), No. 7, pp. 814-820

3. Effect of cold rolling on precipitation processes in Al–Mn–Sc–Zr alloy

   M. Vlach, I. Stulikova, B. Smola, J. Piesova, H. Cisarova, S. Danis, J. Plasek, R. Gemma, D. Tanprayoon, V. Neubert

   Materials Science and Engineering: A, Vol. 548 (2012), pp. 27–32

4. Response of Hot-Extruded Al-Mn-Sc-Zr Alloy to Annealing with Constant Heating Rate

   Martin Vlach, Ivana Stulíková, Bohumil Smola, Hana Císařová, Tomas Kekule, Jaroslav Malek, Dhritti Tanprayoon, Volkmar Neubert

   Defect and Diffusion Forum Vols. 334-335 (2013), pp. 161-166

5. Precipitation in cold-rolled Al–Sc–Zr and Al–Mn–Sc–Zr alloys prepared by powder metallurgy

   M. Vlach, I. Stulikova, B. Smola, T. Kekule, H. Kudrnova, S. Danis, R. Gemma, V. Ocenasek, J. Malek, D. Tanprayoon, V. Neubert

   Materials Characterization, Volume 86 (2013), pp. 59–68